FRACTURE CHARACTERIZATION USING MULTICOMPONENT ELASTIC WAVES

A Thesis Presented to

the Faculty of the Department of Earth and Atmospheric Sciences

University of Houston

In Partial Fulfillment

of the Requirements for the Degree

Master of Science

By

Xiaoyun Peng

May 2019

FRACTURE CHARACTERIZATION USING MULTICOMPONENT ELASTIC WAVES

Xiaoyun Peng

APPROVED:

Dr. Yingcai Zheng, Advisor

Dr. John Castagna

Dr. Enru Liu, ExxonMobil

Dean, College of Natural Sciences and Mathematics

Acknowledgments

I would like to express my great thanks to the people who have been involved and supported me all the time during my Master’ s at the University of Houston.

First, I would like to express my deepest gratitude to my supervisor, Dr. Yingcai Zheng. It was truly an honor to be accepted as your student. Your continuous support, patience, advice, instructions, and strict attitude towards science pushed on the right path through my research. Thank you for teaching me how to do research from the very start. Thank you for helping me try new ideas, solve different problems, and revise this thesis work. Thank you for encouraging me to attend activities and present my work to more audiences. Thank you, for making me believe that I could do more.

I also wish to express my sincerest appreciation to my committee members, Dr. John Castagna, and Dr. Enru Liu for their participation and sincere suggestions for my research.

I feel privileged to have learned a great deal from my accomplished peers Hao Hu, Jiaxuan Li, Zhili Wei, Shuhang Tang, Yuandi Gan, and Hongru Hu about wave propagation, anisotropy, and coding. I want to express special thanks to Yingshuai Ding, who spent a great deal of time helping me solve a tricky problem that trapped me for a long time during my research. I also want to thank David Li, for helping me with the grammar of my thesis work.

I thank Zhongmin Tao, for being my roommate and tolerating me over the past two years. Thank you for being my best friend and always listening to my heart

whenever I am upset. Thank you for making me delicious food when I had no time to cook. Thank you for taking care of me when I was sick.

Last but not least, I thank my family for their unending patience, encouragement, love, support, and faith in me. I want to especially thank my uncle Zhibin Wei for criticizing me all the way to make me be aware of all my weaknesses and felt the urge to correct them. It is him, who makes me a better learner. Thank you my boyfriend, Di Wu, for always supporting and encouraging me.

FRACTURE CHARACTERIZATION USING MULTICOMPONENT

ELASTIC WAVES

An Abstract of a Thesis

Presented to

the Faculty of the Department of Earth and Atmospheric Sciences

University of Houston

In Partial Fulfillment

of the Requirements for the Degree

Master of Science

By

Xiaoyun Peng

May 2019

Abstract

Fractures impact reservoir management, drilling, and well completion. Therefore, we characterize fractures systems to understand subsurface stress and flow fields.

I studied four topics on fracture characterization for both applied and earthquake seismology: (1) the effect of fractured reservoir layer thickness on reflected *P* wave amplitudes; (2) the effect of fractured reservoir layer thickness on shear-wave splitting; (3) the effect of normal and tangential fracture compliances on anisotropy and shear wave splitting; and (4) the effect of incidence angle and subducting slab dipping angle on the transmitted seismic wavefield.

I considered a 3-layer model in which the middle layer is anisotropic. I applied full-wave modeling based on plane wave expansion in anisotropic media. The modeling includes all reflections and mode conversions.

In topic 1, I studied how layer thickness affects the reflected *P* wave amplitude variation versus azimuth caused by an incident *P* plane wave in an HTI fractured layer. I found that to accurately extract fracture orientation and density using azimuthal *P*-wave traveltime as a function of azimuth, the thickness of the fractured reservoir layer cannot be less than the *P* wavelength.

In topic 2, I found that the splitting time for reflected shear waves is related to the thickness of the fractured layer. To observe splitting from seismic data, the layer thickness needs to be ~5 times the S wavelength.

In topic 3, I used linear-slip boundary conditions to represent fractures. I found that shear wave splitting is only affected by the tangential compliance, Z_T, because the Thomsen's parameter, γ, only relates to tangential compliance, Z_T, and not the normal compliance, Z_N. From my modeling, I find it difficult to observe shear wave splitting from synthetic seismic data if the Z_N/Z_T is low (<0.4) even if the fracture thickness is thick enough.

In topic 4, I extracted polarization, ϕ, of the fast S wave and the time delay, *dt*, between the fast and slow S waves measured from seismic records to characterize the possible anisotropy in subducted slabs. I found that ϕ and *dt* are related to the anisotropic property, the slab dipping and incidence angles.

Table of Contents

List of figures

List of tables

Chapter 1

Introduction

Fractures are mechanical discontinuities in rocks that originate from strains caused by stress concentrations around flaws, heterogeneities, and physical discontinuities. They form in response to lithostatic, tectonic, thermal stresses, and high fluid pressures. Fractures may occur at scales ranging from microscopic pore sizes to tectonic plate scales.

Fractures, which are pervasive within the Earth's crust, play important roles in the multi physical response of the subsurface. The presence of coherent fracture sets can lead to observable seismic anisotropy enabling seismic techniques to remotely locate and characterize fracture systems (Yousef and Angus, 2016). If we know information about certain fractures, we can predict the stress state of the subsurface. Because fractures provide pathways for fluid flow, they are important for a variety of scientific and engineering applications, including oil and gas exploration and production and geotechnical and hydrogeological applications. Natural fracture systems can dominate the fluid drainage pattern for reservoirs in rocks with low matrix permeability (e.g., Fang *et al.*, 2017). Fracture systems also control the dispersion of fluids into and through the subsurface. Because fracture systems control how fluids flow through the subsurface, they can affect the stability of engineering structures. Therefore, knowing the spatial distribution and mechanical properties of fracture systems is important for knowing the subsurface as well as oil exploration.

Traditional non-seismic methods for natural fracture characterization could only measure fractures near the wellbore. These methods include detecting fractures from core description and image logs (Nelson, 2001; Khoshbakht *et al.*, 2009) and using data from well/production logging tests (Dyke *et al.*, 1995; Aguilera and Aguilera, 2001). Traditional seismic methods for fracture characterization involve extracting fracture information from seismic data. These methods include analyzing reflected P wave amplitude variation with offset and azimuth (AVOAz) (Rüger, 1998; Hall and Kendall, 2003; Liu *et al.*, 2010), shear wave splitting (Gaiser and Van Dok, 2001; Crampin and Chastin, 2003), or P-to-S converted waves (Vetri *et al.*, 2003). In my research, I will use surface seismic data to probe subsurface fractures at the field scale.

According to Schoenberg (1980), a fracture can be described by a linear-slip boundary condition. I will use the linear-slip theory of Schoenberg in this research. The linear slip fracture model can be viewed as an effective stiffness matrix from the background medium properties, fracture density and fracture compliance (Schoenberg and Sayers, 1995; Fang *et al.*, 2017).

In the linear slip model, a fracture is characterized by fracture compliance, which relates deformation to applied stress. The compliance of a fracture can be further resolved into the compliance of the fractures under normal and tangential deformation, which is the normal compliance, Z_N, and tangential compliance, Z_T (Hsu and Schoenberg, 1993). Experiments have indicated that Z_N/Z_T is related to the stiffness of the fluid types in the fracture (e.g., Sayers and den Boer, 2012), as well as terms that describe the internal architecture of the fractures. The effect of Z_N/Z_T on the anisotropy is therefore very important if we want to have a better understanding of the fracture. The relation between Z_N/Z_T and the reflected wavefields will be discussed later in my thesis.

I will numerically calculate the reflected and transmitted wavefield in anisotropic media. For a P wave incidence, I will investigate the P wave reflection amplitude variation with azimuth (AVAz) by extracting azimuthal gathers at a constant offset. The effect of the fractured reservoir layer thickness on the anisotropy and reflected P and S wave amplitudes will also be discussed.

For a S wave incidence, my modeling will show the minimum thickness of the fractured layer in order to observe the shear wave splitting phenomenon from seismic records. I will also investigate how the incidence angle and slab dipping angle are going to influence the transmitted wavefield of an anisotropic subducting slab by extracting the splitting time of fast and slow S wave and the polarization of the fast S wave.

1.1 Research topics and organization of the thesis

In Chapter 2, I will review basic concepts of seismic anisotropy. I will introduce the definition of seismic anisotropy, Hooke's law, and several different symmetry classes. I would also review the linear slip fracture model which I use as my fracture model.

In Chapter 3, I will illustrate in detail how I calculate the reflection and transmission coefficients for a three-layered model.

In Chapter 4 and 5, I will show how the fracture layer thickness affects the P and S scattered waves for different azimuths. For S waves, the relationship between the thickness of the fracture layer and the S wave splitting time is presented in Chapter 5. I will also assess the feasibility of using P wave amplitude variation with azimuth (AVAz) and the shear wave splitting to obtain fracture information from seismic data for different reservoir thicknesses.

In Chapter 6, I will present the effect of normal and tangential fracture compliances on P reflection amplitude variation and the splitting time of fast and slow S reflections.

In Chapter 7, I will apply my modeling procedure to study anisotropy in subducting slabs. I will calculate the transmitted wavefield with SV and SH wave incidence of a subducting fractured slab due to different incidence angles and different anisotropy type (HTI, VTI and TTI models). The shear wave splitting is used as a tool here to extract the splitting time and the polarization of the fast S wave.

Finally, in Chapter 8, I will conclude my thesis work.

Chapter 2

Review of Seismic Anisotropy

2.1 Introduction

Measuring seismic anisotropy can provide useful information for characterizing fracture properties in rocks. It also gives us a better understanding of structures and locations of faults to determine subsurface stress and strain. Over the past four decades, research in seismic anisotropy has dramatically gained attention. Using seismic anisotropy in applied geophysics will help us improve seismic imaging and extract fracture information that is difficult to obtain from well data.

In this chapter, I will review the fundamentals of seismic anisotropy that are necessary to understand the principle of seismic fracture characterization with a mathematical description.

2.2 Definition

For seismic anisotropy, we are referring to the directional variation of a material's response to the passage of seismic (elastic) waves (Liu and Martinez, 2012). According to Thomsen (2002), seismic anisotropy refers to "the dependence of seismic velocity upon angle", which means seismic velocity depends on the direction of wave propagation or polarization.

2.3 Generalized Hooke's law

Constitutive equations for a linear elastic material are called Hooke's Law, which describe the linear relations between stress σ and strain ε tensors:

$$\sigma_{ij} = C_{ijkl}\varepsilon_{kl}\,, \tag{2.1}$$

or

$$\varepsilon_{ij} = S_{ijkl}\sigma_{kl}\,, \tag{2.2}$$

where C_{ijkl} is the stiffness tensor and S_{ijkl} is the compliance tensor. Both tensors are fourth-rank tensor with 81 components ($i, j, k, l = 1,2,3$). However, not all 81 components are independent. Because of stress and strain tensor symmetry and requirements of energy constraints, we can reduce the number of independent elastic constants of C_{ijkl} from 81 to 21 by using the following relations:

$$C_{ijkl} = C_{ijlk}\,, \tag{2.3}$$

$$C_{ijkl} = C_{jikl}\,, \tag{2.4}$$

and

$$C_{ijkl} = C_{klij}\,. \tag{2.5}$$

These types of materials exhibit the triclinic symmetry which is the lowest class of symmetry (*Table 1*). The highest class of symmetry is isotropy in which the material has uniform properties in all orientations. Isotropic rocks only need two independent elastic constants to characterize the elastic tensor. These constants are called the Lame parameters, λ and μ.

Table 1 The symmetry classes from the lowest system (triclinic) to the highest (isotropy)

Symmetry Class	Number of Independent Elastic Stiffness
Triclinic	21
Monoclinic	11
Orthorhombic	9
Trigonal	6
Tetragonal	6
Hexagonal	5
Cubic	3
Isotropic	2

In isotropic media, we have the generalized Hooke's law for isotropic media, describing the relationship between the stress σ and strain ε using two constants - Lame constants λ and μ:

$$\sigma_{ij} = \lambda \delta_{ij} \varepsilon_{kk} + 2\mu \varepsilon_{ij} , \tag{2.6}$$

where the Kronecker delta is defined as $\delta_{ij} = \begin{cases} 0 & (i \neq j) \\ 1 & (i = j) \end{cases}$, and the volumetric strain is $\varepsilon_{kk} = \varepsilon_{11} + \varepsilon_{22} + \varepsilon_{33}$.

2.4 Voigt notation

The Voigt notation is a way to simplify the representation of a symmetric tensor by reducing its order. The stiffness and compliance tensors are rank-4 tensors denoted as 3x3x3x3 matrices. This notation is complicated and we use the Voigt notation to simplify these expressions. In the Voigt notation, the stress and strain tensors are written as six element column vectors rather than 3x3 matrices under the following replacement rules: 11 →1, 22→2, 33→3, 23 & 32→4, 13 & 31→5, and 12 & 21→6. The rules could be expressed as follows:

$$(\sigma)=\begin{pmatrix}\sigma_{11}\\ \sigma_{22}\\ \sigma_{33}\\ \sigma_{23}\\ \sigma_{31}\\ \sigma_{12}\end{pmatrix}=\begin{pmatrix}\sigma_{1}\\ \sigma_{2}\\ \sigma_{3}\\ \sigma_{4}\\ \sigma_{5}\\ \sigma_{6}\end{pmatrix}, \tag{2.7}$$

and

$$(\varepsilon)=\begin{pmatrix}\varepsilon_{11}\\ \varepsilon_{22}\\ \varepsilon_{33}\\ 2\varepsilon_{23}\\ 2\varepsilon_{31}\\ 2\varepsilon_{12}\end{pmatrix}=\begin{pmatrix}\varepsilon_{1}\\ \varepsilon_{2}\\ \varepsilon_{3}\\ \varepsilon_{4}\\ \varepsilon_{5}\\ \varepsilon_{6}\end{pmatrix}. \tag{2.8}$$

In this way, a four-dimensional symmetric fourth-order tensor C_{ijkl} can be reduced to a 6×6 matrix C_{ij}:

$$C_{ij}=\begin{pmatrix}C_{11} & C_{12} & C_{13} & C_{14} & C_{15} & C_{16}\\ C_{21} & C_{22} & C_{23} & C_{24} & C_{25} & C_{26}\\ C_{31} & C_{32} & C_{33} & C_{34} & C_{35} & C_{36}\\ C_{41} & C_{42} & C_{43} & C_{44} & C_{45} & C_{46}\\ C_{51} & C_{52} & C_{53} & C_{54} & C_{55} & C_{56}\\ C_{61} & C_{62} & C_{63} & C_{64} & C_{65} & C_{66}\end{pmatrix}. \tag{2.9}$$

We only express the tensors in the Voigt notation for abbreviation purposes in notation. When we actually compute the forward modeling, we still use fourth rank tensors in the calculation.

2.5 Symmetry classes

The structure of the elastic stiffness tensor C_{ijkl} characterizes the symmetry of a medium, on both the variation of the elastic response with the propagation direction of waves and the number of its independent components. This in turn determines the velocities, polarizations and amplitudes of elastic waves travelling through the media (Crampin and McGonigle, 1981).

In the following, we show different symmetry systems and their elastic stiffness matrices (empty entries are zero) in the Voigt notation:

Elastic tensor in isotropic material: two independent elements (Lame constants λ and μ)

$$C_{ij} = \begin{pmatrix} \lambda+2\mu & \lambda & \lambda & & & \\ \lambda & \lambda+2\mu & \lambda & & & \\ \lambda & \lambda & \lambda+2\mu & & & \\ & & & \mu & & \\ & & & & \mu & \\ & & & & & \mu \end{pmatrix}. \qquad (2.10)$$

Elastic tensor in hexagonal or transversely isotropic (TI) materials: five independent elements:

$$C_{ij} = \begin{pmatrix} C_{11} & C_{12} & C_{13} & & & \\ C_{12} & C_{11} & C_{13} & & & \\ C_{13} & C_{13} & C_{33} & & & \\ & & & C_{44} & & \\ & & & & C_{44} & \\ & & & & & C_{66} \end{pmatrix}, C_{66} = (C_{11} - C_{12})/2. \qquad (2.11)$$

The transversely isotropic medium is symmetric about the axis that is normal to a plane of isotropy. For instance, the transversely isotropic (VTI) medium is symmetric about the vertical axis (3-axis) and the transversely isotropic (HTI) medium is symmetric about the horizontal symmetry axis (1-axis).

Elastic tensor in orthorhombic materials: nine independent elements:

$$C_{ij} = \begin{pmatrix} C_{11} & C_{12} & C_{13} & & & \\ C_{12} & C_{22} & C_{23} & & & \\ C_{13} & C_{23} & C_{33} & & & \\ & & & C_{44} & & \\ & & & & C_{55} & \\ & & & & & C_{66} \end{pmatrix}. \quad (2.12)$$

This tensor has the same null components as that for transversely isotropic (TI) media. The orthorhombic medium is characterized by three mutually orthogonal symmetry axes (1-axis, 2-axis and 3-axis).

2.6 Linear slip model for HTI media

The hexagonal symmetry is perhaps the most commonly considered symmetry class for seismic anisotropy studies in exploration geophysics. For hexagonally symmetric materials, there is a single rotational symmetry axis. The property of the material in directions perpendicular to this axis appear to be directionally invariant. For this reason, materials of this type are commonly described as being “transversely isotropic” or TI for short. The stiffness matrix of a TI medium includes five independent elastic constants. In my thesis, I focus on transversely isotropy (TI) which is the most commonly used anisotropy model in applied geophysics. When the symmetry axis of TI media is vertical, the media is referred to as vertical transverse isotropy or VTI or polar anisotropy (*Figure 1 (a)*). When the symmetry axis of TI media is horizontal, the media is called horizontal transverse isotropy or HTI or azimuthal anisotropy (*Figure 1(b)*).

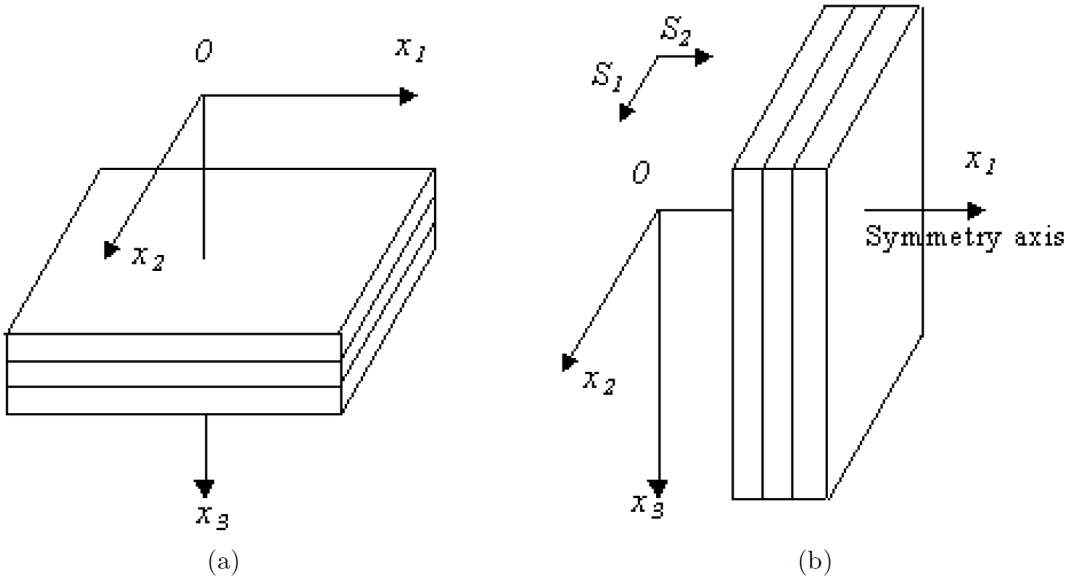

Figure 1 Symmetry-axis planes and isotropic planes in TI media: (a) VTI model; (b) HTI model. From Du *et al.* (2002).

In this section, I will focus on the linear slip (Schoenberg, 1980) fracture model for HTI. A system of vertically parallel fractures are embedded in an isotropic background medium. The thickness of each fracture is zero (i.e. represented by linear slip boundary conditions). The elastic properties of the fracture are described by the effective stiffness matrix of the medium (e.g., Schoenberg and Sayers, 1995; Fang *et al.*, 2017):

$$C = \begin{pmatrix} M(1-\delta_N) & \lambda(1-\delta_N) & \lambda(1-\delta_N) & & & \\ \lambda(1-\delta_N) & M(1-r^2\delta_N) & \lambda(1-r\delta_N) & & & \\ \lambda(1-\delta_N) & \lambda(1-r\delta_N) & M(1-r^2\delta_N) & & & \\ & & & \mu & & \\ & & & & \mu(1-\delta_T) & \\ & & & & & \mu(1-\delta_T) \end{pmatrix}, \qquad (2.13)$$

where

$$M = \lambda + 2\mu, \qquad (2.14)$$

$$r = \frac{\lambda}{M}, \qquad (2.15)$$

$$\delta_N = \frac{d_f Z_N M}{1 + d_f Z_N M}, \qquad (2.16)$$

$$\delta_T = \frac{d_f Z_T \mu}{1 + d_f Z_T \mu}, \qquad (2.17)$$

and λ, μ are the Lame constants, Z_N is normal compliance of a single fracture, Z_T is tangential compliance of a single fracture, and d_f is fracture spatial density (the number of fractures per meter).

When d_f equals zero, there is no fracture, and we get the familiar stiffness for isotropic medium.

2.7 Plane waves in anisotropic media and the Green-Christoffel equation

In this section, I will solve for the seismic wave propagation in the form of plane waves in the anisotropic medium in the frequency-space domain. In general, it is difficult to find an analytical solution of the wavefield directly in anisotropic media. Typically, we consider the wavefield as a superposition of plane waves with a certain wave vector and frequency, each with its own amplitude. The amplitude of each wave is a coefficient that will be determined by the initial or boundary conditions.

For a layered medium, we can decompose (in the most general case) the wavefield in each layer into six plane waves: three upgoing wavefields (upgoing P, SV, and SH) and three downgoing wavefields (downgoing P, SV, and SH). Each plane wave can be expressed as:

$$u_i\left(\boldsymbol{x},\omega\right) = A_n t_i^{(n)} \exp\left[i\boldsymbol{k}_n \bullet \boldsymbol{x}\right],\ i = 1,2,3,\ n = 1,\ldots,6\,, \tag{2.18}$$

where A_n is the n-th coefficient for the plane wave amplitude, $\boldsymbol{k}_n = (k_1^{(n)}, k_2^{(n)}, k_3^{(n)})$ is the n-th wavenumber indicating the wave propagation direction, $t_i^{(n)}$ is the n-th wave polarization vector for the i-th component. The bold variables are used to represent vectors. The number n from 1 to 6 denotes three downgoing and three upgoing transmitted waves in the anisotropic medium, summarized as follow:

$$n = \begin{cases} 1: \ \textit{downgoing P wave} \\ 2: \ \textit{downgoing slow S wave} \\ 3: \ \textit{downgoing fast S wave} \\ 4: \ \textit{upgoing P wave} \\ 5: \ \textit{upgoing slow S wave} \\ 6: \ \textit{upgoing fast S wave} \end{cases} .$$

Each of the six waves above must satisfy the wave equation. The elastodynamic equation of motion (frequency domain) in a homogeneous anisotropic medium can be written as:

$$-\omega^2 \rho u_{\boldsymbol{i}} = C_{ijkl} u_{\boldsymbol{k'lj}}, \; i, j, k, l = 1, 2, 3, \tag{2.19}$$

where u_i is the *i*-th component of the displacement, $u_{\boldsymbol{k'lj}}$ is the derivative of displacement with respect to the spatial coordinates *l* and *j*. In order to avoid ambiguity in the following text, we replace the $ijkl$ subscript in C_{ijkl} with $pqlm$. Substituting Equation (2.18) into (2.19), we can get:

$$-\omega^2 \rho A_n t_i^{(n)} \exp\left[i\boldsymbol{k}_n \bullet \boldsymbol{x} \right] = C_{pqlm} \left(ik_q^{(n)} \right)\left(ik_m^{(n)} \right) A_n t_i^{(n)} \exp\left[i\boldsymbol{k}_n \bullet \boldsymbol{x} \right], p, q, l, m = 1, 2, 3; \; n = 1, ..., 6$$

. (2.20)

In Equation (2.20), $k_q^{(n)}$ is the *q*-th component of the *n*-th plane wavenumber indicating propagation direction and phase velocities. There are six different vector plane wavenumbers. Simplifying Equation (2.20), we get:

$$-\omega^2 \rho \delta_{pl} t_i^{(n)} \exp\left[i\boldsymbol{k}_n \bullet \boldsymbol{x} \right] + C_{pqlm} k_q^{(n)} k_m^{(n)} t_i^{(n)} \exp\left[i\boldsymbol{k}_n \bullet \boldsymbol{x} \right] = 0, \; p, q, l, m = 1, 2, 3, \; n = 1, ..., 6,$$

(2.21)

where

$$\delta_{pl} = \begin{cases} 1, p = l \\ 0, p \neq l \end{cases}. \tag{2.22}$$

Combing similar terms, we obtain:

$$\left[-\omega^2\rho\delta_{pl}+C_{pqlm}k_q^{(n)}k_m^{(n)}\right]t_i^{(n)}\exp\left[i\boldsymbol{k}_n\bullet\boldsymbol{x}\right]=0,\, p,q,l,m=1,3\,, \qquad (2.23)$$

which could be written as:

$$\left[-\omega^2\rho\delta_{pl}+C_{pqlm}k_q^{(n)}k_m^{(n)}\right]t_i^{(n)}=0,\, p,q,l,m=1,2,3,\; n=1,...,6\,. \qquad (2.24)$$

Equation (2.24) is the Green-Christoffel equation. The 2nd-rank tensor $\Gamma_{pl}=C_{pqlm}k_qk_m$ is the Green-Christoffel tensor that depends both on elastic tensor of the medium and on the direction of the wave propagation direction.

Here, we need to determine the six different solutions of wave polarization vector $\boldsymbol{t}^{(n)}$ (n=1, …, 6). For different values of *n*, we will get different wave polarization vectors of six different plane waves in three components as follows:

$$\boldsymbol{t}^{(1)}=\left(\psi_1^{(1)},\psi_2^{(1)},\psi_3^{(1)}\right), \qquad (2.25)$$

$$\boldsymbol{t}^{(2)}=\left(\psi_1^{(2)},\psi_2^{(2)},\psi_3^{(2)}\right), \qquad (2.26)$$

$$\boldsymbol{t}^{(3)}=\left(\psi_1^{(3)},\psi_2^{(3)},\psi_3^{(3)}\right), \qquad (2.27)$$

$$\boldsymbol{t}^{(4)}=\left(\psi_1^{(4)},\psi_2^{(4)},\psi_3^{(4)}\right), \qquad (2.28)$$

$$\boldsymbol{t}^{(5)}=\left(\psi_1^{(5)},\psi_2^{(5)},\psi_3^{(5)}\right), \qquad (2.29)$$

$$\boldsymbol{t}^{(6)}=\left(\psi_1^{(6)},\psi_2^{(6)},\psi_3^{(6)}\right). \qquad (2.30)$$

2.7.1 Determine wavenumbers and polarization vectors

If we want to solve Equation (2.24), we need to determine the values of polarization vectors $\boldsymbol{t}^{(n)}\left(n=1,\ \ldots,\ 6\right)$ and wavenumber $\boldsymbol{k}^{(n)}\left(n=1,\ \ldots,\ 6\right)$ for each of the six plane waves. For a horizontally layered medium, when $\boldsymbol{k}^{(n)}=\left(k_1^{(n)},k_2^{(n)},k_3^{(3)}\right)$, the X- (or 1-component) and Y- (or 2-component) component of wavenumber $\boldsymbol{k}^{(n)}\left(n=1,\ \ldots,\ 6\right)$ will be the same as those of the incidence plane wave in all layers under the Snell's Law. For the *n*-th plane wave, we can write the matrix $A_{pl}^{(n)}$ as:

$$A_{pl}^{(n)}=-\omega^2\rho\delta_{pl}+C_{pqlm}k_q^{(n)}k_m^{(n)},\ p,q,l,m=1,2,3,\ n=1,...,6\,. \tag{2.31}$$

In order to get a nontrivial solution for Equation (2.24), i.e., $\boldsymbol{t}_i^{(n)}\neq 0\ \left(i=1,2,3;\ n=1,...,6\right)$, the determinant of matrix $A_{pl}^{(n)}$ must be zero. We then must have:

$$\left|A_{pl}^{(n)}\right|=0,\ \ p,l=1,2,3,\ n=1,...,6\,, \tag{2.32}$$

which can also be explicitly expressed as:

$$\left|-\omega^2\rho\delta_{pl}+C_{pqlm}k_q^{(n)}k_m^{(n)}\right|=0,\ \ p,q,l,m=1,2,3,\ n=1,...,6\,. \tag{2.33}$$

We can write Equation (2.24) as:

$$A_{pl}^{(n)}\boldsymbol{t}_i^{(n)}=0,\ p,l,i=1,2,3,\ n=1,...,6\,. \tag{2.34}$$

For instance, let *n*=1 (the first plane wave), we have:

$$A_{pl}\boldsymbol{x}=\boldsymbol{0}\,, \tag{2.35}$$

where $\boldsymbol{x}=\left(\psi_1^{(1)},\psi_2^{(1)},\psi_3^{(1)}\right)$. To find the nontrivial ***x*,** we could decompose matrix A_{pq} by the eigen decomposition:

$$A_{pl}=VDV^{-1}, \tag{2.36}$$

where

$$D=\begin{pmatrix}\lambda_1 & & \\ & \lambda_2 & \\ & & \lambda_3\end{pmatrix}, \qquad (2.37)$$

is the diagonal matrix of eigenvalues of matrix A_{pl}, the *i-th* column of matrix V is the eigen-vector associated with λ_i. Substituting Equation (2.36) into (2.35), we obtain:

$$VDV^{-1}\boldsymbol{x}=\boldsymbol{0}\,. \qquad (2.38)$$

Let $\boldsymbol{y}=V^{-1}\boldsymbol{x}$, we have:

$$D\boldsymbol{y}=\boldsymbol{0}\,. \qquad (2.39)$$

Substituting Equation (2.37) into (2.39), we have:

$$\begin{pmatrix}\lambda_1 & & \\ & \lambda_2 & \\ & & \lambda_3\end{pmatrix}\begin{pmatrix}y_1\\ y_2\\ y_3\end{pmatrix}=0\,, \qquad (2.40)$$

where $\boldsymbol{y}=(y_1,y_2,y_3)$. In order to get a unique solution, we let λ_1 be zero. Then $\boldsymbol{y}$ turns into $\boldsymbol{y}=(y_1,0,0)$. According to the relation that

$$\boldsymbol{x}=V\boldsymbol{y}\,, \qquad (2.41)$$

we can obtain the following equation to solve for the $\boldsymbol{x}$ vector:

$$x=\begin{pmatrix}V_{11} & V_{12} & V_{13}\\ V_{21} & V_{22} & V_{23}\\ V_{31} & V_{32} & V_{33}\end{pmatrix}\begin{pmatrix}y_1\\ 0\\ 0\end{pmatrix}. \qquad (2.42)$$

The solution of $\boldsymbol{x}$ can be obtained by using y_1 multiple the first column of matrix V. The equation can be written as:

$$x=y_1\left(V_{11},V_{21},V_{31}\right), \qquad (2.43)$$

which is the normalized polarization vector $\boldsymbol{t}^{(1)}$ of downgoing P wave.

Using a similar method, we can also obtain the other five polarization vectors of downgoing slow S wave ($\boldsymbol{t}^{(2)}$), downgoing fast S wave ($\boldsymbol{t}^{(3)}$), upgoing P wave ($\boldsymbol{t}^{(4)}$), upgoing slow S wave ($\boldsymbol{t}^{(5)}$) and upgoing fast S wave ($\boldsymbol{t}^{(6)}$).

Chapter 3

Reflection and Transmission Coefficients for HTI Media

3.1 Introduction

The purpose of this chapter is to investigate the reflection and transmission coefficients indicating the amplitudes of the plane waves in the anisotropic medium. I use a three-layered model to calculate the anisotropic reflection and transmission coefficients for an incidence P plane wave. The three-layered model has an isotropic upper layer, an anisotropic middle layer, and an isotropic bottom layer.

3.2 Three-layered model

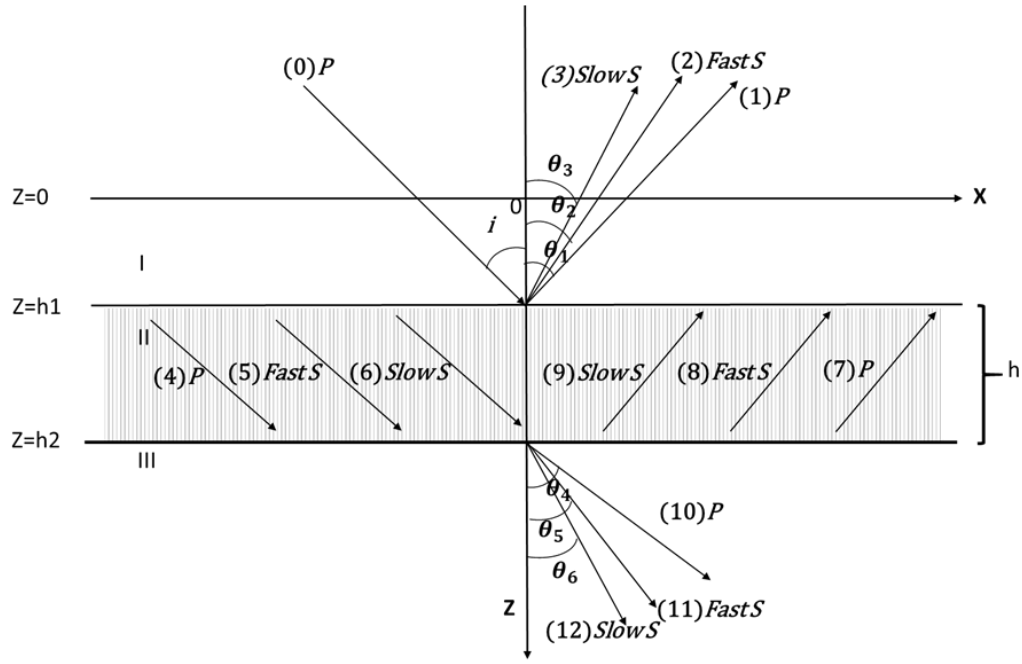

Figure 2 Reflected and transmitted waves caused by a P plane wave incidence for three-layered model.

For the model (*Figure 2*), medium-I is isotropic. Medium-II is an HTI medium with vertical fractures embedded in an isotropic background that has the same background velocity as medium-I. I used the linear-slip model (Schoenberg and Sayers, 1995) as my fracture model in medium-II. Medium-III is an isotropic layer with the same properties as layer 1. Number (0), (1), (2), (3), (4), (5), (6), (7), (8), (9), (10), (11), (12) denote P plane wave incidence, reflected P wave, reflected fast S wave and reflected slow S wave in layer 1; transmitted downgoing P wave, transmitted downgoing fast S wave, transmitted downgoing slow S wave, transmitted upgoing P wave, transmitted upgoing fast S wave and transmitted upgoing slow S wave in layer 2; transmitted P wave, transmitted fast S wave and transmitted slow S wave in layer 3 (Figure *2*). Here, i is the incidence angle, $\theta_1, \theta_2, \theta_3$ are the reflected angles of reflected P wave, fast S wave and slow S wave, respectively (*Figure 2*). The Y direction points into the page, following the right-hand rule. The fast S wave in layer 2 is polarized in the Y-Z plane parallel to the fracture system, while the slow S wave is polarized in X-Z plane perpendicular to the fracture system.

In three-layered model case, we will have all six plane waves in the middle layer which is the HTI medium: upgoing P to P and downgoing P to P, upgoing P to SV and downgoing P to SV, upgoing P to SH and downgoing P to SH. Respectively, we have six transmission coefficients to determine in layer 2. And three reflection coefficients in layer 1 and three transmission coefficients in layer 3 to determine. In this case, we need to solve twelve reflection/transmission (R/T) coefficients in total.

We will move on to calculate the reflection and transmission coefficients of the three-layered model. We can determine the coefficients from the boundary conditions.

3.2.1 Boundary conditions

Two kinds of boundary conditions are used at a solid-solid interface. They are:

$$u_j^+ = u_j^-, \; j = 1, 2, 3, \tag{3.1}$$

and

$$\sigma_{3j}^+ = \sigma_{3j}^-, \; j = 1, 2, 3. \tag{3.2}$$

In Equation (3.1), u_j^+ denotes the displacement of one side of the boundary and u_j^- denotes the displacement of the other side. Equation (3.1) describes the displacement continuity at the boundary. In Equation (3.2), σ_{3j}^+ denotes the traction of one side of the boundary and σ_{3j}^- denotes the traction of the other side of the boundary. Equation (3.2) describes the traction continuity at the boundary, where $j = 1, 2, 3$ denotes three different components: 1 is the X- component, 2 is the Y- component and 3 is the Z-component.

We will deal with the displacement continuity first. In the following text, the label (I), (II) and III represent layers 1, 2 and 3, respectively. The displacement of *P* plane wave incidence is given by:

$$u_i^0 = k_P^0 \exp\left[i\boldsymbol{k}_P^0 \bullet \boldsymbol{x} \right], \tag{3.3}$$

where $k_P^0 = \left(k_1, k_2, k_3^0\right)$ is the polarization vector of the incidence P plane wave, $\boldsymbol{k}_P^0$ is the wavenumber $\boldsymbol{k}_P^0 = \dfrac{\omega}{v_P} k_P^0$ of the incidence wave where v_P is the P-wave propagation velocity. The incidence wavefield in layer 1 could be expressed on the three components as:

$$u_1^0 = k_1 \exp\left[i\left(k_1 x + k_2 y + k_3^0 z\right)\right], \tag{3.4}$$

$$u_2^0 = k_2 \exp\left[i\left(k_1 x + k_2 y + k_3^0 z\right)\right], \tag{3.5}$$

$$u_3^0 = k_3^0 \exp\left[i\left(k_1 x + k_2 y + k_3^0 z\right)\right]. \tag{3.6}$$

In **Chapter 2**, we have discussed that the X- and Y- component of wavenumber should be the same as that of the incidence wave in each layer under the Snell's Law. We fix the X- and Y- component of wavenumbers as constants for all plane waves and refer to them as k_1 and k_2, respectively.

The displacement of reflected P wave in layer 1 could be expressed on the three components as:

$$u_{P1}^{(I)} = R_P \xi_{P1} \exp\left[i\left(k_1 x + k_2 y + k_P^{(I)} z\right)\right], \tag{3.7}$$

$$u_{P2}^{(I)} = R_P \xi_{P2} \exp\left[i\left(k_1 x + k_2 y + k_P^{(I)} z\right)\right], \tag{3.8}$$

$$u_{P3}^{(I)} = R_P \xi_{P3} \exp\left[i\left(k_1 x + k_2 y + k_P^{(I)} z\right)\right], \tag{3.9}$$

where R_p is the reflection coefficient of reflected P wave in layer 1, $\boldsymbol{\xi_p}$ is the polarization vector of reflected P wave, $\boldsymbol{\xi_p} = \left(\xi_{P1}, \xi_{P2}, \xi_{P3}\right)$ is a normalized unit vector, $k_P^{(I)}$ is the Z- component of the wavenumber of reflected P wave in layer 1.

The displacement of reflected SV wave in layer 1 could be expressed on the three components as:

$$u_{SV1}^{(I)} = R_{SV}\xi_{SV1}\exp\left[i\left(k_1x + k_2y + k_{SV}^{(I)}z\right)\right], \tag{3.10}$$

$$u_{SV2}^{(I)} = R_{SV}\xi_{SV2}\exp\left[i\left(k_1x + k_2y + k_{SV}^{(I)}z\right)\right], \tag{3.11}$$

$$u_{SV3}^{(I)} = R_{SV}\xi_{SV3}\exp\left[i\left(k_1x + k_2y + k_{SV}^{(I)}z\right)\right], \tag{3.12}$$

where R_{SV} is the reflectivity coefficient of reflected SV wave in layer 1, $\boldsymbol{\xi_{SV}}$ is the polarization vector of reflected SV wave, $\boldsymbol{\xi_{SV}} = \left(\xi_{SV1}, \xi_{SV2}, \xi_{SV3}\right)$ is a normalized unit vector, $k_{SV}^{(I)}$ is the Z- component of the wavenumber of reflected SV wave in layer 1.

The displacement of reflected SH wave in layer 1 could be expressed on the three components as:

$$u_{SH1}^{(I)} = R_{SH}\xi_{SH1}\exp\left[i\left(k_1x + k_2y + k_{SH}^{(I)}z\right)\right], \tag{3.13}$$

$$u_{SH2}^{(I)} = R_{SH}\xi_{SH2}\exp\left[i\left(k_1x + k_2y + k_{SH}^{(I)}z\right)\right], \tag{3.14}$$

$$u_{SH3}^{(I)} = R_{SH}\xi_{SH3}\exp\left[i\left(k_1x + k_2y + k_{SH}^{(I)}z\right)\right], \tag{3.15}$$

where R_{SH} is the reflection coefficient of reflected SH wave in layer 1, $\boldsymbol{\xi_{SH}}$ is the polarization vector of reflected SH wave, $\boldsymbol{\xi_{SH}} = \left(\xi_{SH1}, \xi_{SH2}, \xi_{SH3}\right)$ is a normalized unit vector, $k_{SH}^{(I)}$ is the Z- component of the wavenumber of reflected SH wave in layer 1.

The total displacement in medium-I could be written as follows on the three components (X-, Y- and Z- components):

$$u_1^{(I)} = u_1^0 + u_{P1}^{(I)} + u_{SV1}^{(I)} + u_{SH1}^{(I)}, \tag{3.16}$$

$$u_2^{(I)} = u_2^0 + u_{P2}^{(I)} + u_{SV2}^{(I)} + u_{SH2}^{(I)}, \tag{3.17}$$

$$u_3^{(I)} = u_3^0 + u_{P3}^{(I)} + u_{SV3}^{(I)} + u_{SH3}^{(I)}. \tag{3.18}$$

Medium-II is an HTI medium. There are six types of transmitted waves propagating in layer 2: downgoing P, converted downgoing SV, downgoing SH, upgoing P, upgoing SV and upgoing SH. Respectively, we have six transmission coefficients to determine.

The displacement of transmitted downgoing P wave in layer 2 could be expressed on the three components as:

$$u_{Pd1}^{(II)} = T_{Pd}^{(II)} \psi_{Pd1} \exp\left[i\left(k_1 x + k_2 y + k_{Pd}^{(II)} z \right) \right], \tag{3.19}$$

$$u_{Pd2}^{(II)} = T_{Pd}^{(II)} \psi_{Pd2} \exp\left[i\left(k_1 x + k_2 y + k_{Pd}^{(II)} z \right) \right], \tag{3.20}$$

$$u_{Pd3}^{(II)} = T_{Pd}^{(II)} \psi_{Pd3} \exp\left[i\left(k_1 x + k_2 y + k_{Pd}^{(II)} z \right) \right], \tag{3.21}$$

where $T_{Pd}^{(II)}$ is the transmission coefficient of downgoing transmitted P wave in layer 2, $\boldsymbol{\psi_{Pd}}$ is the polarization vector of transmitted downgoing P wave, $\boldsymbol{\psi_{Pd}} = \left(\psi_{Pd1}, \psi_{Pd2}, \psi_{Pd3} \right)$ is a normalized unit vector, $k_{Pd}^{(II)}$ is the Z- component of the wavenumber of transmitted downgoing P wave in layer 2.

The displacement of transmitted downgoing SV wave in layer 2 could be expressed on the three components as:

$$u_{SVd1}^{(II)} = T_{SVd}^{(II)} \psi_{SVd1} \exp\left[i\left(k_1 x + k_2 y + k_{SVd}^{(II)} z \right) \right], \tag{3.22}$$

$$u_{SVd2}^{(II)} = T_{SVd}^{(II)} \psi_{SVd2} \exp\left[i\left(k_1 x + k_2 y + k_{SVd}^{(II)} z \right) \right], \tag{3.23}$$

$$u_{SVd3}^{(II)} = T_{SVd}^{(II)} \psi_{SVd3} \exp\left[i\left(k_1 x + k_2 y + k_{SVd}^{(II)} z \right) \right], \tag{3.24}$$

where $T_{SVd}^{(II)}$ is the transmission coefficient of downgoing transmitted slow S wave in layer 2, $\boldsymbol{\psi_{SVd}}$ is the polarization vector of transmitted downgoing slow S wave, $\boldsymbol{\psi_{SVd}} = (\psi_{SVd1}, \psi_{SVd2}, \psi_{SVd3})$ is a normalized unit vector, $k_{SVd}^{(II)}$ is the Z- component of the wavenumber of transmitted downgoing SV wave in layer 2.

The displacement of transmitted downgoing SH wave in layer 2 could be expressed on the three components as:

$$u_{SHd1}^{(II)} = T_{SHd}^{(II)} \psi_{SHd1} \exp\left[i\left(k_1 x + k_2 y + k_{SHd}^{(II)} z \right) \right], \tag{3.25}$$

$$u_{SHd2}^{(II)} = T_{SHd}^{(II)} \psi_{SHd2} \exp\left[i\left(k_1 x + k_2 y + k_{SHd}^{(II)} z \right) \right], \tag{3.26}$$

$$u_{SHd3}^{(II)} = T_{SHd}^{(II)} \psi_{SHd3} \exp\left[i\left(k_1 x + k_2 y + k_{SHd}^{(II)} z \right) \right], \tag{3.27}$$

where $T_{SHd}^{(II)}$ is the transmission coefficient of downgoing transmitted fast S wave in layer 2, $\boldsymbol{\psi_{SHd}}$ is the polarization vector of transmitted downgoing fast S wave, $\boldsymbol{\psi_{SHd}} = (\psi_{SHd1}, \psi_{SHd2}, \psi_{SHd3})$ is a normalized unit vector, $k_{SHd}^{(II)}$ is the Z- component of the wavenumber of transmitted downgoing SH wave in layer 2.

The displacement of transmitted upgoing P wave in layer 2 could be expressed on the three components as:

$$u_{Pu1}^{(II)} = T_{Pu}^{(II)} \psi_{Pu1} \exp\left[i\left(k_1 x + k_2 y + k_{Pu}^{(II)} z \right) \right], \tag{3.28}$$

$$u_{Pu2}^{(II)} = T_{Pu}^{(II)} \psi_{Pu2} \exp\left[i\left(k_1 x + k_2 y + k_{Pu}^{(II)} z \right) \right], \tag{3.29}$$

$$u_{Pu3}^{(II)} = T_{Pu}^{(II)} \psi_{Pu3} \exp\left[i\left(k_1 x + k_2 y + k_{Pu}^{(II)} z \right) \right], \tag{3.30}$$

where $T_{Pu}^{(II)}$ is the transmission coefficient of transmitted upgoing P wave in layer 2, ψ_{Pu} is the polarization vector of transmitted upgoing P wave, $\psi_{Pu} = (\psi_{Pu1}, \psi_{Pu2}, \psi_{Pu3})$

is a normalized unit vector, $k_{Pu}^{(II)}$ is the Z- component of the wavenumber of transmitted upgoing P wave in layer 2.

The displacement of transmitted upgoing SV wave in layer 2 could be expressed on the three components as:

$$u_{SVu1}^{(II)} = T_{SVu}^{(II)} \psi_{SVu1} \exp\left[i\left(k_1 x + k_2 y + k_{SVu}^{(II)} z \right) \right], \tag{3.31}$$

$$u_{SVu2}^{(II)} = T_{SVu}^{(II)} \psi_{SVu2} \exp\left[i\left(k_1 x + k_2 y + k_{SVu}^{(II)} z \right) \right], \tag{3.32}$$

$$u_{SVu3}^{(II)} = T_{SVu}^{(II)} \psi_{SVu3} \exp\left[i\left(k_1 x + k_2 y + k_{SVu}^{(II)} z \right) \right], \tag{3.33}$$

where $T_{SVu}^{(II)}$ is the transmission coefficient of transmitted upgoing SV wave in layer 2, ψ_{SVu} is the polarization vector of transmitted upgoing SV wave, $\psi_{SVu} = \left(\psi_{SVu1}, \psi_{SVu2}, \psi_{SVu3} \right)$ is a normalized unit vector, $k_{SVu}^{(II)}$ is the Z- component of the wavenumber of transmitted upgoing SV wave in layer 2.

The displacement of transmitted upgoing SH wave in layer 2 could be expressed on the three components as:

$$u_{SHu1}^{(II)} = T_{SVu}^{(II)} \psi_{SHu1} \exp\left[i\left(k_1 x + k_2 y + k_{SHu}^{(II)} z \right) \right], \tag{3.34}$$

$$u_{SHu2}^{(II)} = T_{SVu}^{(II)} \psi_{SHu2} \exp\left[i\left(k_1 x + k_2 y + k_{SHu}^{(II)} z \right) \right], \tag{3.35}$$

$$u_{SHu3}^{(II)} = T_{SVu}^{(II)} \psi_{SHu3} \exp\left[i\left(k_1 x + k_2 y + k_{SHu}^{(II)} z \right) \right], \tag{3.36}$$

where $T_{SHu}^{(II)}$ is the transmission coefficient of transmitted upgoing SH wave in layer 2, ψ_{SHu} is the polarization vector of transmitted upgoing SH wave, $\psi_{SHu} = \left(\psi_{SHu1}, \psi_{SHu2}, \psi_{SHu3} \right)$ is a normalized unit vector, $k_{SHu}^{(II)}$ is the Z- component of the wavenumber of transmitted upgoing SH wave in layer 2.

The total displacement in medium-II could be expressed on the three components (X-, Y- and Z- components) as:

$$u_1^{(II)} = u_{1Pd}^{(II)} + u_{1SVd}^{(II)} + u_{1SHd}^{(II)} + u_{1Pu}^{(II)} + u_{1SVu}^{(II)} + u_{1SHu}^{(II)}, \tag{3.37}$$

$$u_2^{(II)} = u_{2Pd}^{(II)} + u_{2SVd}^{(II)} + u_{2SHd}^{(II)} + u_{2Pu}^{(II)} + u_{2SVu}^{(II)} + u_{2SHu}^{(II)}, \tag{3.38}$$

$$u_3^{(II)} = u_{3Pd}^{(II)} + u_{3SVd}^{(II)} + u_{3SHd}^{(II)} + u_{3Pu}^{(II)} + u_{3SVu}^{(II)} + u_{3SHu}^{(II)}. \tag{3.39}$$

Layer 3 is isotropic. We have three transmitted waves in medium III: downgoing P wave, downgoing fast S wave, downgoing slow S wave.

The displacement of transmitted P wave in layer 3 could be expressed on the three components as:

$$u_{P1}^{(III)} = T_P^{(III)} \tau_{P1} \exp\left[i\left(k_1 x + k_2 y + k_P^{(III)} \right) \right], \tag{3.40}$$

$$u_{P2}^{(III)} = T_P^{(III)} \tau_{P2} \exp\left[i\left(k_1 x + k_2 y + k_P^{(III)} \right) \right], \tag{3.41}$$

$$u_{P3}^{(III)} = T_P^{(III)} \tau_{P3} \exp\left[i\left(k_1 x + k_2 y + k_P^{(III)} \right) \right]. \tag{3.42}$$

where $T_P^{(III)}$ is the transmission coefficient of transmitted downgoing P wave in layer 3, τ_P is the polarization vector of transmitted downgoing P wave, $\tau_P = \left(\tau_{P1}, \tau_{P2}, \tau_{P3} \right)$ is a normalized unit vector, $k_P^{(III)}$ is the Z component of the wavenumber of transmitted downgoing P wave in layer 3.

The displacement of transmitted SV wave in layer 3 could be expressed on the three components as:

$$u_{SV1}^{(III)} = T_{SV}^{(III)} \tau_{SV1} \exp\left[i\left(k_1 x + k_2 y + k_{SV}^{(III)} \right) \right], \tag{3.43}$$

$$u_{SV2}^{(III)} = T_{SV}^{(III)} \tau_{SV2} \exp\left[i\left(k_1 x + k_2 y + k_{SV}^{(III)} \right) \right], \tag{3.44}$$

$$u_{SV3}^{(III)} = T_{SV}^{(III)} \tau_{SV3} \exp\left[i\left(k_1 x + k_2 y + k_{SV}^{(III)} \right) \right]. \tag{3.45}$$

where $T_{SV}^{(III)}$ is the transmission coefficient of transmitted downgoing SV wave in layer 3, τ_{SV} is the polarization vector of transmitted downgoing SV wave, $\tau_{SV} = \left(\tau_{SV1}, \tau_{SV2}, \tau_{SV3} \right)$ is a normalized unit vector, $k_{SV}^{(III)}$ is the Z- component of the wavenumber of transmitted downgoing SV wave in layer 3.

The displacement of transmitted SH wave in layer 3 could be expressed on the three components as:

$$u_{SH1}^{(III)} = T_{SH}^{(III)} \tau_{SH1} \exp\left[i\left(k_1 x + k_2 y + k_{SH}^{(III)} \right) \right], \tag{3.46}$$

$$u_{SH2}^{(III)} = T_{SH}^{(III)} \tau_{SH2} \exp\left[i\left(k_1 x + k_2 y + k_{SH}^{(III)} \right) \right], \tag{3.47}$$

$$u_{SH3}^{(III)} = T_{SH}^{(III)} \tau_{SH3} \exp\left[i\left(k_1 x + k_2 y + k_{SH}^{(III)} \right) \right]. \tag{3.48}$$

where $T_{SH}^{(III)}$ is the transmission coefficient of transmitted downgoing SH wave in layer 3, τ_{SH} is the polarization vector of transmitted downgoing SV wave, $\tau_{SH} = \left(\tau_{SH1}, \tau_{SH2}, \tau_{SH3} \right)$ is a normalized unit vector, $k_{SH}^{(III)}$ is the Z- component of the wavenumber of transmitted downgoing SH wave in layer 3.

The total displacement in medium-III could be expressed on the three components as:

$$u_1^{(III)} = u_{1P}^{(III)} + u_{1SV}^{(III)} + u_{1SH}^{(III)}, \tag{3.49}$$

$$u_2^{(III)} = u_{2P}^{(III)} + u_{2SV}^{(III)} + u_{2SH}^{(III)}, \tag{3.50}$$

$$u_3^{(III)} = u_{3P}^{(III)} + u_{3SV}^{(III)} + u_{3SH}^{(III)}. \tag{3.51}$$

According to Equation (3.1), when the depth $z = h_1$, we apply the continuity of displacement at the interface of medium-I and II. We can get the following Equations:

$$u_1^{(I)} = u_1^{(II)}, \tag{3.52}$$

$$u_2^{(I)} = u_2^{(II)}, \tag{3.53}$$

$$u_3^{(I)} = u_3^{(II)}. \tag{3.54}$$

Now we deal with the continuity of traction at the interface of medium-I and II. The traction vector could be described as:

$$T_i = \sigma_{ij} n_j,\ i, j = 1, 2, 3, \tag{3.55}$$

where n_j is the normal of the boundary, σ_{ij} is the stress tensor. Let $n_j = (0, 0, 1)$, we could get:

$$T_1 = \sigma_{13} n_3, \tag{3.56}$$

$$T_2 = \sigma_{23} n_3, \tag{3.57}$$

$$T_3 = \sigma_{33} n_3. \tag{3.58}$$

For the upper isotropic layer 1, we use Equation (2.6) in **Chapter 2** to express the relations between stress and strain. Substituting them into Equation (3.56), (3.57), and (3.58) respectively, we can obtain the equations of traction in the upper layer at the boundary as:

$$T_1^{(I)} = 2\mu\varepsilon_{13}^{(I)} n_3, \tag{3.59}$$

$$T_2^{(I)} = 2\mu\varepsilon_{23}^{(I)} n_3, \tag{3.60}$$

$$T_3^{(I)} = (\lambda\varepsilon_{kk}^{(I)} + 2\mu\varepsilon_{33}^{(I)}) n_3, \tag{3.61}$$

where

$$\varepsilon_{13}^{(I)} = \frac{1}{2}\left(\frac{\partial u_1^{(I)}}{\partial z} + \frac{\partial u_3^{(I)}}{\partial x}\right), \tag{3.62}$$

$$\varepsilon_{23}^{(I)} = \frac{1}{2}(\frac{\partial u_2^{(I)}}{\partial z} + \frac{\partial u_3^{(I)}}{\partial y}), \tag{3.63}$$

$$\varepsilon_{11}^{(I)} = \frac{\partial u_1^{(I)}}{\partial x} , \tag{3.64}$$

$$\varepsilon_{22}^{(I)} = \frac{\partial u_2^{(I)}}{\partial y} , \tag{3.65}$$

$$\varepsilon_{33}^{(I)} = \frac{\partial u_3^{(I)}}{\partial z} , \tag{3.66}$$

$$\varepsilon_{kk}^{(I)} = \varepsilon_{11}^{(I)} + \varepsilon_{22}^{(I)} + \varepsilon_{33}^{(I)}, \tag{3.67}$$

and $\varepsilon_{ij}^{(I)}\left(i,\, j = 1, 2, 3\right)$ is the strain tensor in layer 1, λ and μ are the Lame constants.

For the anisotropic layer, we use Equation (2.1) in **Chapter 2** (generalized Hooke's Law) to describe the relation between traction and stress. Therefore, the traction in medium-II at the boundary 1 could be expressed as:

$$T_1^{(II)} = C_{13mn}\varepsilon_{mn}^{(II)}, \tag{3.68}$$

$$T_2^{(II)} = C_{23mn}\varepsilon_{mn}^{(II)}, \tag{3.69}$$

$$T_3^{(II)} = C_{33mn}\varepsilon_{mn}^{(II)}, \tag{3.70}$$

here $m,\, n = 1, 2, 3$. According to Equation (3.2), we apply the continuity of traction at the interface of medium-I and medium-II when $z = h_1$. We have the following Equations:

$$T_1^{(I)} = T_1^{(II)}, \tag{3.71}$$

$$T_2^{(I)} = T_2^{(II)}, \tag{3.72}$$

$$T_3^{(I)} = T_3^{(II)}. \tag{3.73}$$

Applying the continuity of displacement when the depth $z = h_2$ at boundary 2, we obtain the following Equations:

$$u_1^{(II)} = u_1^{(III)}, \tag{3.74}$$

$$u_2^{(II)} = u_2^{(III)}, \tag{3.75}$$

$$u_3^{(II)} = u_3^{(III)}. \tag{3.76}$$

Applying the continuity of traction when the depth $z = h_2$ at the boundary, we could describe the traction at boundary 2 as:

$$T_1^{(II)} = T_1^{(III)}, \tag{3.77}$$

$$T_2^{(II)} = T_2^{(III)}, \tag{3.78}$$

$$T_3^{(II)} = T_3^{(III)}. \tag{3.79}$$

Based on the boundary conditions above, we have twelve Equations (Equation (3.52) ~ (3.54) and Equation (3.71) ~ (3.79)) with 12 unknown RT coefficients(R_p , R_{SV} , R_{SH} , $T_{Pd}^{(II)}$, $T_{SVd}^{(II)}$, $T_{SHd}^{(II)}$, $T_{Pu}^{(II)}$, $T_{SVu}^{(II)}$, $T_{SHu}^{(II)}$, $T_P^{(III)}$, $T_{SV}^{(III)}$, $T_{SH}^{(III)}$) in total. Solving the twelve Equations above, we will be able to calculate all twelve reflection/transmission (R/T) coefficients.

Chapter 4

Effect of Fracture Layer Thickness on Reflected *P* Wavefield

Fractures are important in oil field exploration and production, geotechnical, and hydrogeological applications because they provide pathways for fluid flow. Having a better understanding on how seismic waves respond to different fractured layers is necessary for seismic imaging and fracture characterization. In this chapter, I will investigate how the thickness of fractured layer will affect reflected P-wave amplitude as a function of azimuth. I will use the three-layered modeling for this work.

4.1 *P* wave amplitude variation with azimuth

For P waves, the main attributes we can use are the azimuthal variations of arrival times and amplitudes. We can obtain fracture orientation and density by analyzing seismic data. The fracture orientation could be inferred from the minimum traveltime, fastest normal move out (NMO) velocity, or azimuthal AVO gradient. Fracture density could be obtained from the anisotropic AVO gradient (Rüger, 2002). In order to investigate the P wave amplitude variation with different azimuths, we use a special data-acquisition geometry shown in map view in *Figure 3*. The azimuth is defined as the angle between the source-receiver line and the positive x-axis. We put the source (red star) at the origin (0, 0) which is the center of the circle. We place multiple receivers along the circle (blue triangles) at different azimuths. The offset (the distance from source to receiver) is the radius of the circle. In this way, the reflected wavefield could be recorded at these receivers at different azimuths. The fracture planes are oriented at azimuth 90 degrees.

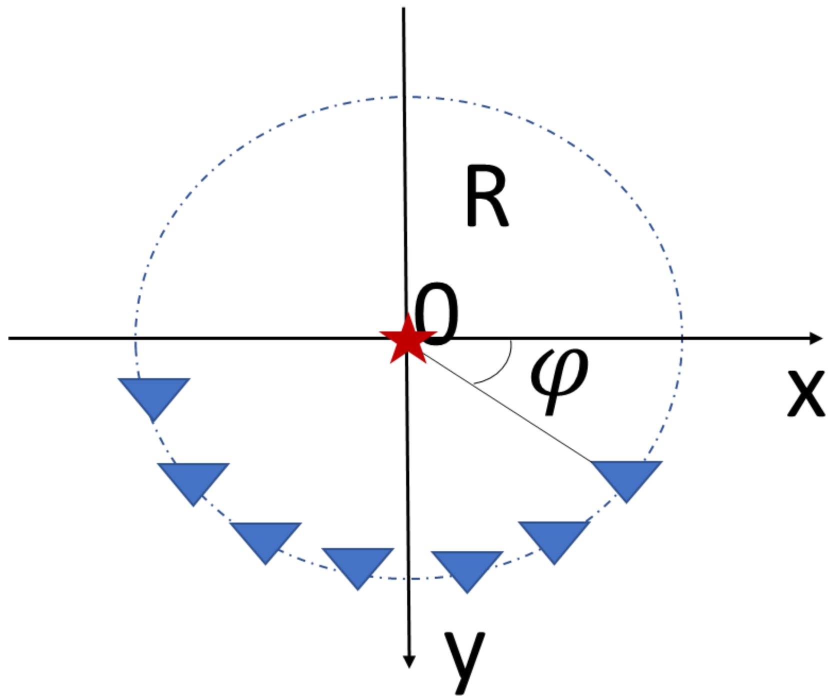

Figure 3 Schematic of the acquisition geometry for multiple receivers (map view). Red star represents the source location (0, 0, 0). Blue triangles represent receivers along the circle whose center is the source. Offset is the same value as the radius R (R=1000 m). The azimuth φ starts from positive x-axis, moving clockwise from 0 to 360 degrees every 10 degrees. The fracture plane strike is along the y-axis (i.e., 90-degree azimuth).

For my three-layer model, the second (middle) layer is the fractured layer while the first and third layer are isotropic half spaces. The medium properties of the first and the third layers are the same and we call them the background media. The background P wave velocity is 2500 m/s, and S wave is 1000 m/s. Density is set as 1000 kg/m³. The thickness of the first layer is always 500 m, while the thickness of the fractured layer varies from 1/4 of wavelength, one wavelength, 3 to 5 times of the P-wave wavelength.

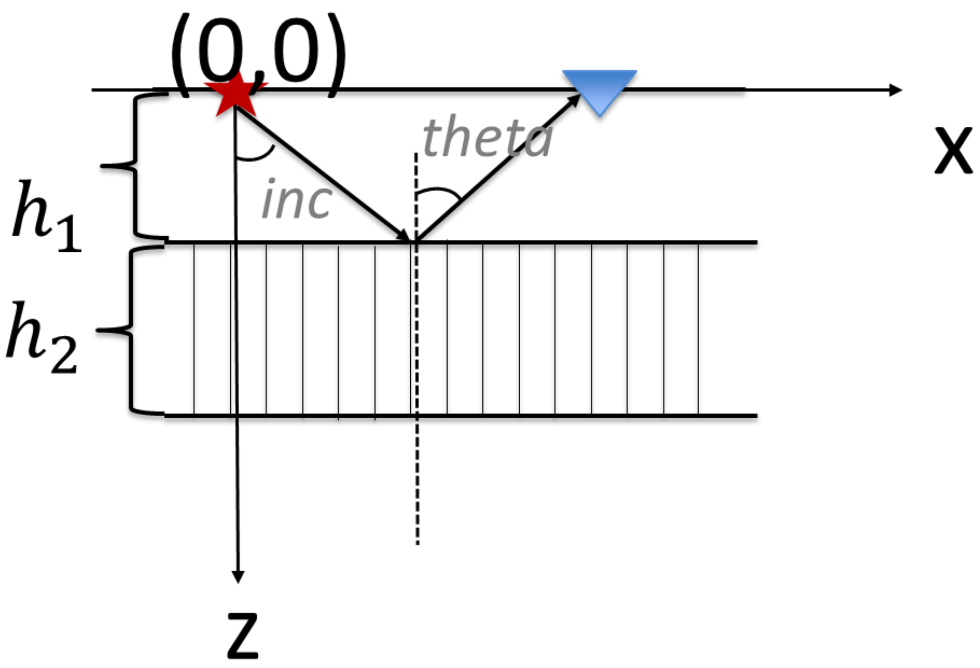

Figure 4 Schematic of a vertical cross-section of the fractured three-layer model. h_1 denotes the thickness of layer 1; h_2 denotes the thickness of fractured layer; *inc* denotes the incidence angle; *theta* denotes reflection angle of shear wave.

4.1.1 HTI case

I will investigate how the reflected P wave interacts with vertically parallel fractures embedded in the background medium. The reflected multicomponent P waves from the top and the bottom of the fractured layer are shown in *Figure 5*, *Figure 6*, and *Figure 7* for X-, Y- and Z- component respectively.

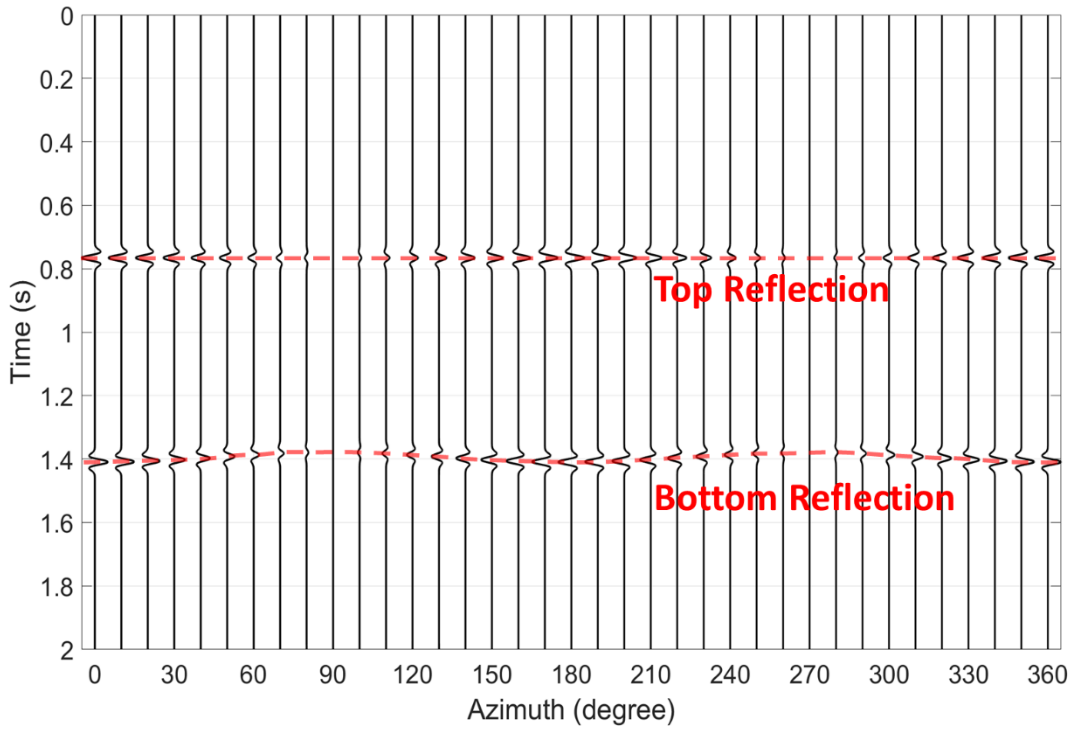

Figure 5 Reflections of *P* wave on the X- component at different azimuths when the thickness of fractured layer is 1000 m. The two background red stripes in each panel indicate reflections from top and bottom of the fractured layer. The source wavelet is a 20 Hz Ricker. The incidence wave is *P* wave. The incidence angle is 45 degrees. Fracture strike planes are along 90-degree azimuth.

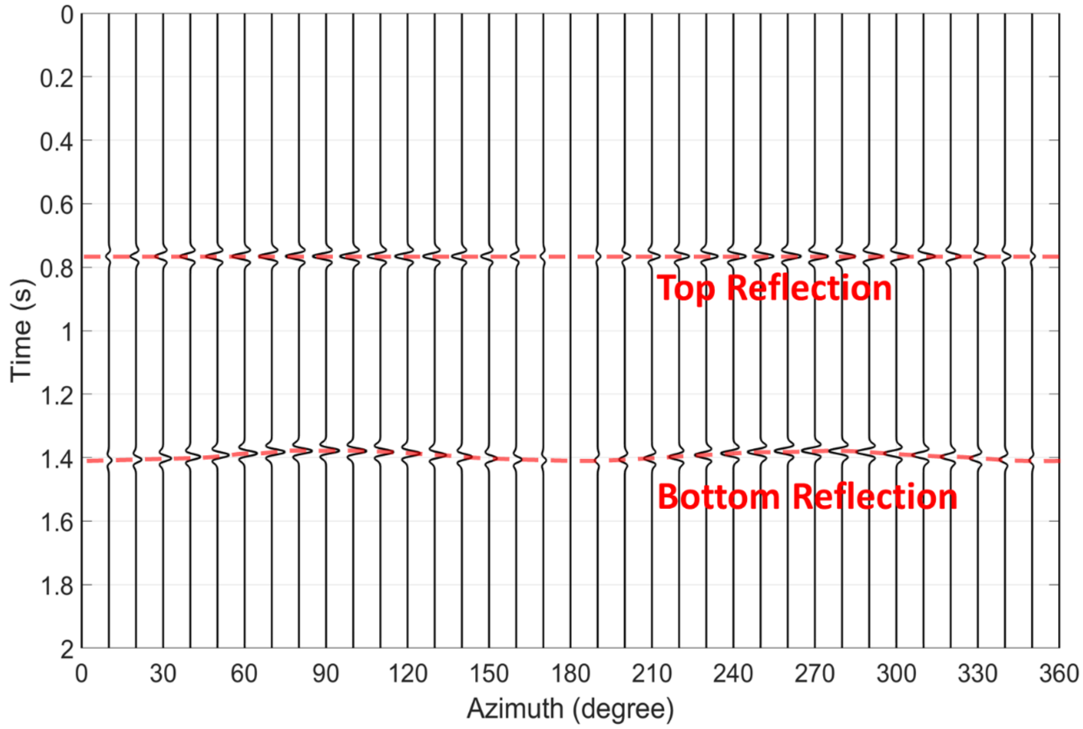

Figure 6 Reflections of P wave on the Y- component at different azimuths when the thickness of fractured layer is 1000 m. The two background red stripes in each panel indicate reflections from top and bottom of the fractured layer. The source wavelet is a 20 Hz Ricker. The incidence wave is P wave. The incidence angle is 45 degrees. Fracture strike planes are along 90-degree azimuth.

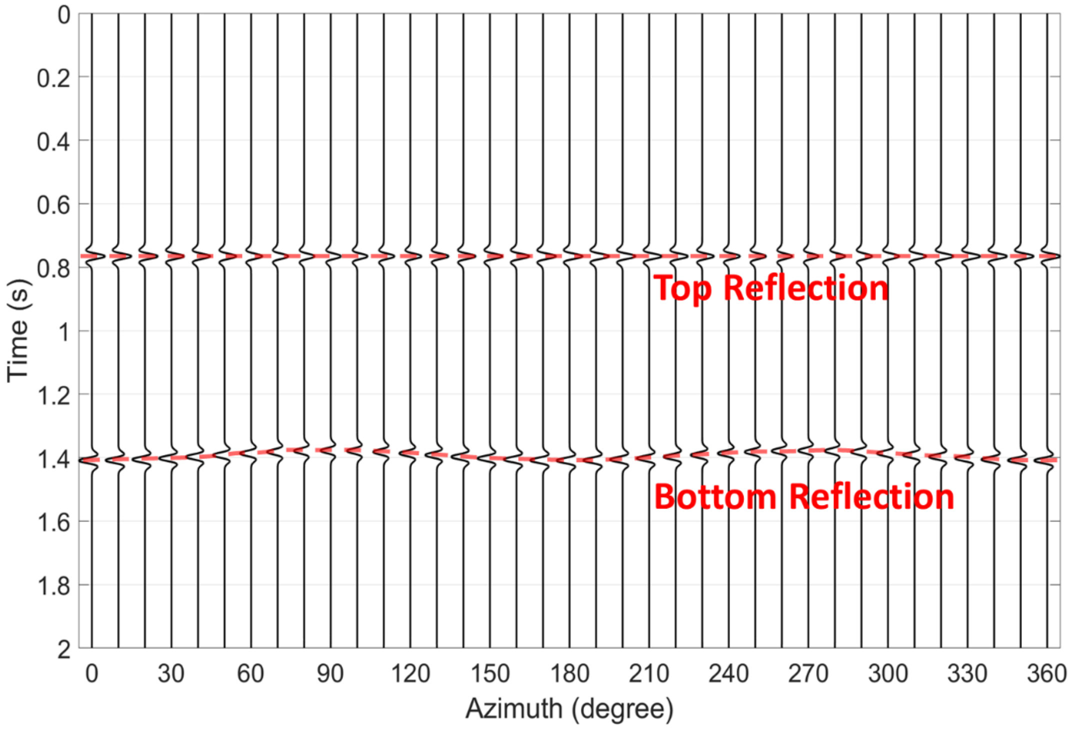

Figure 7 Reflections of P wave on the Z- component at different azimuths when the thickness of fractured layer is 1000 m. The two background red stripes in each panel indicate reflections from top and bottom of the fractured layer. The source wavelet is a 20 Hz Ricker. The incidence wave is P wave. The incidence angle is 45 degrees. Fracture strike planes are along 90-degree azimuth.

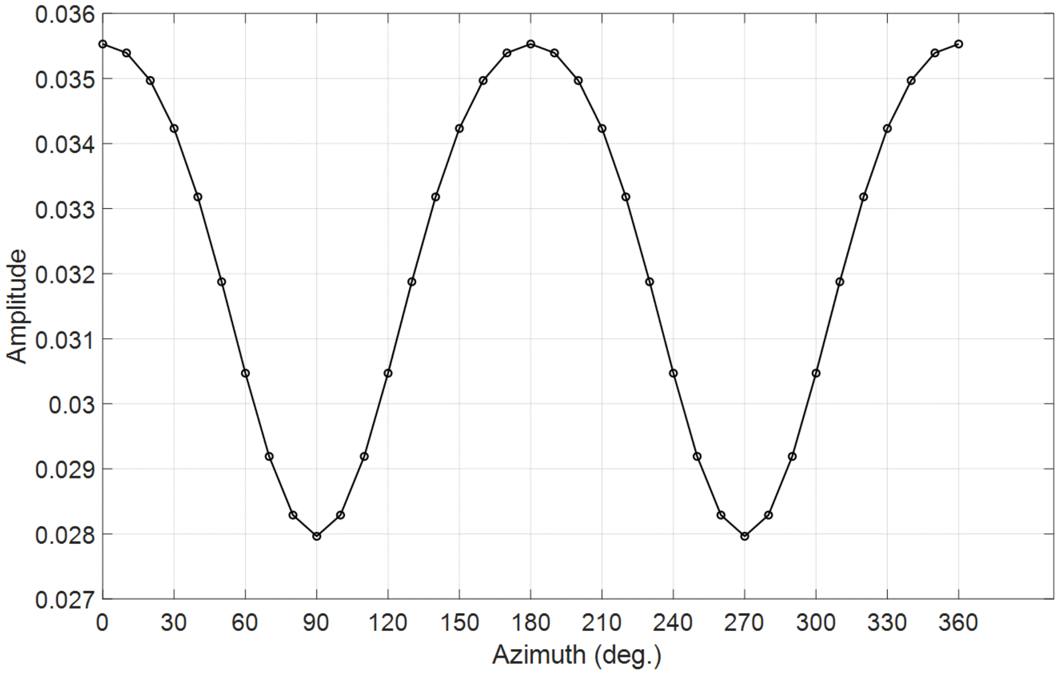

Figure 8 Amplitudes (absolute values) of top reflections that are extracted from the Z-component in *Figure 7* at different azimuths.

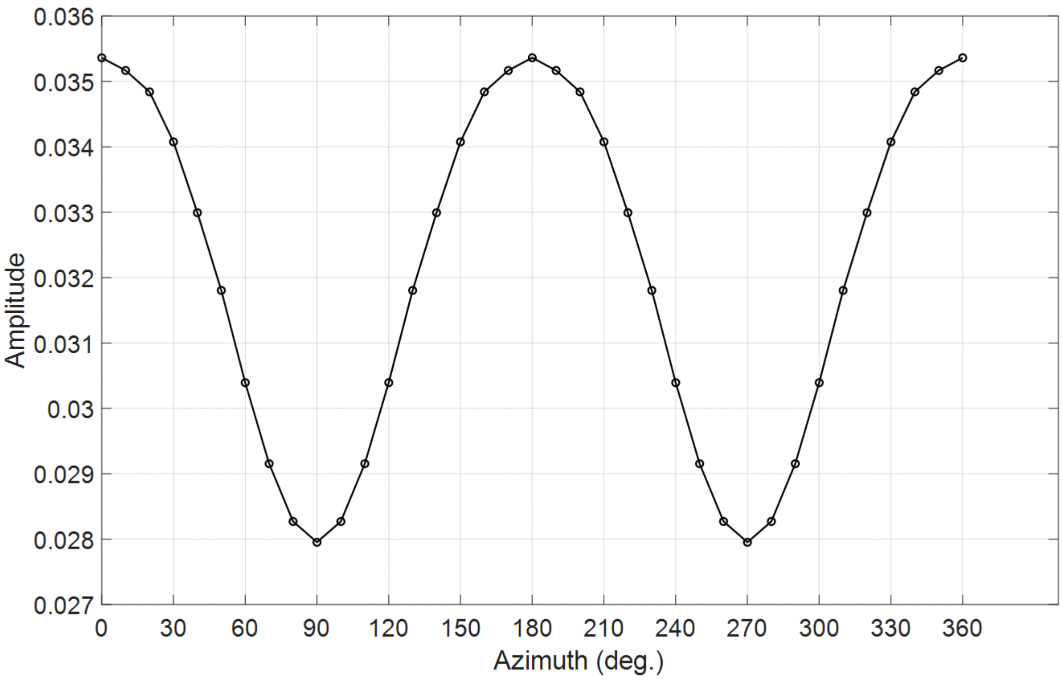

Figure 9 Amplitudes (absolute values) of bottom reflections that are extracted from the Z-component in *Figure 9* at different azimuths.

The seismograms of the three components of the reflected P waves from the top and the bottom of the fractured layer are shown in *Figure 5*, *Figure 6*, and *Figure 7*. P waves travel faster along the fracture planes (azimuth ~ 90 degrees) than perpendicular to the fractures.

From *Figure 5*, *Figure 6*, and *Figure 7*, reflections from the top of the fractured layer arrive first. They arrive at the same time regardless of azimuths because layer 1 is isotropic. Although no time residual is observed for top reflections, we still observe the sinusoidal variation of amplitudes from top reflections of P waves caused by different azimuths (top reflections in *Figure 5*, *Figure 6*, and *Figure 7*).

The reflections from the bottom of the fracture layer waves arrive between 1.2-1.6 s (*Figure 5*, *Figure 6*, and *Figure 7*). We can see the sinusoidal variation ($\cos[2\phi]$) of traveltimes (red dashed lines in in *Figure 5*, *Figure 6*, and *Figure 7*) as a function of azimuth φ for all three components. When the azimuth is parallel to the fracture strike (90 or 270 degrees), the traveltime is shorter compared to the traveltime of the azimuths perpendicular to the fractures (i.e. 0 degrees, 180 and 360 degrees).

To better observe the variation of amplitudes of reflected P wave with different azimuths, I extracted the absolute value of amplitudes of top and bottom reflections on the Z- component in *Figure 7* and showed the results in *Figure 8* and *Figure 9*. We observe the sinusoidal variation of amplitudes with the azimuth. When the source-receiver line is parallel to the fracture strike (90 degrees azimuth), we can obtain the minimum amplitude for both top and bottom reflections.

In *Figure 10 ~ Figure 15*, I calculated the reflected P wavefields for different thicknesses of the fracture layer: 31 m (1/4 of the P-wave wavelength), 125 m (same as the P-wave wavelength), 375 m (3 times of the P-wave wavelength) and 625 m (5 times of the P-wave wavelength).

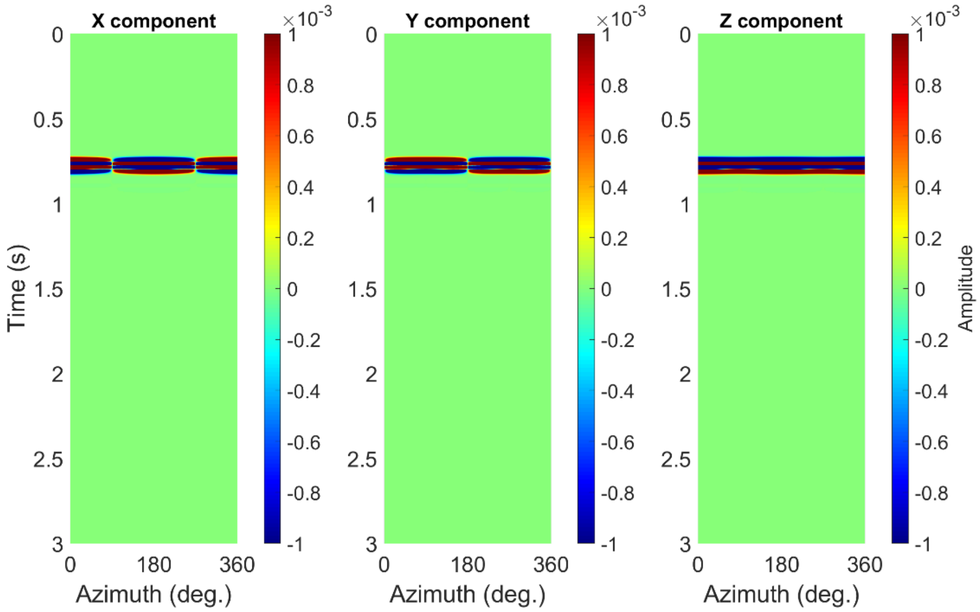

Figure 10 Reflected P wave amplitudes variation with azimuths on the X- , Y- and Z-components when the fracture layer thickness is 31 m (1/4 times of the P-wave wavelength). The source wavelet is a 20 Hz Ricker. The incidence wave is P wave. The incidence angle is 45 degrees.

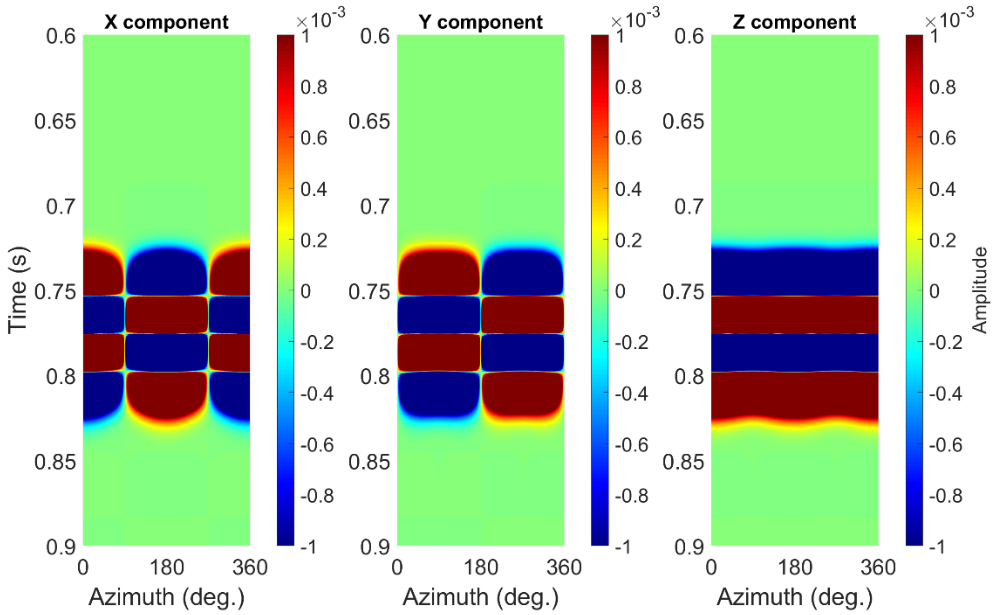

Figure 11 Reflected P wave amplitudes variation with azimuths after zooming in (*Figure 10*) on the X- , Y- and Z- components when the fracture layer thickness is 31 m (1/4 times of the P-wave wavelength). The source wavelet is a 20 Hz Ricker. The incidence wave is P wave. The incidence angle is 45 degrees.

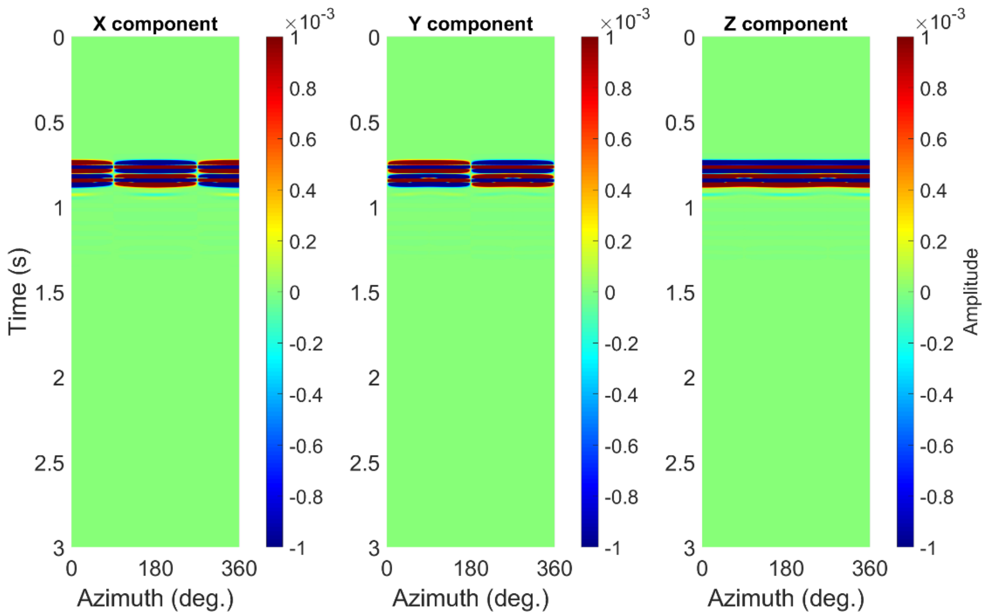

Figure 12 Reflected P wave amplitudes variation with azimuths on the X- , Y- and Z- components when the fracture layer thickness is 125 m (same as the P-wave wavelength). The source wavelet is a 20 Hz Ricker. The incidence wave is P wave. The incidence angle is 45 degrees.

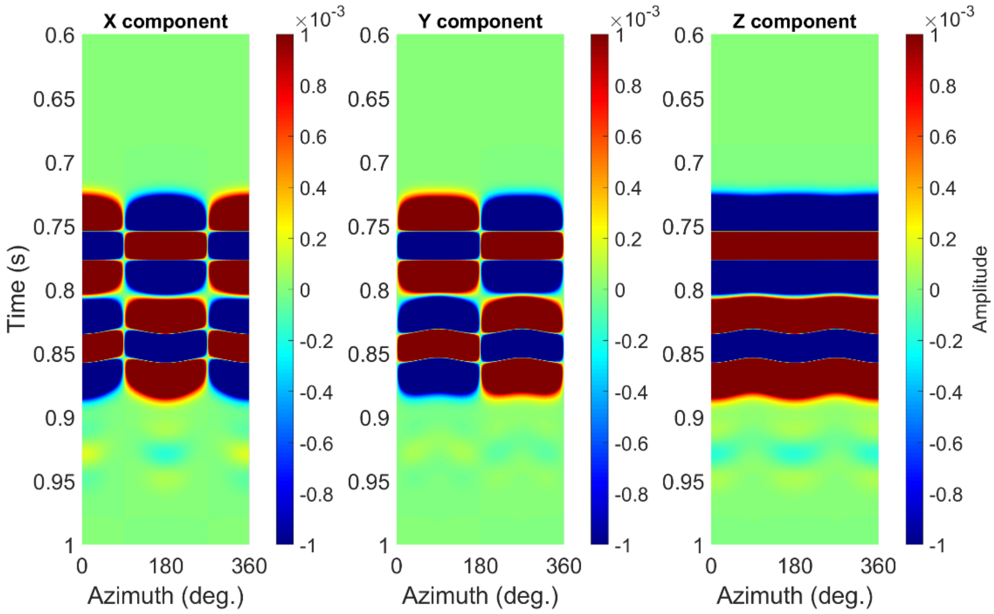

Figure 13 Reflected *P* wave amplitudes variation with azimuths after zooming in (*Figure 12*) on the X- , Y- and Z- components when the fracture layer thickness is 125 m (same as the *P*-wave wavelength). The source wavelet is a 20 Hz Ricker. The incidence wave is *P* wave. The incidence angle is 45 degrees.

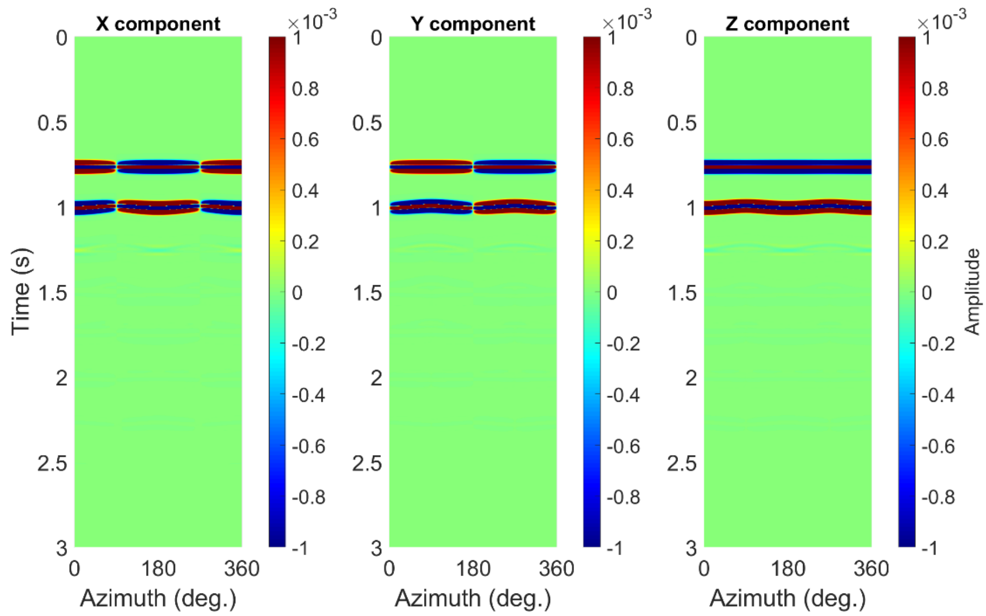

Figure 14 Reflected *P* wave amplitudes variation with azimuths on the X- , Y- and Z- components when the fracture layer thickness is 375 m (3 times of the *P*-wave wavelength). The source wavelet is a 20 Hz Ricker. The incidence wave is *P* wave. The incidence angle is 45 degrees.

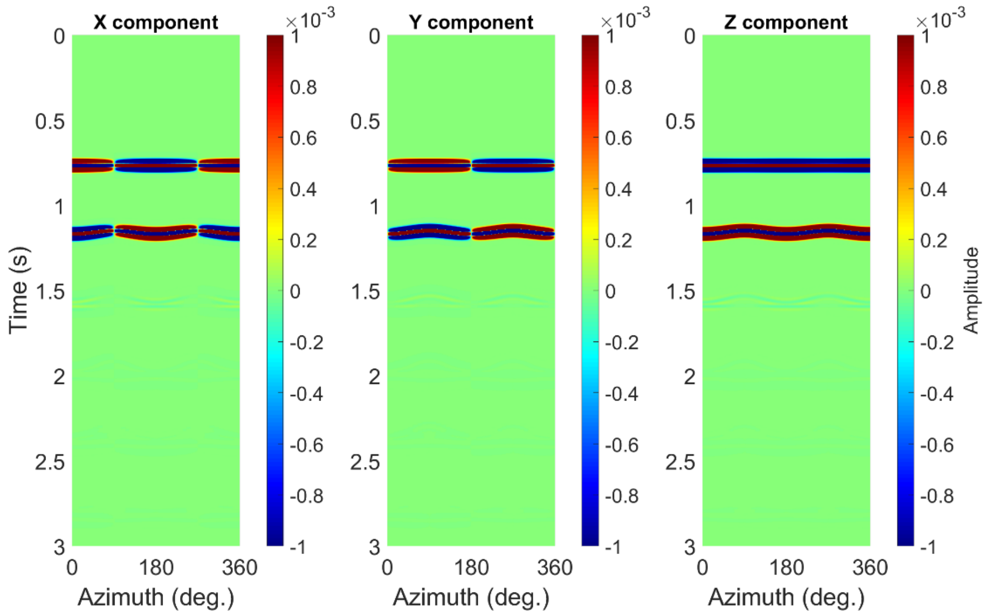

Figure 15 Reflected *P* wave amplitudes variation with azimuths on the X- , Y- and Z-components when the fracture layer thickness is 625 m (5 times of the *P*-wave wavelength). The source wavelet is a 20 Hz Ricker. The incidence wave is *P* wave. The incidence angle is 45 degrees.

From *Figure 10* to *Figure 15*, the wavefronts that arrive earlier are the reflections from the top of the fractured layer. The traveltimes are the same for all azimuths. The bottom reflections arrive between 1-1.5 s. We can easily observe the sinusoidal variation of traveltimes caused by different azimuths on all three components (*Figure 10~Figure 15*). We also observe polarity reversals at 90 degrees and 270 degrees on the X- component, and at 180 degrees on the Y- component for different fractured layer thickness.

I conclude that from the azimuthal analysis of *P*-wave traveltime and amplitude, we can extract fracture orientation. We also note that from the results in *Figure 11* to *Figure 13*, when the thickness of fractured layer is less than the *P*-wave wavelength, the reflections from the top and bottom of the fractured layer begin to overlap in time with each other. Therefore, the variation of the traveltime caused by different azimuths could not be extracted reliably from the seismic data. In order to accurately analyze the traveltime and amplitude that are extracted from azimuthal P wave data, the thickness of fractured layer has to be no less than the P-wave wavelength.

4.1.2 VTI case

In this part, I calculate the reflection coefficients of the P wave propagating through the VTI medium caused by different azimuths for my three-layer model. In order to find out how the reflection coefficients change with the azimuth in the VTI medium, I randomly picked two circular frequencies (15 and 313 Hz) to display the results below.

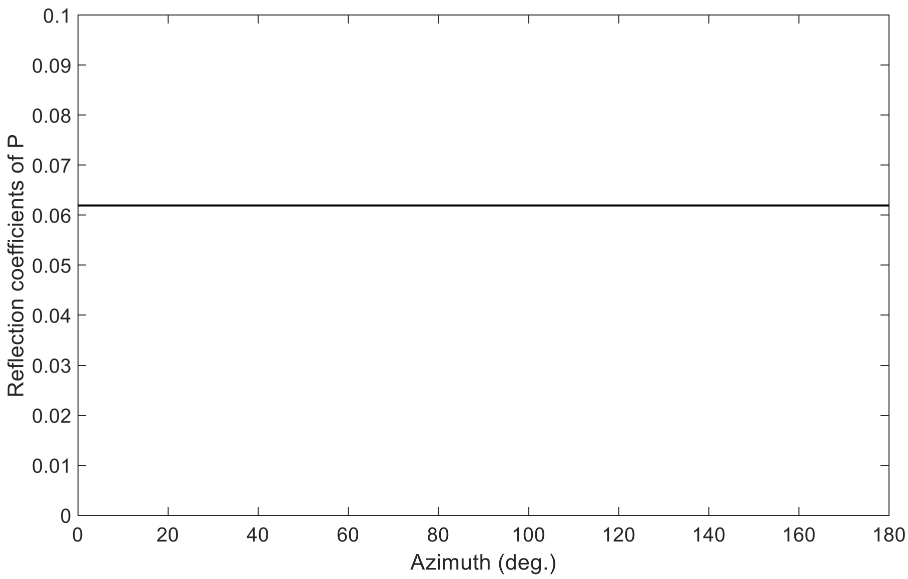

Figure 16 Reflection coefficients of P wave as a function of azimuth when frequency is 15 Hz for VTI medium.

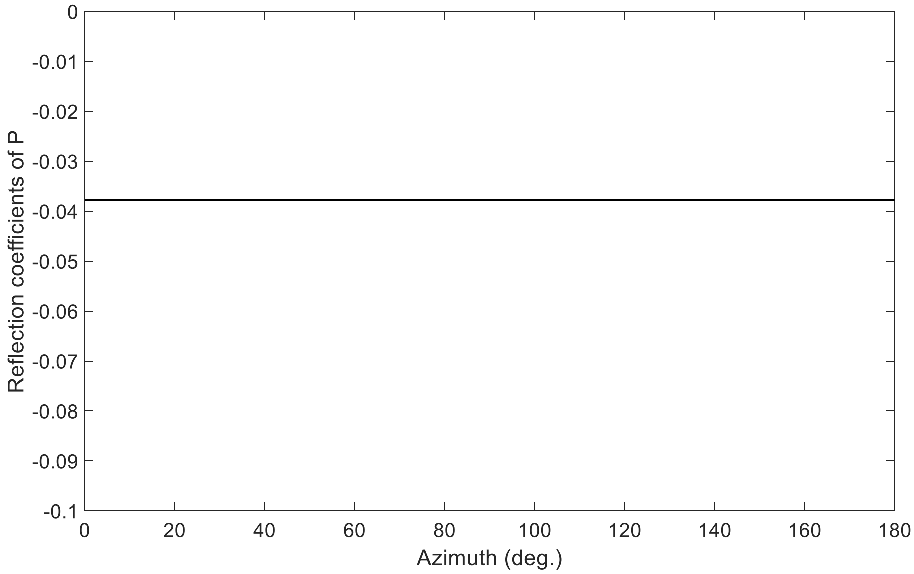

Figure 17 Reflection coefficients of *P* wave as a function of azimuth when frequency is 313 Hz for VTI medium.

According to *Figure 16* and *Figure 17*, the reflection coefficients of *P* wave do not vary with azimuth in VTI medium. The source and receivers are in XOY plane, which is the isotropy plane. The *P* wave travels at the same velocity at all azimuths. Thus, there is no variation in the amplitude of the *P* reflection with azimuth for VTI medium based on my acquisition geometry (*Figure 3*). Therefore, we are not able to extract any useful fracture information using azimuthal P wave data if the fracture model is VTI.

4.2 Conclusions

In this chapter, I first calculated the reflected *P* wavefield for HTI media as a function of azimuth using different fracture layer thickness. The results revealed that both the amplitude and the traveltime of P-wave bottom reflections of the fracture layer exhibit sinusoidal variation with source to receiver azimuth. For top reflections, we could only extract the amplitude to infer the fracture orientation.

My modeling results also presented the effect of fracture layer thickness on the azimuthal P wavefield. The thickness of the fractured layer varies from 1/4 of the P-wave wavelength, the same as the P-wave wavelength, 3 times of the P-wave wavelength to 5 times of the P-wave wavelength. When the thickness of the fracture layer is less than the P-wave wavelength, the variation of traveltimes due to different azimuths could not be extracted reliably from the seismic data.

For VTI media, no azimuthal variation of amplitude could be observed in my modeling if the acquisition geometry is the same as my model.

Chapter 5

Effect of Fracture Layer Thickness on Splitting Time of Reflected S Wavefield

There are two shear waves, which are characterized by having different polarizations and propagation velocities.

When shear waves propagating in isotropic media, the two waves are called SV and SH waves. The SV wave is polarized in the plane of the propagation of the body wave, while the SH wave is polarized orthogonal to it. In isotropic media, two shear waves both travel at the same speed.

In anisotropic media, one shear-wave can split into a fast S wave S_1 and a slow S wave S_2. Shear-wave splitting, or birefringence is a fundamental outcome of wave propagation in anisotropic media. If such splitting is present in the reservoir, it is often indicative of fracturing which can be associated with increased permeability. Shear wave splitting can be a powerful method for characterizing both anisotropy orientation (from the polarization of the fast shear wave S_1) and intensity (from S_1-S_2 time delay). These are important in understanding fluid pathways in fractured reservoirs (Bale *et al.*, 2009). In this section, I will investigate the relationship between the splitting time and the thickness of fractured layer for both HTI and VTI cases. The ability to observe shear wave splitting is defined as follows: if the time difference is larger than the sampling time interval of the seismic record, we consider the splitting observable. The acquisition geometry is the same as that shown in **Chapter 4** (*Figure 3*).

5.1 HTI case

In an HTI model, I consider an incident S wave. I calculated the splitting time of the reflected S waves caused by both SV incidence and SH incidence. In the isotropic first layer of my model, the SV wave is polarized in the plane of the direction of wave propagation and SH wave is polarized orthogonal to the SV wave. For my model, the second layer is an HTI medium. The fast S wave S_1 is polarized in the plane parallel to the fracture system, while the slow S wave S_2 is polarized in the plane perpendicular to the fracture system.

Here is an example of shear wave splitting as observed in 3D multi-component surveys shown in *Figure 18*a. When the shear wave encounters the anisotropic medium, it splits (*Figure 18*) into fast (red) and slow (blue) waves. The green axis shown parallel to the fractures in *Figure 18b*, is the 'isotropy plane' and the orange axis is the 'symmetry-axis plane'. As we can see, there is no splitting along either axis.

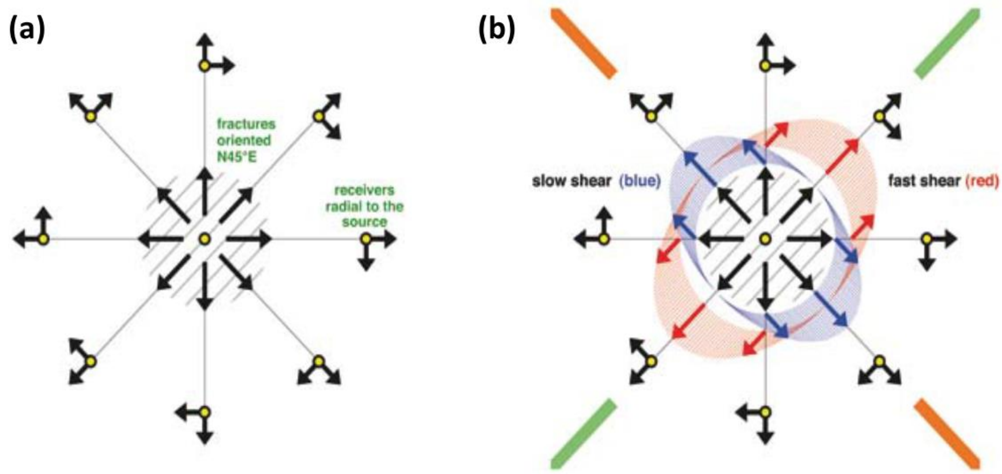

Figure 18 Illustration of 3D 'signature' of shear wave splitting. In (a), a representative geometry is shown with the effective source at the central the conversion point (CCP) location, and radial-transverse data measured at eight receiver locations. In (b), the fast and slow amplitude variation is shown in red and blue respectively, relative to the isotropy (green) and symmetry-axis (orange) planes. Note that the signal amplitude of both the fast and slow shear waves varies with the angle from the symmetry planes. At any intermediate azimuth, that SV wave is split into two components. From Bale *et al.* (2009).

5.1.1 Shear wave splitting from SV incidence

In my modeling, the synthetic seismograms are recorded in the XYZ coordinate system. However, the fast S wave S_1 and the slow S wave S_2 are simultaneously recorded in all 3 components. As a result, in order to observe shear wave splitting, we need to rotate the seismic records (Silver and Chan, 1991; Long and Silver, 2009). I rotate the multicomponent reflected wavefield of S wave until the fast S wave S_1 and slow S wave S_2 are completely separated.

First, I model the full wavefield and display the X- and Y-components of the reflected S waves caused by an incident SV wave from above in the isotropic layer 1. The P wave velocity of the background medium is 4000 m/s, while the S wave velocity is 2000 m/s. The thickness of fracture layer is 2000 m. The incidence angle is 10 degrees. The source wavelet is a Ricker wavelet with a 20 Hz central frequency. I set an anisotropy value of ~14% with the fast symmetry axis along the y-axis for the S wave. The synthetic seismogram of S reflections at the 30-degree azimuth are shown in *Figure 19*. The fast S wave and the slow S wave are not separated (*Figure 19*) when we record the seismogram in layer 1. We need to apply rotation correction to separate the fast and slow S wave on seismic records. I extract the X- component of the reflected S wavefield u_x and the Y- component u_{y} in *Figure 19*, and project them onto the direction of u_β with the rotation angle β (*Figure 20*). This way, I have the projected wavefield u_x' from u_x and u_{y}' from u_{y}. Combing u_x' and u_{y}', I obtain the rotated wavefield u_β (*Figure 20*). Rotating u_β from 0 to 360 degrees, the reflected S wavefield separates into the fast S wave S_1 and the slow S wave S_2 (*Figure 21*).

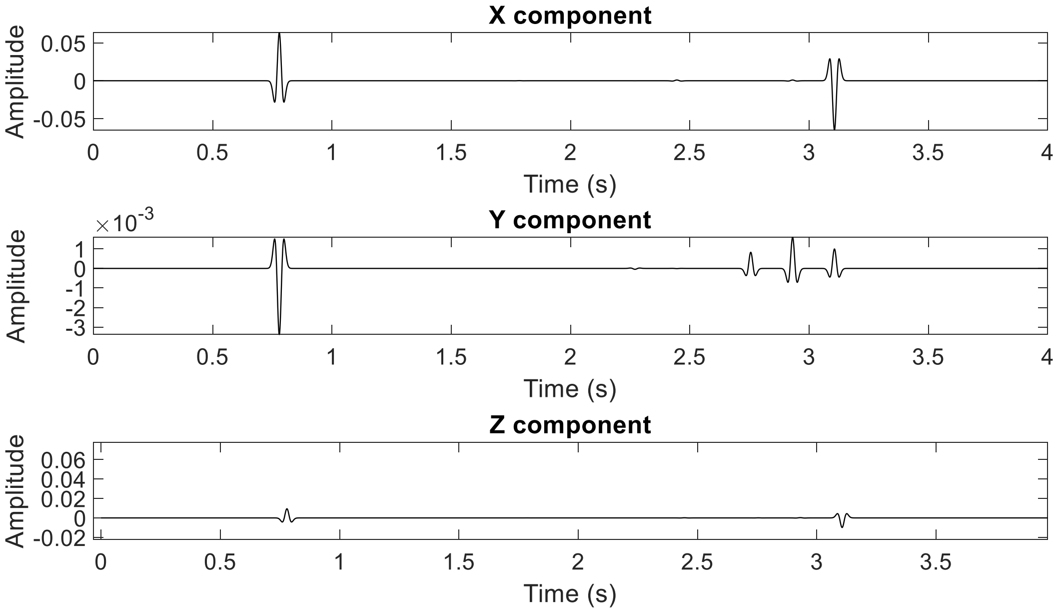

Figure 19 The synthetic seismogram of reflected S wavefield recorded on three components at the 30-degree azimuth. The thickness of fracture layer is 2000 m. The incidence angle is 10 degrees. The source wavelet is Ricker of a central frequency 20 Hz.

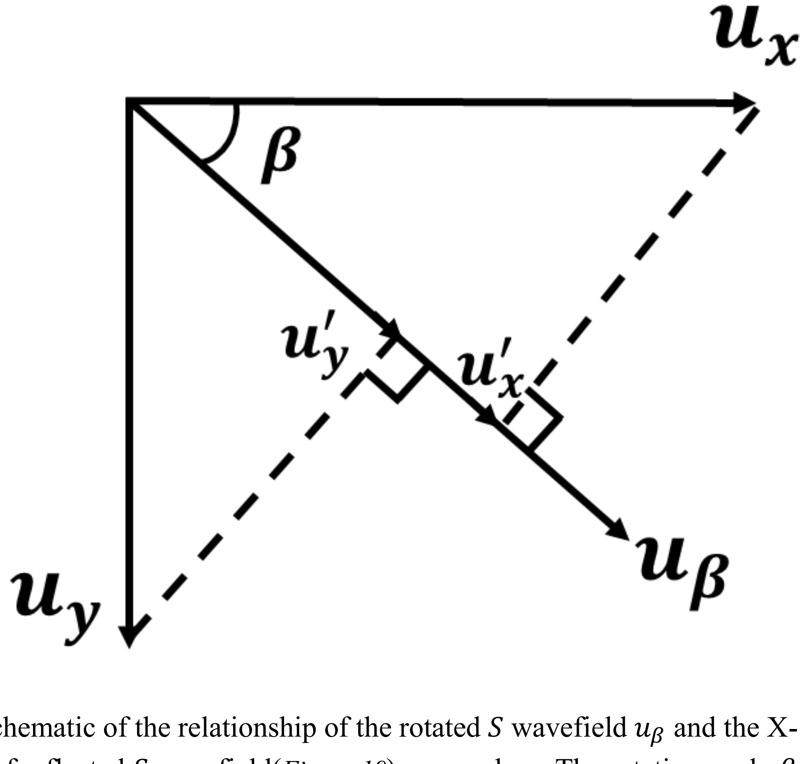

Figure 20 Schematic of the relationship of the rotated S wavefield u_β and the X- and Y-component of reflected S wavefield(*Figure 19*) - u_x and u_y. The rotation angle β is the angle between u_x and u_β. u'_x is the projection of u_x and u'_y is the projection of u_y.

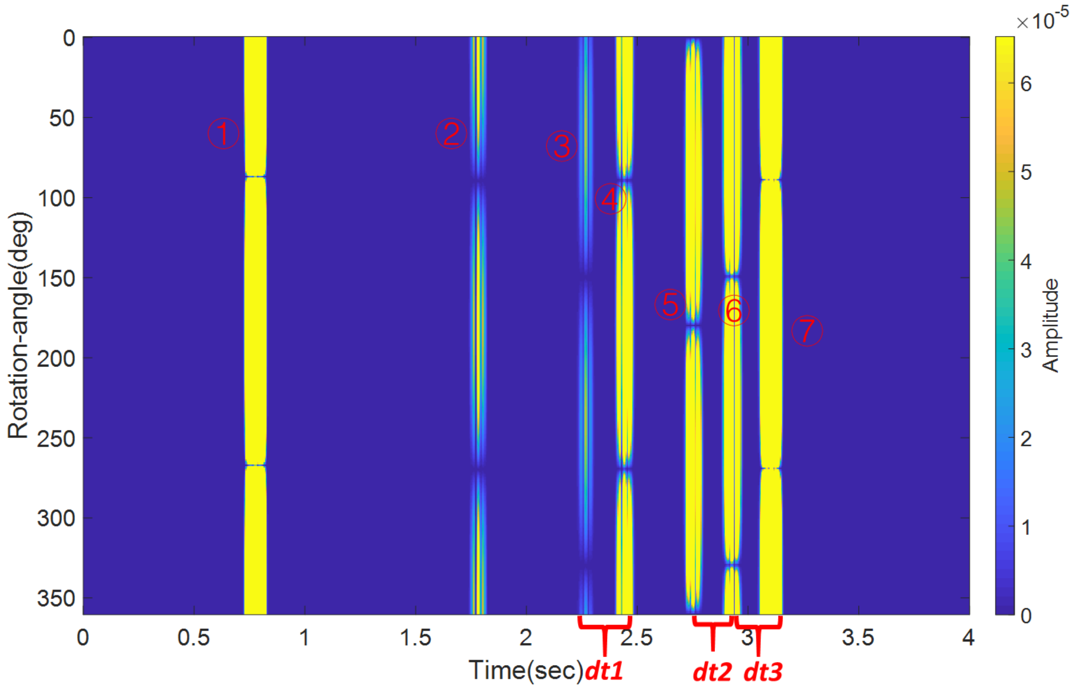

Figure 21 Reflections of S wave at 30-degree azimuth after rotation. The thickness of fracture layer is 2000 m. The incident angle is 10 degrees. The source wavelet is Ricker of a central frequency 20 Hz. Seismic events 1~7 are: S-S, S-P-P-S, S-P-S_1-S, S-P-S_2-S, S-S_1-S_1-S, S-S_1-S_2-S and S-S_2-S_2-S.

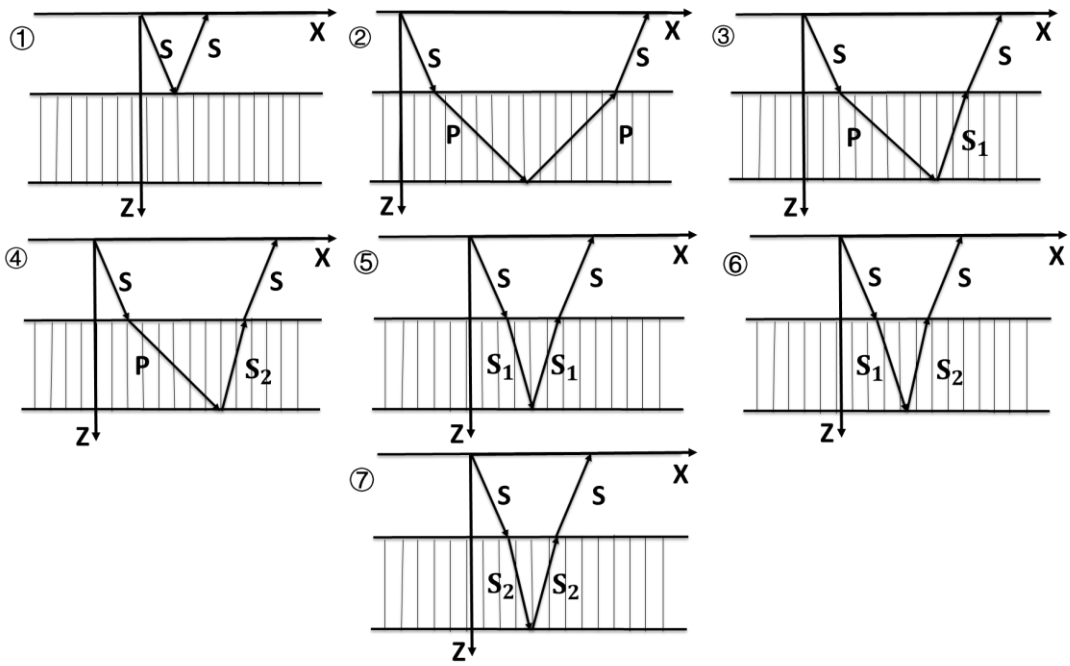

Figure 22 Schematic of ray paths of seismic event 1~6 when the azimuth is 30 degrees.

When the azimuth is 30 degrees, splitting could be observed after rotation. I applied raytracing to my model, I figured out every seismic event displayed in Figure *21* from number 1 to 7 in 4s recording time period. They are S-S, S-P-P-S, S-P-S_1-S, S-P-S_2-S, S-S_1-S_1-S, S-S_1-S_2-S and S-S_2-S_2-S successively (*Figure 21*: seismic event 1~7). dt_1 denotes the time delay between S-P-S_1-S and S-P-S_2-S; *dt2* denotes the time delay between S-S_1-S_1-S and S-S_1-S_2-S; *dt3* denotes the time delay between S-S_1-S_2-S and S-S_2-S_2-S.

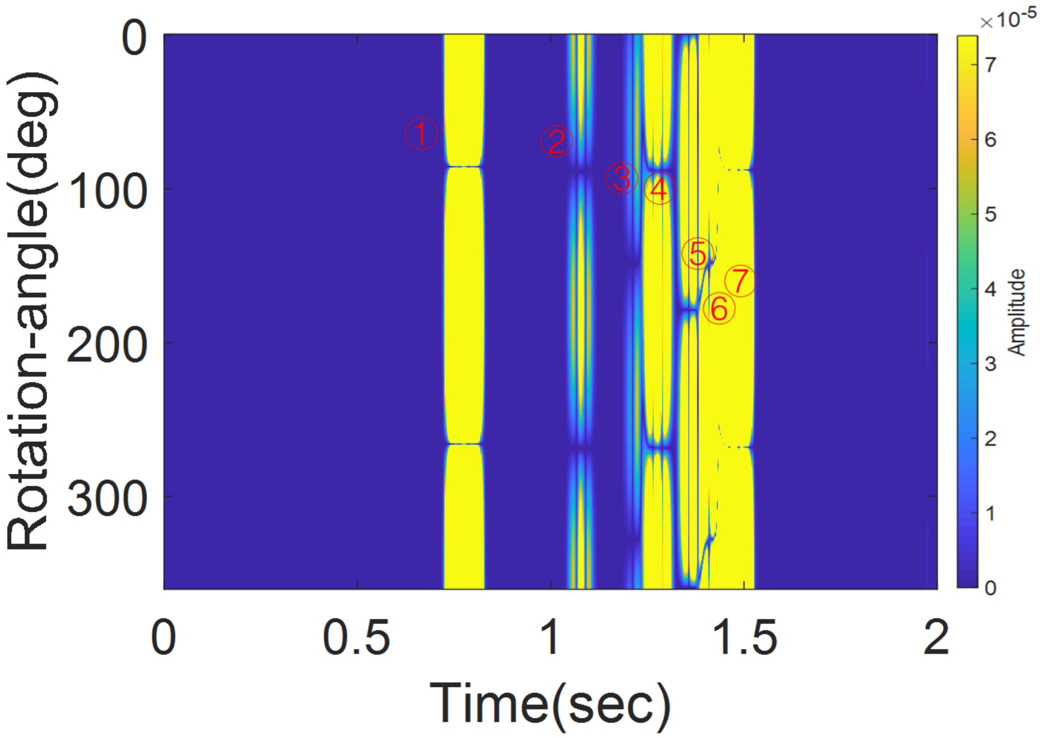

Figure 23 Reflections of S wave at the 30-degree azimuth after rotation when the thickness of fractured layer is 6 times of S wavelength (600 m). Seismic event 3 and 4 (S-P-S_1-S and S-P-S_2-S), 5-7 (S-S_1-S_1-S, S-S_1-S_2-S and S-S_2-S_2-S) all overlap with each other.

To further investigate how the thickness of the fractured layer will affect the transmitted shear wavefield. I calculated the splitting time *dt1*, *dt2*, and *dt3* for different thickness of fractured layer from 0.1 times of S wavelength to 15 times of S wavelength which is 1500 m with ~14% anisotropy of S wave. However, when the thickness is five times of the S wavelength (500 m), the S-P-S_1-S wave and S-P-S_2-S wave begin to overlap with each other. Therefore, I could not obtain the splitting time from the observation if the thickness is less than 500 m (five times of the S wavelength). When the thickness is six times of the S wavelength (600 m), the splitting time *dt2* and *dt3* could not be observed correctly because they overlap (*Figure 23*). The relationships between time delay *dt1*, *dt2*, and *dt3* and thickness of fractured layer are given for both azimuth is 30 degrees and 60 degrees through *Figure 24*, *Figure 25*, *Figure 26*, and *Figure 27*.

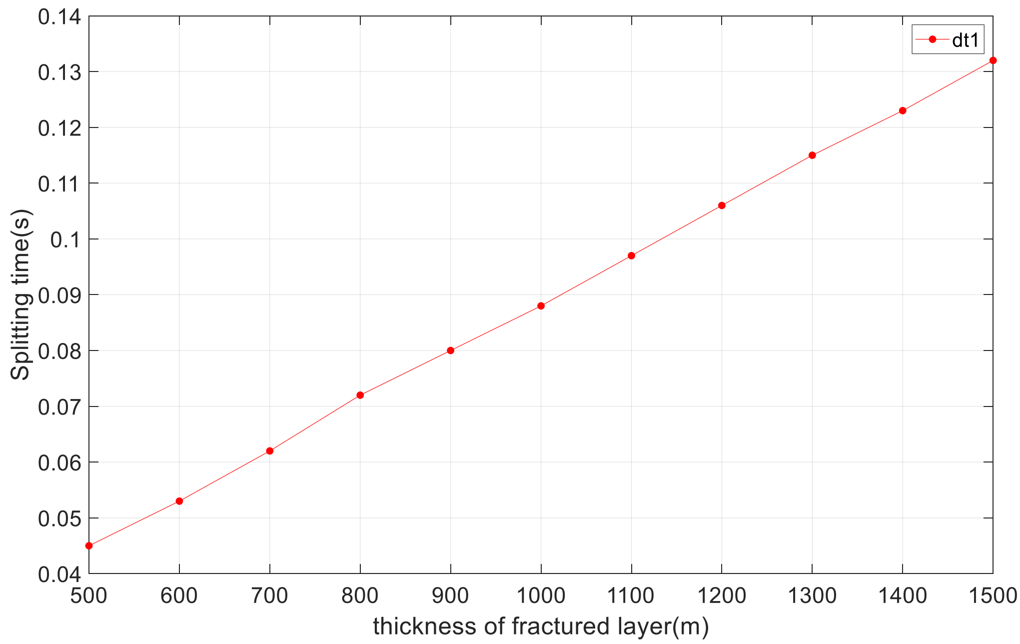

Figure 24 Time delay of S-P-S_1-S and S-P-S_2-S (*dt1*) due to different thickness of fractured layer at the 30-degree azimuth. The S wavelength is 100 m. The anisotropy is ~14% of S wave.

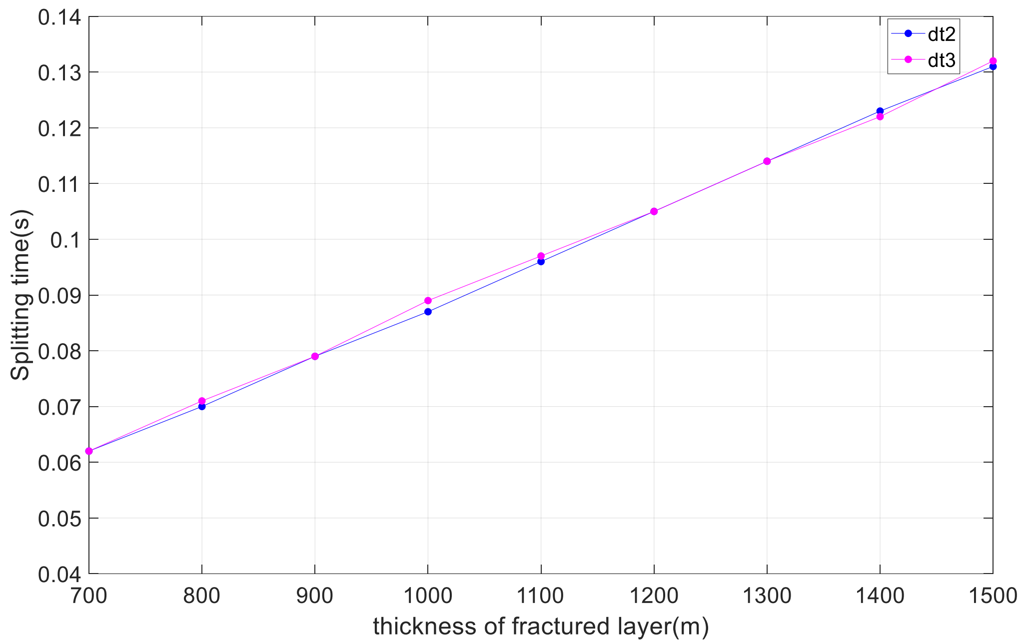

Figure 25 Time delay of S-S_1-S_1-S and S-S_1-S_2-S (*dt2*), S-S_1-S_2-S, and S-S_2-S_2-S (*dt3*) due to different thickness of fractured layer at the 30-degree azimuth. The S wavelength is 100 m. The anisotropy is ~14% of S wave.

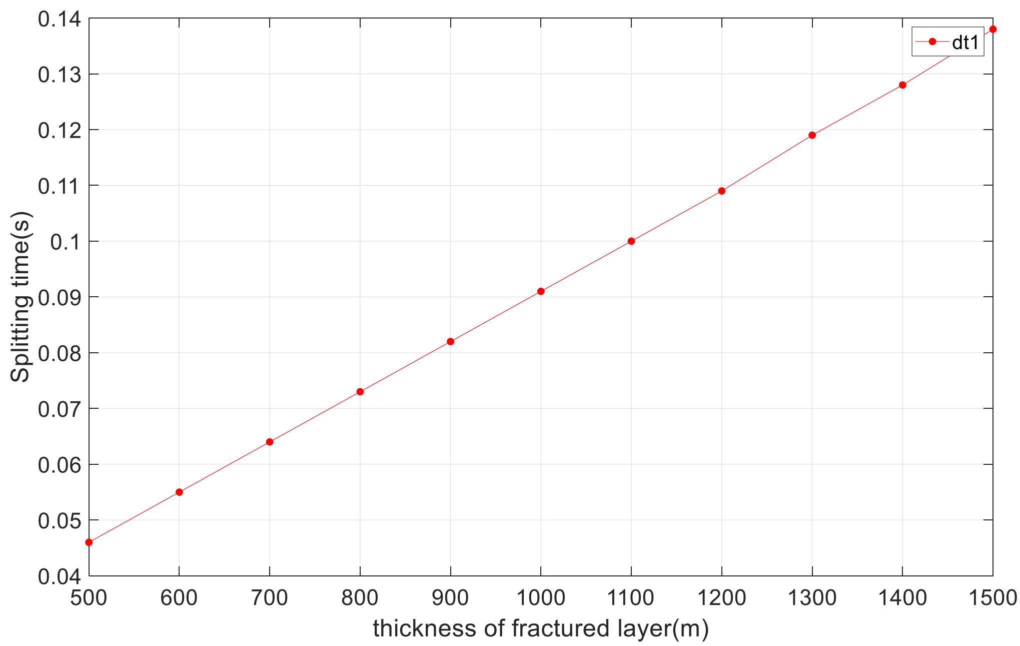

Figure 26 Time delay of S-P-S_1-S and S-P-S_2-S (*dt1*) due to different thickness of fractured layer at the 60-degree azimuth. The S wavelength is 100 m. The anisotropy is ~14% of S wave.

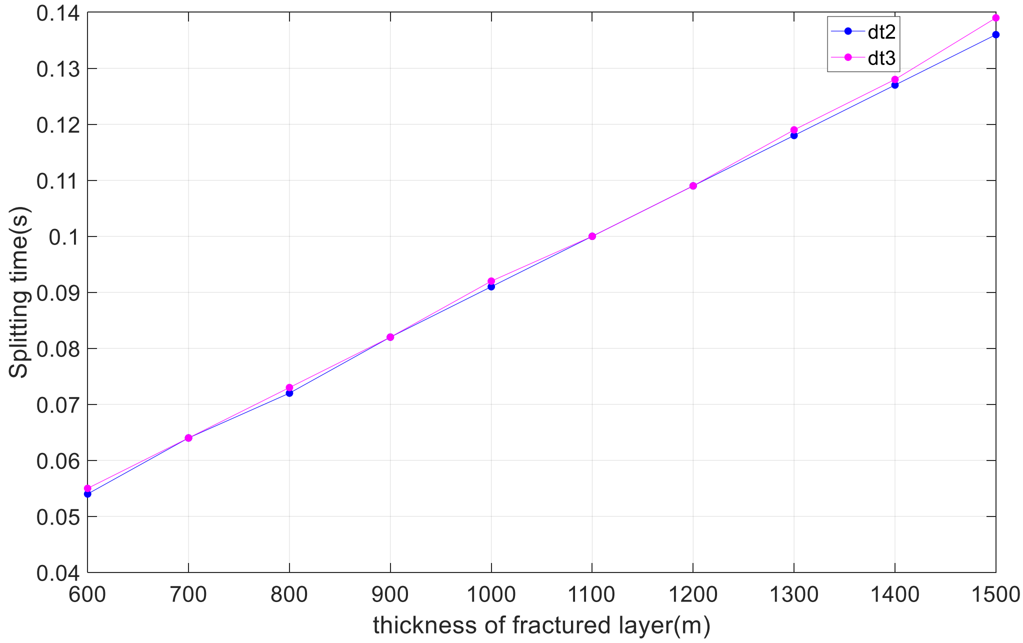

Figure 27 Time delay of S-S_1-S_1-S and S-S_1-S_2-S (*dt2*), S-S_1-S_2-S and S-S_2-S_2-S (*dt3*) due to different thickness of fractured layer at the 60-degree azimuth. The S wavelength is 100 m. The anisotropy is ~14% of S wave.

According to the results, the thickness of the fractured layer influences shear wave splitting more than the azimuths do. The splitting time for reflected shear waves increases with the increasing fractured layer thickness. If we extract the splitting time from the seismic records, we could then estimate the thickness of reservoir layer based on this modeling results. However, if the thickness is less than 500 m (five times of the S wavelength), the splitting time would be too short to be observable (shorter than the sampling time interval) from the synthetic seismogram for S-P-S_1-S and S-P-S_2-S waves (*Figure* 24 and *Figure* 26). To observe splitting, the minimum thickness of fractured layer has to be 600 m (six times of the S wavelength) for reflected S-S_1-S_1-S and S-S_1-S_2-S, and for S-S_1-S_2-S and S-S_2-S_2-S.

5.1.2 Shear wave splitting from *SH* incidence

In this part, the incidence wave in isotropic layer 1 is an SH wave which is polarized orthogonal to the direction of wave propagation. I calculated the S reflection at first and apply rotation correction in the same way as discussed in **Section 5.1.1**. Then I extracted the splitting time due to different fracture thicknesses at the 30-degree azimuth and the 60-degree azimuth. The results are displayed in *Figure 28 ~ Figure 31*. The P wave velocity in the background medium is 4000 m/s, while the S wave velocity is 2000 m/s. The thickness of fractured layer is 2000 m. The incidence angle is 10 degree. The source wavelet is a 20 Hz Ricker wavelet. The azimuth is the angle between the source to receiver line and the positive *x*-axis as defined in **Chapter 4**.

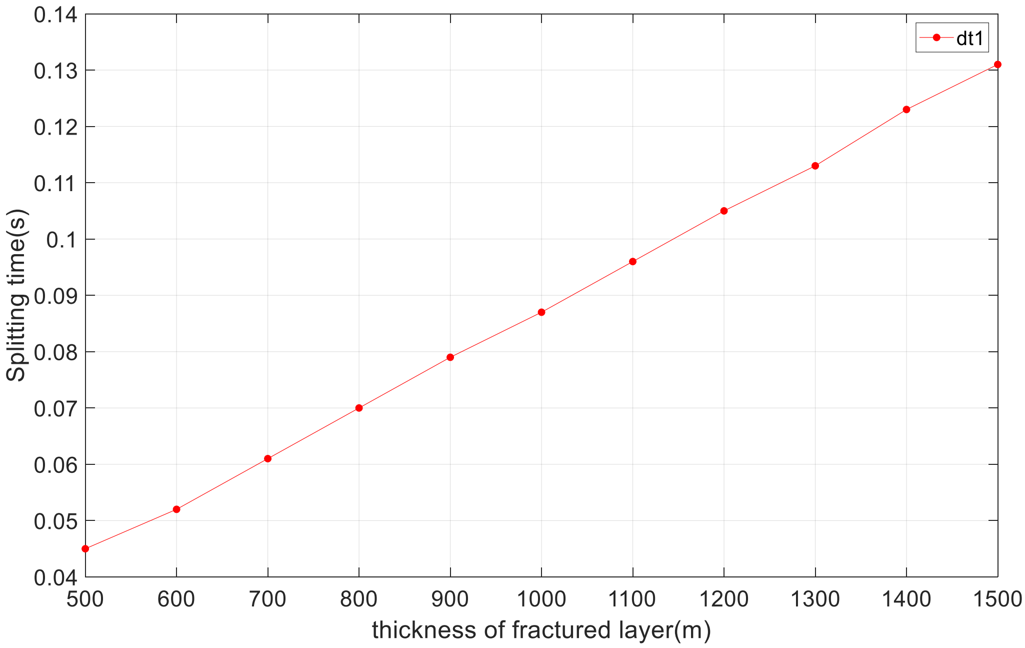

Figure 28 Time delay of S-P-S_1-S and S-P-S_2-S (*dt1*) due to different thickness of fractured layer at the 30-degree azimuth. The S wavelength is 100 m. The anisotropy is ~14% of S wave.

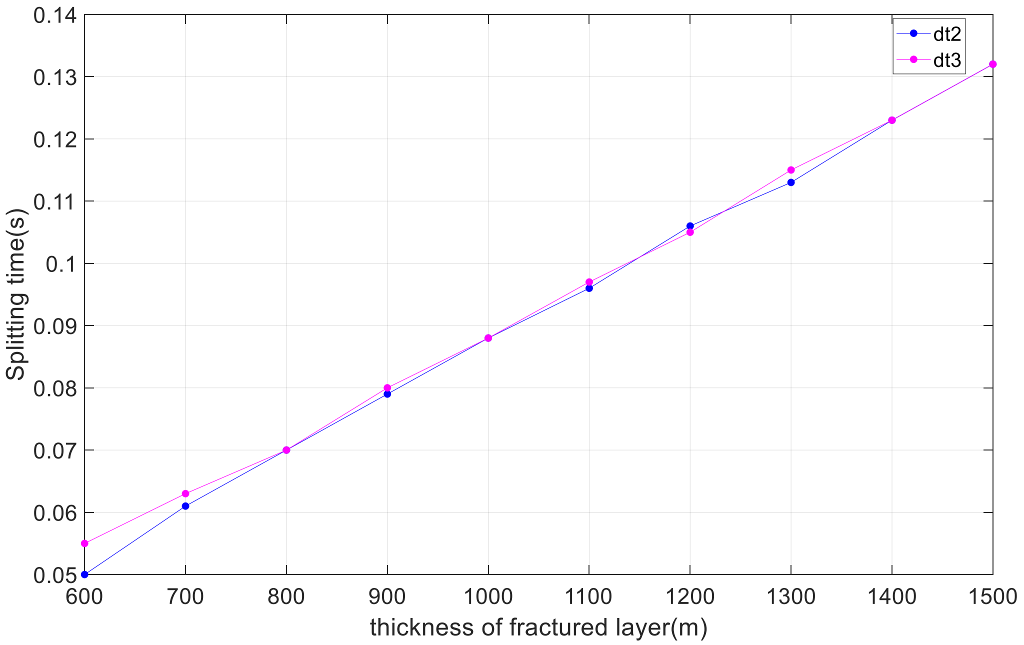

Figure 29 Time delay of S-S_1-S_1-S and S-S_1-S_2-S (*dt2*), S-S_1-S_2-S and S-S_2-S_2-S (*dt3*) due to different thickness of fractured layer at the 30-degree azimuth. The S wavelength is 100 m. The anisotropy is ~14% of S wave.

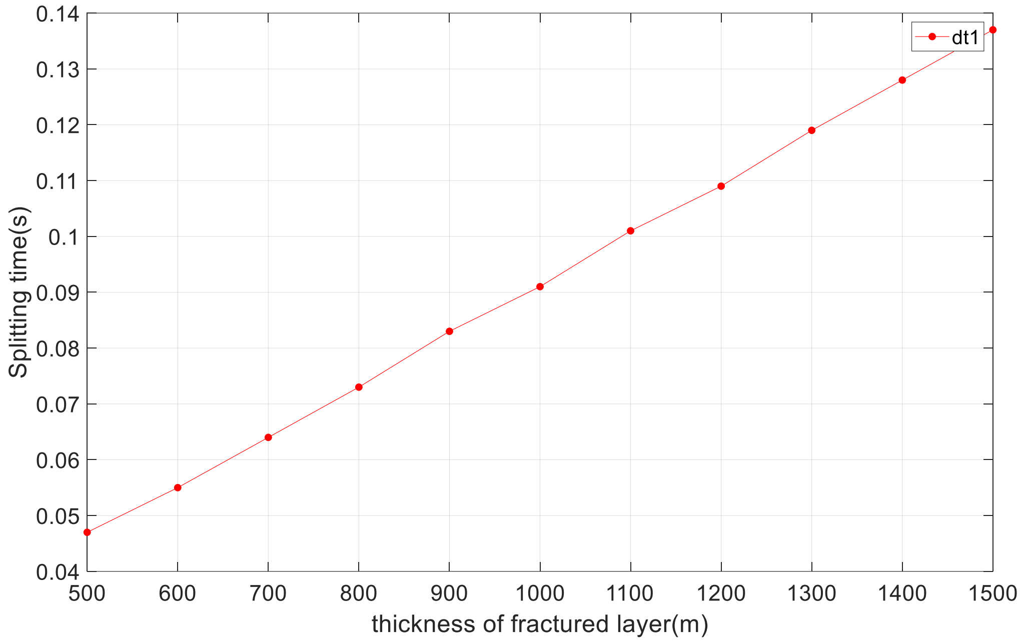

Figure 30 Time delay of S-P-S_1-S and S-P-S_2-S (*dt1*) due to different thicknesses of the fractured layer at the 60-degree azimuth. The S wavelength is 100 m. The anisotropy is ~14% of S wave.

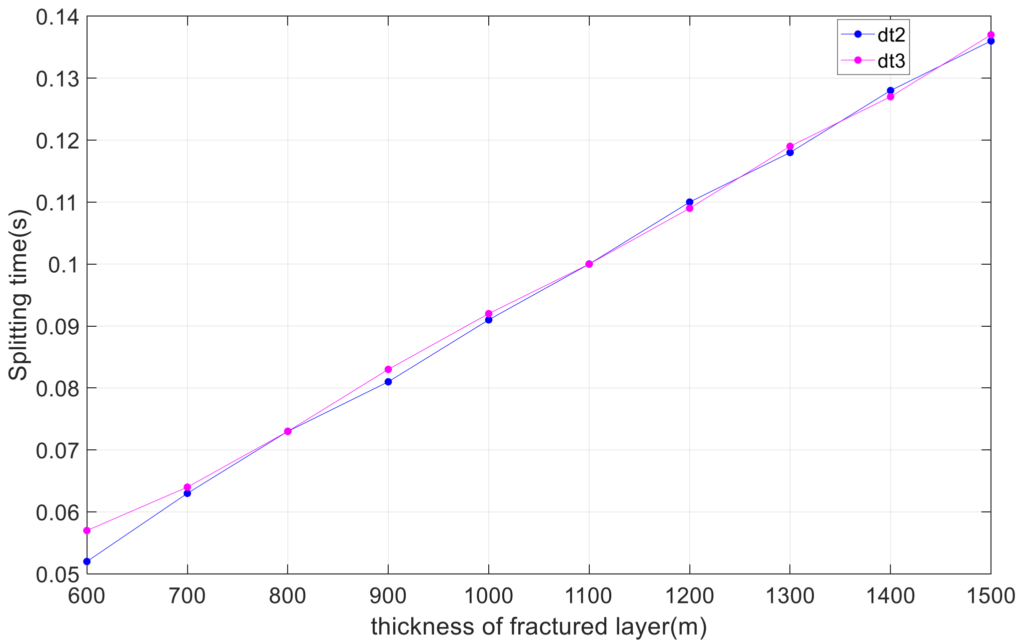

Figure 31 Time delay of S-S_1-S_1-S and S-S_1-S_2-S (*dt2*), S-S_1-S_2-S and S-S_2-S_2-S (*dt3*) due to different thickness of fractured layer at the 60-degree azimuth. The S wavelength is 100 m. The anisotropy is ~14% of S wave.

Comparing *Figure 28* with *Figure 30* and *Figure 29* with *Figure 31*, we observe that the change of azimuth does not influence splitting time. The time delay *dt1*, *dt2*, and *dt3* all increase with the increasing fractured layer thickness. In order to observe S-P-S_1-S and S-P-S_2-S splitting, the thickness of the fractured layer must not be larger than 500 m (five times of the S wave wavelength). Also, the change of *dt2* and *dt3* caused by different fractured layer thickness is almost the same. If the thickness is less than 600 m (six times of the S wavelength), then we will fail to observe splitting of S-S_1-S_1-S, S-S_1-S_2-S and S-S_2-S_2-S in seismic records.

5.2 VTI case

In this section, I use VTI medium for my fracture model. I calculated the wavefields of the reflected S waves in VTI media by changing the stiffness matrix from HTI to VTI. First, I will investigate the reflection wavefield at the 0-degree azimuth for SV incidence. The wavefronts marked in *Figure 32* are S-S, S-P-P-S, S-P-S_2-S, and S-S_2-S_2-S, successively upon on arrival time determined by raytacing. The P wave velocity in the background medium is 4000 m/s, while the S wave velocity is 2000 m/s. The thickness of fractured layer is 2000 m. The incidence angle is 10 degrees and the source wavelet is a 20 Hz Ricker wavelet.

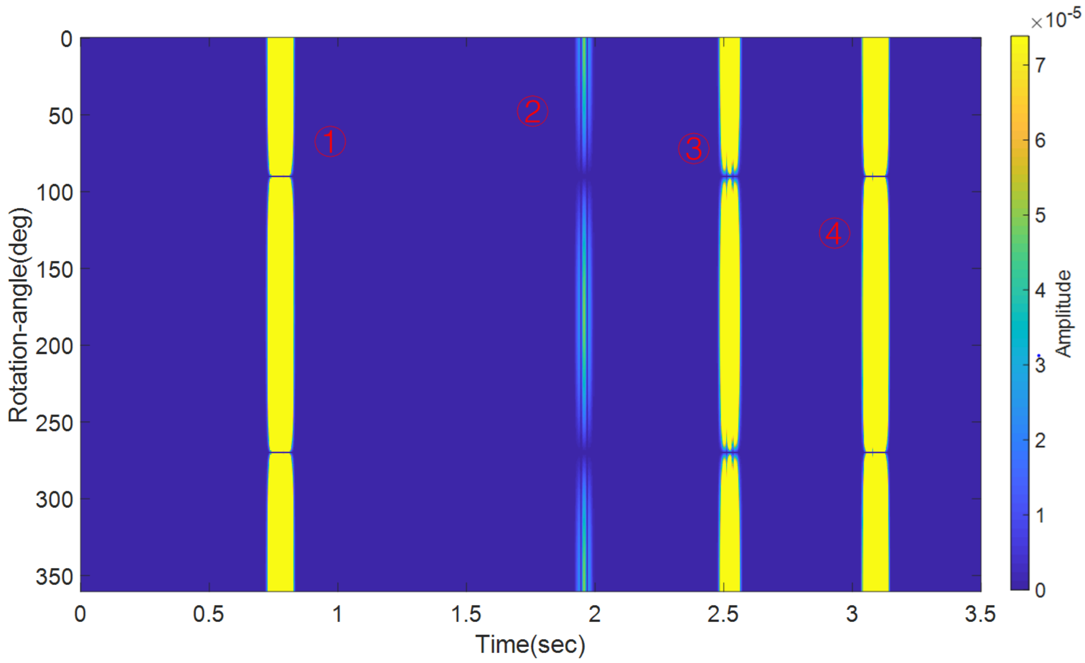

Figure 32 Reflections of S wave in layer 1 when the azimuth is 0 degrees. Seismic event 1 is the S-S reflection, event 2 is S-P-P-S, event 3 is S-P-S_2-S, and event 4 is S-S_2-S_2-S reflection.

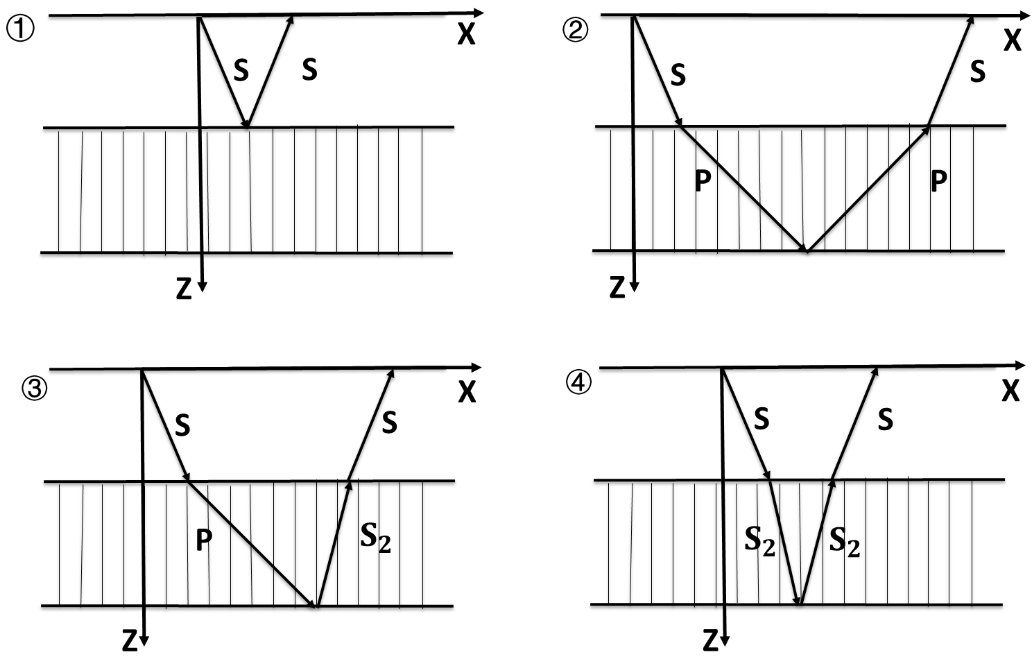

Figure 33 Schematic of ray paths of seismic event 1~4 when the azimuth is 0 degrees.

Changing the azimuth to 30 degrees, the reflection of S waves in layer 1 is shown in *Figure 34*. Applying raytracing, the four wavefronts in 0 ~ 3.5 s are S-S, S-P-P-S, S-P-S_2-S and S-S_2-S_2-S successively. We only have the slow S wave in the seismogram. In this case, no splitting is observed. However, in order to determine the reason why the splitting could not be observed is that there's actually no splitting or it's a special case of splitting in VTI medium. I need to do some further investigation.

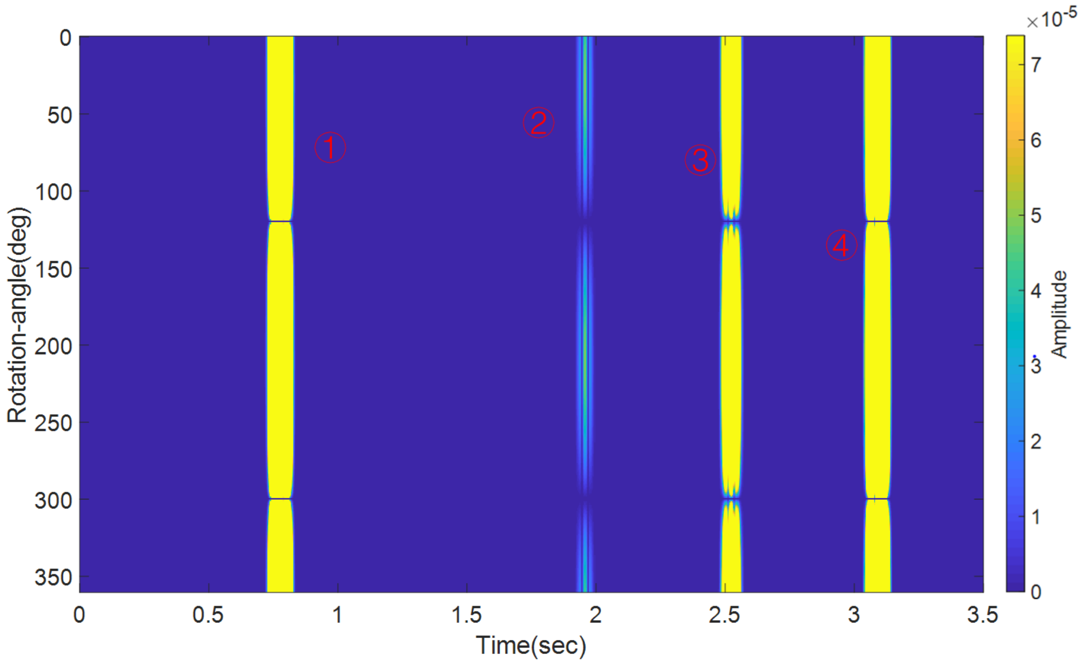

Figure 34 Reflection of S wave in layer 1 when the azimuth is 30 degrees. Seismic event 1 is the S-S reflection, event 2 is S-P-P-S, event 3 is S-P-S_2-S, and event 4 is S-S_2-S_2-S reflection.

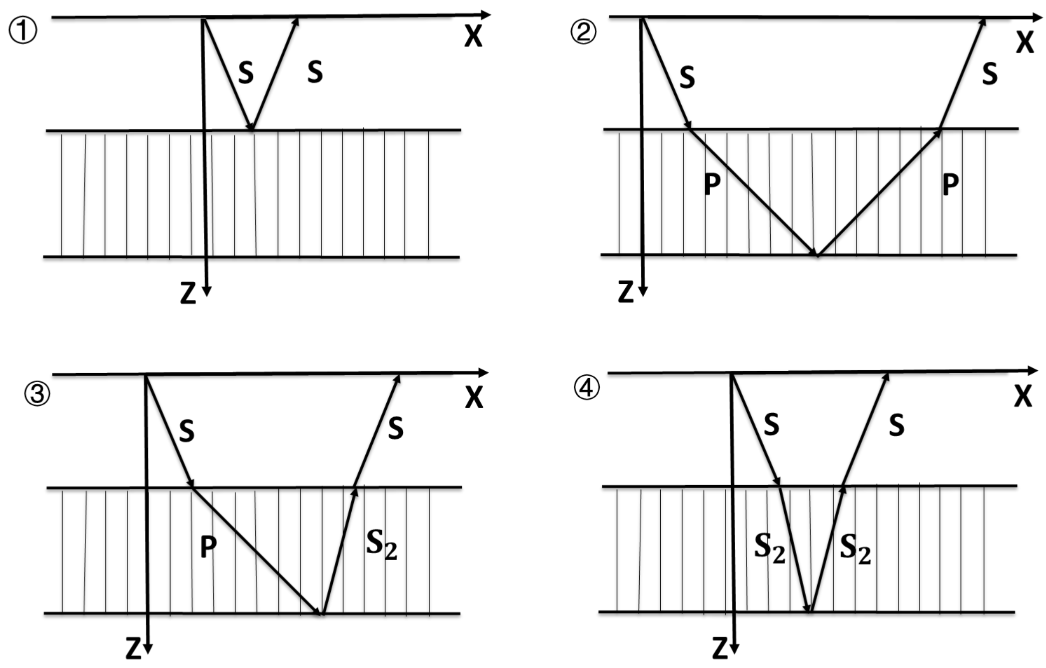

Figure 35 Schematic of ray paths of seismic event 1~4 when the azimuth is 30 degrees.

As discussed in Chapter 2, I can obtain the six values of wavenumber so as to get the velocities of P, $S_1$and S_2 waves in fractured layer 2. According to *Figure 36*, the velocities of P, $S_1$and S_2 waves do not vary with azimuths from 0 to 180 degrees. The velocity of S_1 wave (blue line in *Figure 36*) and S_2 wave (magenta line in *Figure 36*) are always different at any azimuth, which means that the shear wave actually splits into two.

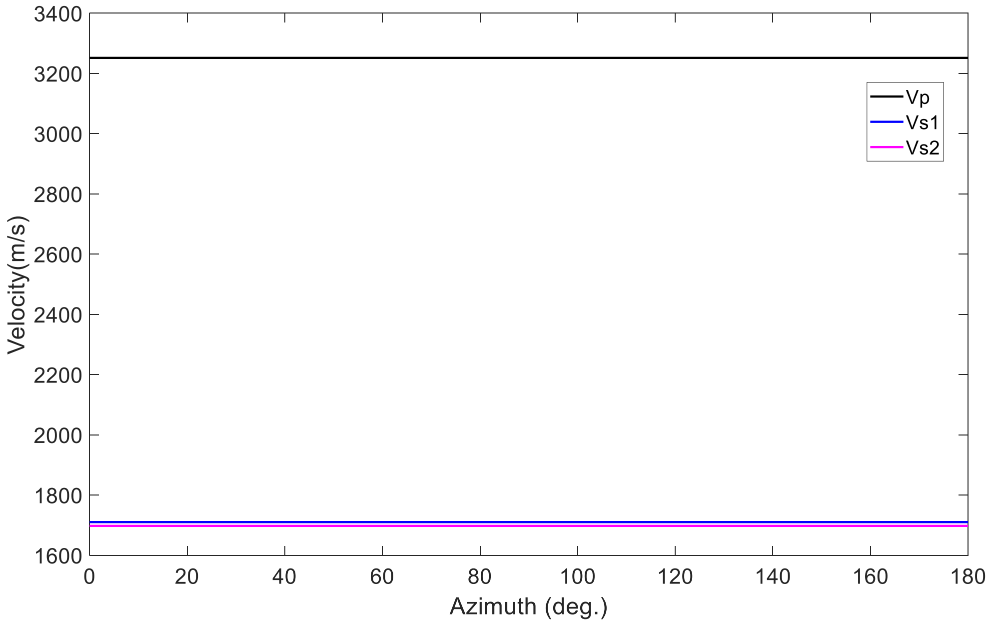

Figure 36 Velocities for downgoing P, S_1, and S_2waves in layer 2 (fractured layer).

The reflection coefficients calculated in Chapter 2 are frequency dependent. I randomly picked two cases: *t*=1 s and 3 s in time domain to see the change of reflection coefficients caused by azimuths. The reflection coefficients of P, S_1, and S_2 waves at 1 s and 3 s are shown in *Figure 37* and *Figure 38*. The value of reflection coefficients of S_1 wave (fast S wave) stay zero at any azimuth at both 1 s and 6 s. In this case, I conclude that the S wave splits into the fast S wave and the slow S wave in VTI medium. However, the reflection coefficients of the fast S wave are always zero under this kind of layered model and geometry in my modeling. As a result, only the slow S wave could be recorded. It is also the reason why the splitting could not be observed in the synthetic seismogram even with the change in azimuths (*Figure 32* and *Figure 34*).

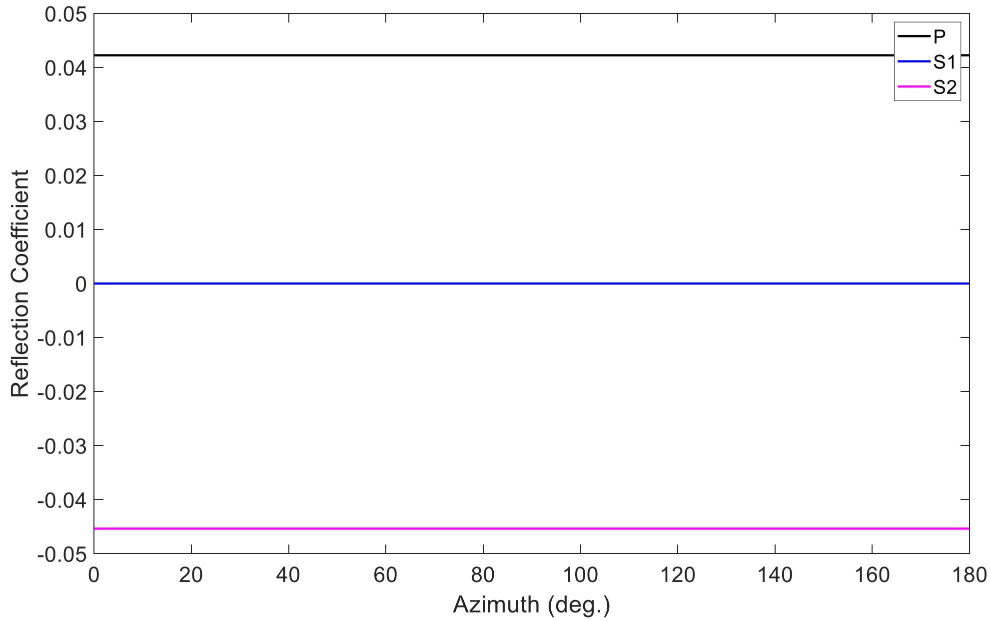

Figure 37 Reflection coefficients for P, S_1, and S_2waves when the time t=1 s.

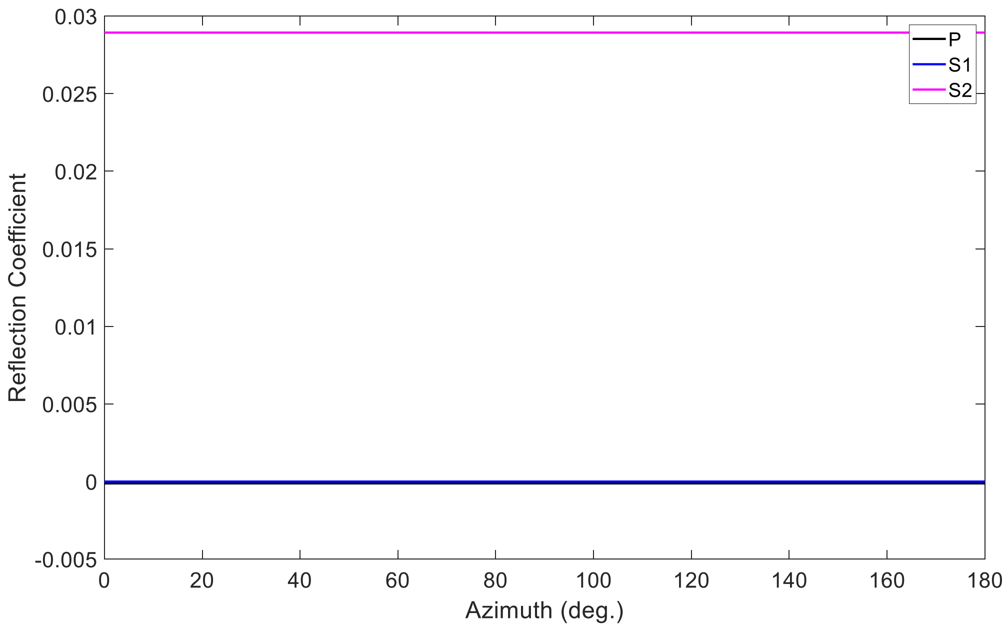

Figure 38 Reflection coefficients for P, S_1, and S_2 waves when the time t=3 s.

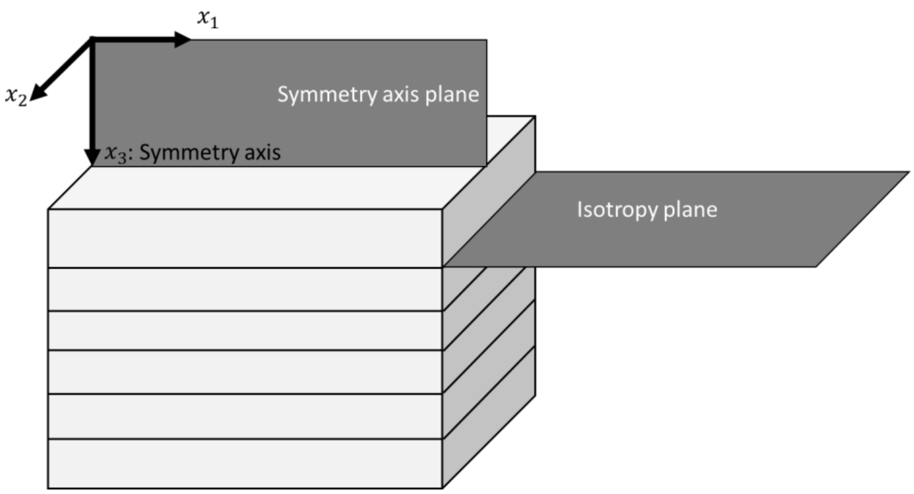

Figure 39 Schematic of VTI medium.

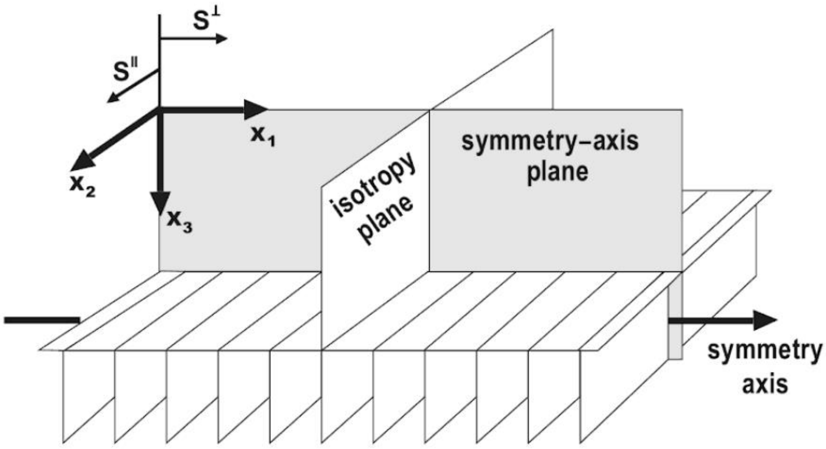

Figure 40 Schematic of HTI medium. From Tsvankin (2001).

The shear-wave splitting in VTI medium of my modeling could be treated as a special case of splitting. Compared to HTI medium (*Figure 40*), the symmetry axis of VTI medium is x_3 (*Figure 39*). The symmetry axis of VTI will always be inside the plane of vertically travelling waves through the model no matter how the azimuth changes, which means that the slow S wave could not be observed at any azimuth (like the 0-degree azimuth case in HTI medium).

5.3 Conclusions

In this chapter, I studied the effect of fracture layer thickness on shear wave splitting for both SV and SH incidence. The thickness varies from 500 m (five times of S wavelength) to 1500 m (15 times of S wavelength). The background velocity of P wave is 4000 m/s. The background velocity of S wave is 2000 m/s. The estimated two-way traveltime is 0.5 s when the fracture layer thickness is 500 m and is based on the background S wave velocity. I set an anisotropy value of ~14% with the fast symmetry axis along the *y*-axis for the S wave.

For HTI media, we found out that the fracture thickness has to be large enough to observe splitting. Time delays *dt1* (S-P-S_1-S and S-P-S_2-S), *dt2* (S-S_1-S_1-S and S-S_1-S_2-S), and *dt3* (S-S_1-S_2-S and S-S_2-S_2-S) all increase with increasing fractured layer thicknesses. In order to observe shear wave splitting between S-P-S_1-S and S-P-S_2-S from seismic data, the minimum thickness of the fracture layer has to be five times of the S wave wavelength (~500 m for this case). To obtain splitting times *dt2* and *dt3*, the minimum thickness has to be six times of the S wavelength (~600 m).

For VTI media, the calculation of shear wave velocities in the fractured layer indicated that the shear wave did split into one fast S wave and one slow S wave. The numerical modeling results of the reflection coefficients of shear waves, on the other hand, explained why the splitting could not be observed in the synthetic seismogram. In my modeling, the value of reflection coefficients of S_2 wave (slow S wave) is always zero at any azimuth.

Chapter 6

Effect of Fracture Compliance on Reflected Wavefield

Rock physics models and laboratory observations have shown that normal and tangential fracture compliance ratio (Z_N/Z_T) can be sensitive to (1) the stiffness of the fluid filling the fracture, (2) the extent to which this fluid can flow in and out of the fracture during the passage of a seismic wave and (3) the internal architecture of the fracture, including the roughness of the fracture surfaces, the number and size of any asperities and the presence of material filling the fracture (Verdon and Wustefeld, 2013). The effect of a fracture network on seismic waves is determined by its compliance, which in turn is controlled by a variety of physical properties of both the fractures and the background, unfractured rock. The compliance of a fracture set can be further resolved into the compliance of the fractures under normal and under tangential deformation – the normal and tangential compliances are noted as, Z_N and Z_T respectively. Consequently, the understanding of the effect of fracture compliance on seismic wavefields will provide useful information about fractured rocks and allow additional constraints to be placed on reservoir analysis.

First, I calculated the relationships between Thomsen's parameter ε and fracture compliance (Z_N and Z_T) in *Figure 41*, as well as Thomsen's parameter γ and fracture compliance (Z_N and Z_T) in *Figure 42*. Thomsen's parameters for VTI media are described as:

$$\varepsilon = \frac{C_{11} - C_{33}}{2C_{33}}, \tag{6.1}$$

and

$$\gamma = \frac{C_{66} - C_{44}}{2C_{44}}, \tag{6.2}$$

where ε measures the difference between horizontal and vertical P-wave velocities (along the propagation direction), while γ measures the difference between horizontal and vertical SH-wave velocities velocities upon the propagation direction (Thomsen, 1986).

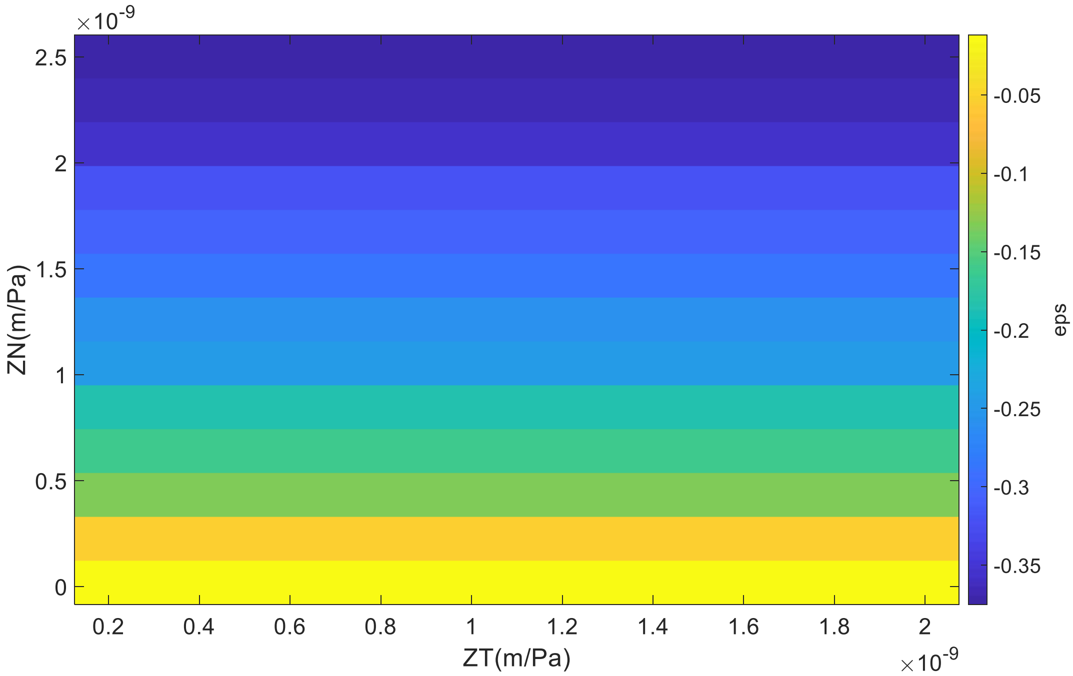

Figure 41 The relationship between Thomsen's ε, the normal fracture compliance Z_N and the tangential fracture compliance Z_T.

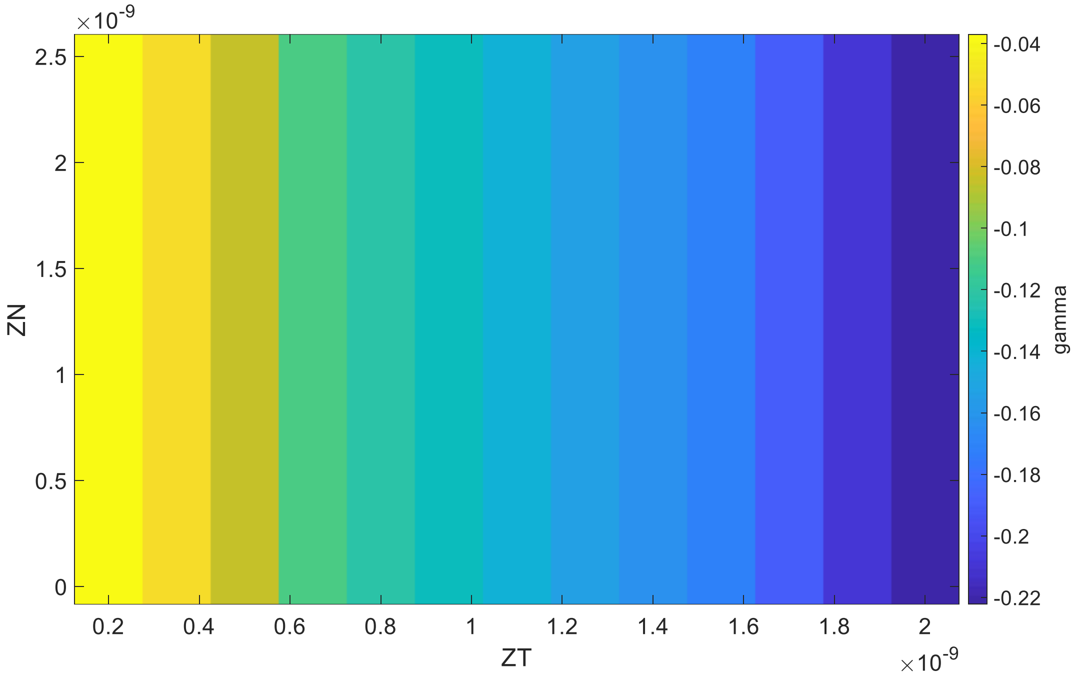

Figure 42 The relationship between Thomsen's γ, the normal fracture compliance Z_N and the tangential fracture compliance Z_T.

According to *Figure 41* and *Figure 42*, Thomsen's ε only changes with the normal fracture compliance Z_N, while Thomsen's γ is only related to tangential compliance Z_T. As a result, shear wave splitting is only affected by the tangential compliance Z_T.

6.1 *P* wave amplitude variation with azimuth

In this part, I calculated the reflected wavefield caused by different fracture normal and tangential compliance ratios based on some published measurement of Z_N/Z_T (*Table 2*). Below is a table of the published measurement of Z_N/Z_T, I investigate the value of Z_N/Z_T from 0.02 to 1.5 to investigate how the normal and tangential ratio will influence the reflected wavefield. Z_T is fixed at 1×10^{-10} m/Pa.

Table 2 Published measurements of Z_N/Z_T from both laboratory and field studies (from Verdon and Wustefeld (2013))

	Reference	Notes	>Z_N/Z_T
1	Verdon *et al.* (2008)	Dry samples. Ultrasonic measurement on grain-scale fabrics.	0.86~1.06
2	Angus *et al.* (2009)	Dry samples. Ultrasonic measurement on grain-scale fabrics .Data collated from a range of literature sources.	0.25~1.5
3(a)	Sayers and Han (2002)	Dry samples. Ultrasonic measurement on grain-scale fabrics.	0.25~3
3(b)		As above, water saturated	0.05~1.1
4(a)	Sayers (1999)	Dry samples. Ultrasonic measurement on shale samples.	0.47~0.8
4(b)		As above, water saturated.	0.26~0.41
5(a)	MacBeth and Schuett (2007)	Dry samples. Ultrasonic measurement on grain-scale fabric. Undamaged sample.	0~0.6
5(b)		As above, sample thermally damaged.	0~1.2
6(a)	Hsu and Schoenberg (1993)	Representative medium of compressed Perspex plates. Ultrasonic measurements on dry samples.	0.8~1
6(b)		As above, honey saturated	0.1
7	Rathore *et al.* (1995)	Synthetic sample containing a population of cracks.	0.46
8(a)	Pyrak-Nolte *et al.* (1990)	Quartz monzonite samples containing a single fracture. Ultrasonic measurements on dry samples.	0.2~0.7
8(b)		As above, water saturated	0.04~0.5
9(a)	Lubbe *et al.* (2008)	Limestone samples cut and reassembled to create a single fracture. Ultrasonic measurements on dry samples.	0.2~0.55
9(b)		As above, honey saturated	0.02~0.05
10	Hobday and Worthington (2012)	Hammer seismic imaging of outcrop of Caithness Flagstone. Water saturated	<=0.1

The background P wave velocity is 2500 m/s, and the S wave velocity is 1000 m/s. The density is 1000 kg/m³. The thickness of the first layer is 500 m, and the thickness of the fractured layer is 625 m which is five times of the P wavelength. The incidence angle is 30 degrees. The source wavelet is a 20 Hz Ricker wavelet. Reflected P wavefield is calculated using different values of Z_N/Z_T because of different azimuths in *Figure 43* ~ *Figure 52*.

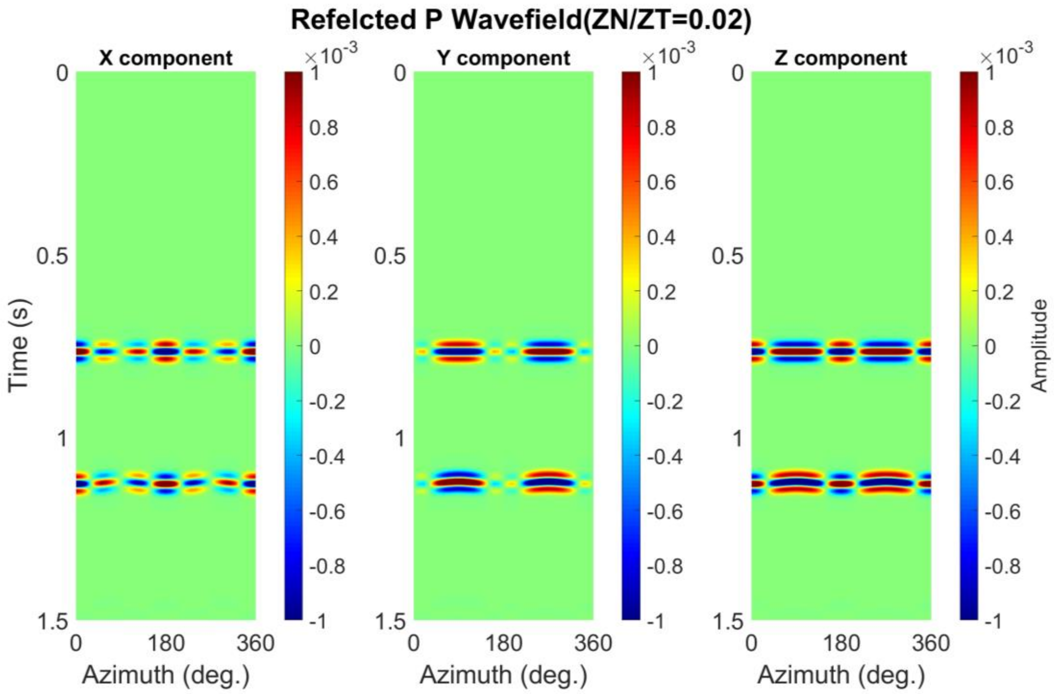

Figure 43 Reflected P wave amplitude variation with azimuths at X, Y and Z components when normal and tangential compliance ratio is 0.02. The source wavelet is a 20 Hz Ricker. The incidence angle is 30 degrees. Z_T is fixed at 1×10^{-10} m/Pa.

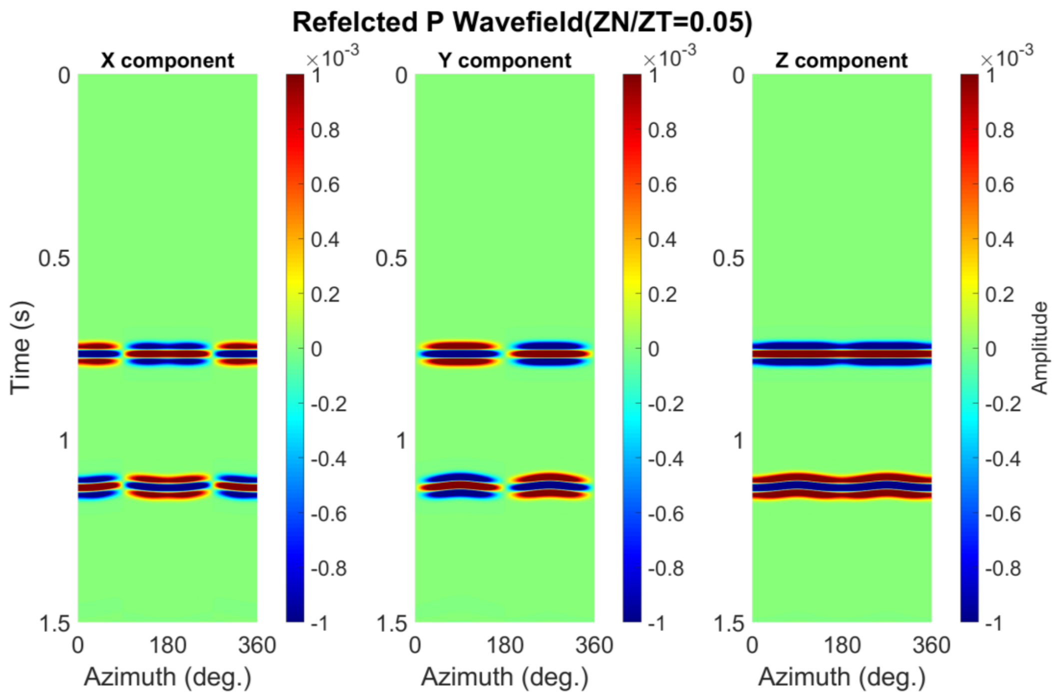

Figure 44 Reflected P wave amplitude variation with azimuths at X, Y and Z components when normal and tangential compliance ratio is 0.05. The source wavelet is a 20 Hz Ricker. The incidence angle is 30 degrees. Z_T is fixed at 1×10^{-10} m/Pa.

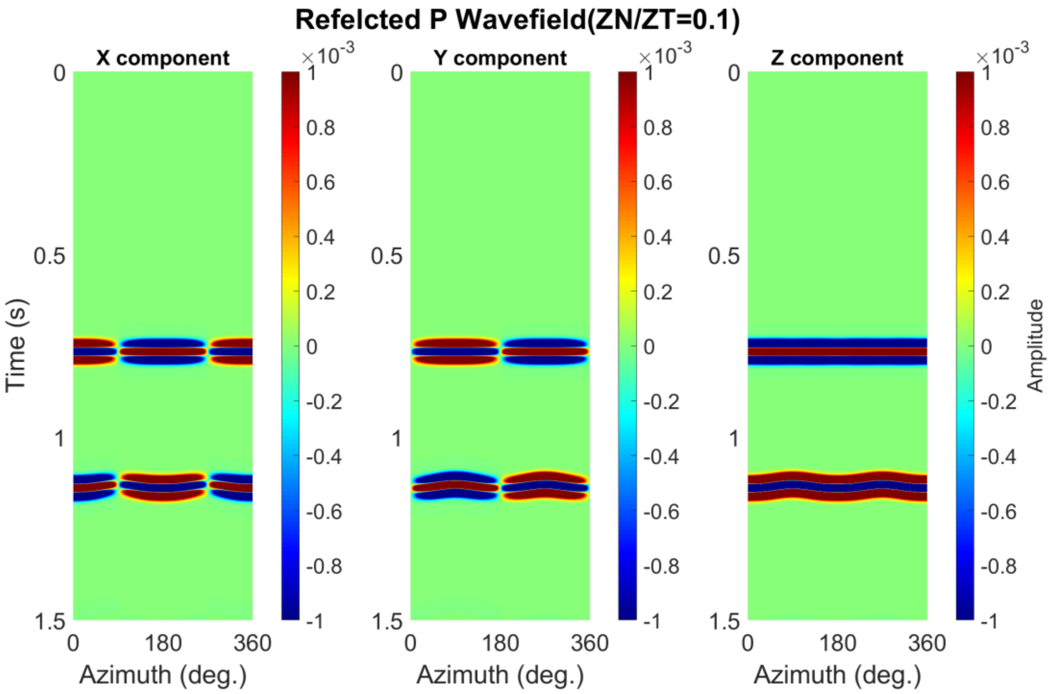

Figure 45 Reflected P wave amplitude variation with azimuths at X, Y and Z components when normal and tangential compliance ratio is 0.1. The source wavelet is a 20 Hz Ricker. The incidence angle is 30 degrees. Z_T is fixed at 1×10^{-10} m/Pa.

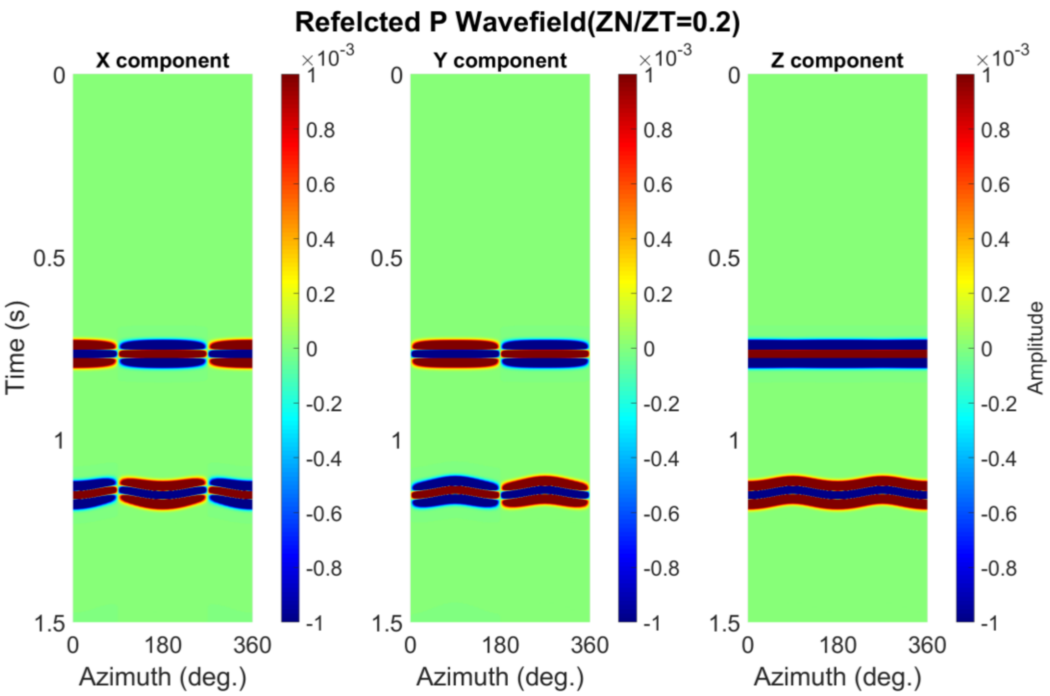

Figure 46 Reflected P wave amplitude variation with azimuths at X, Y and Z components when normal and tangential compliance ratio is 0.2. The source wavelet is a 20 Hz Ricker. The incidence angle is 30 degrees. Z_T is fixed at 1×10^{-10} m/Pa.

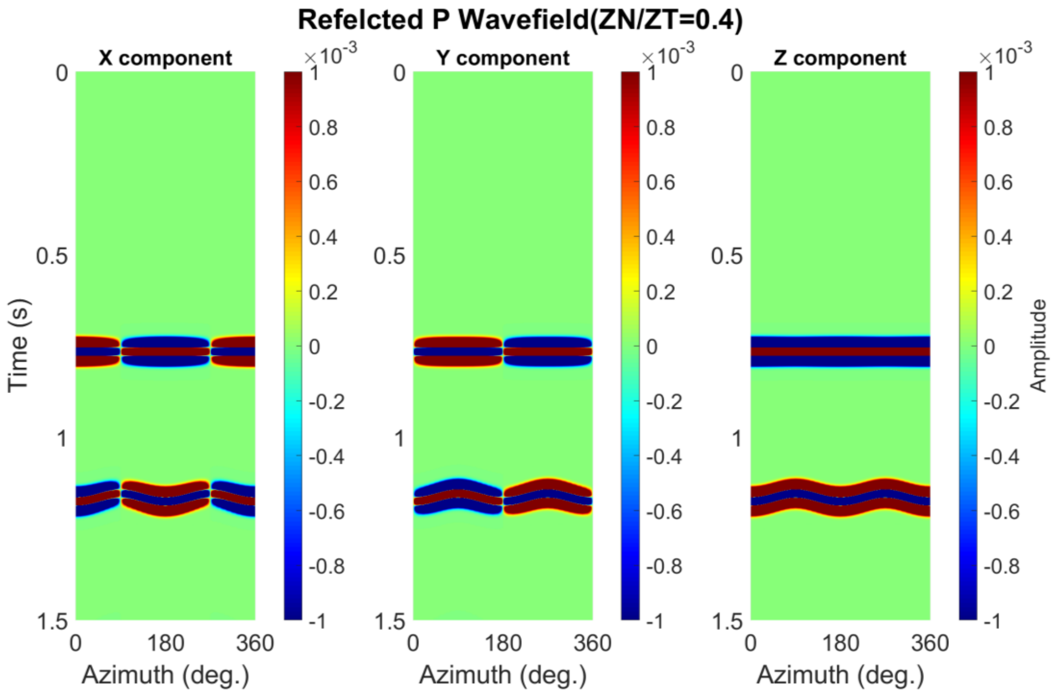

Figure 47 Reflected P wave amplitude variation with azimuths at X, Y and Z components when normal and tangential compliance ratio is 0.4. The source wavelet is a 20 Hz Ricker. The incidence angle is 30 degrees. Z_T is fixed at 1×10^{-10} m/Pa.

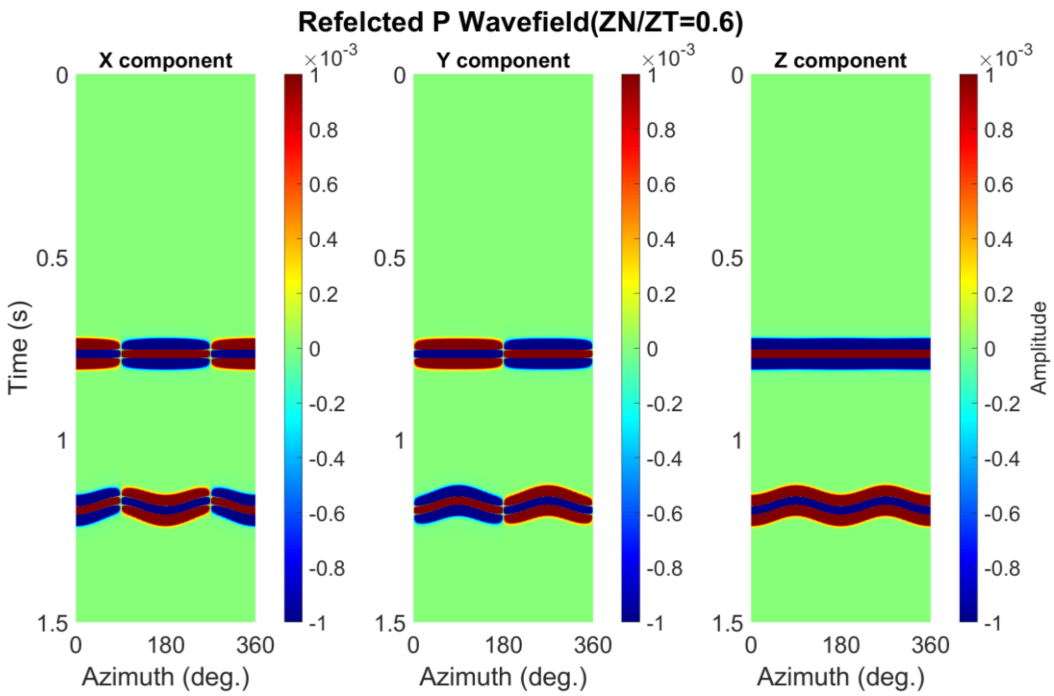

Figure 48 Reflected P wave amplitude variation with azimuths at X, Y and Z components when normal and tangential compliance ratio is 0.6. The source wavelet is a 20 Hz Ricker. The incidence angle is 30 degrees. Z_T is fixed at 1×10^{-10} m/Pa.

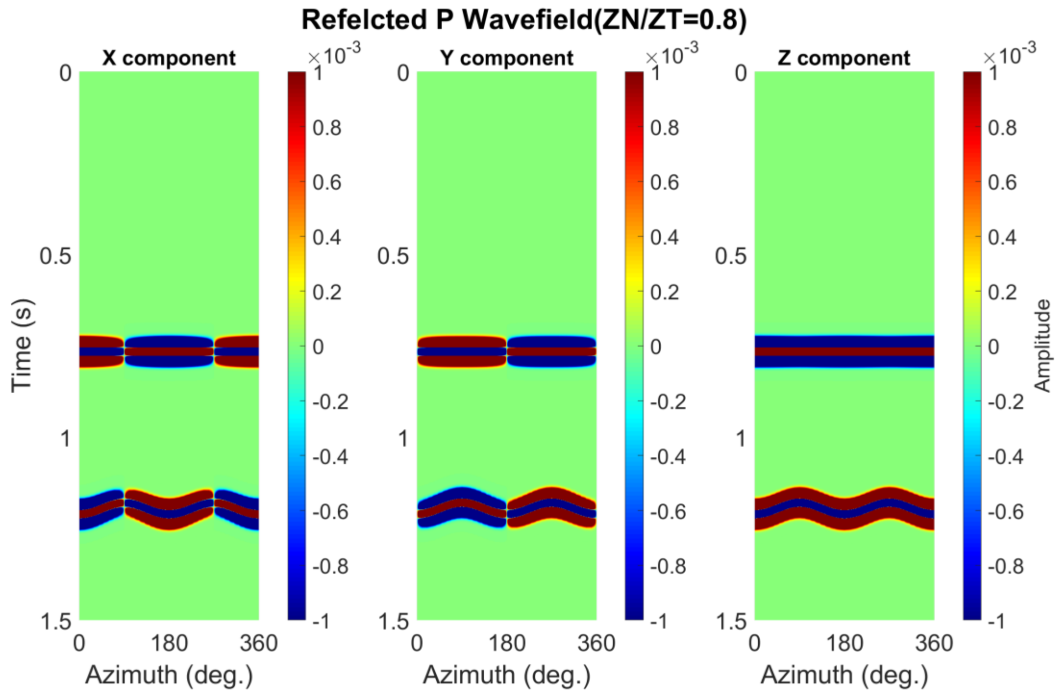

Figure 49 Reflected P wave amplitude variation with azimuths at X, Y and Z components when normal and tangential compliance ratio is 0.8. The source wavelet is a 20 Hz Ricker. The incidence angle is 30 degrees. Z_T is fixed at 1×10^{-10} m/Pa.

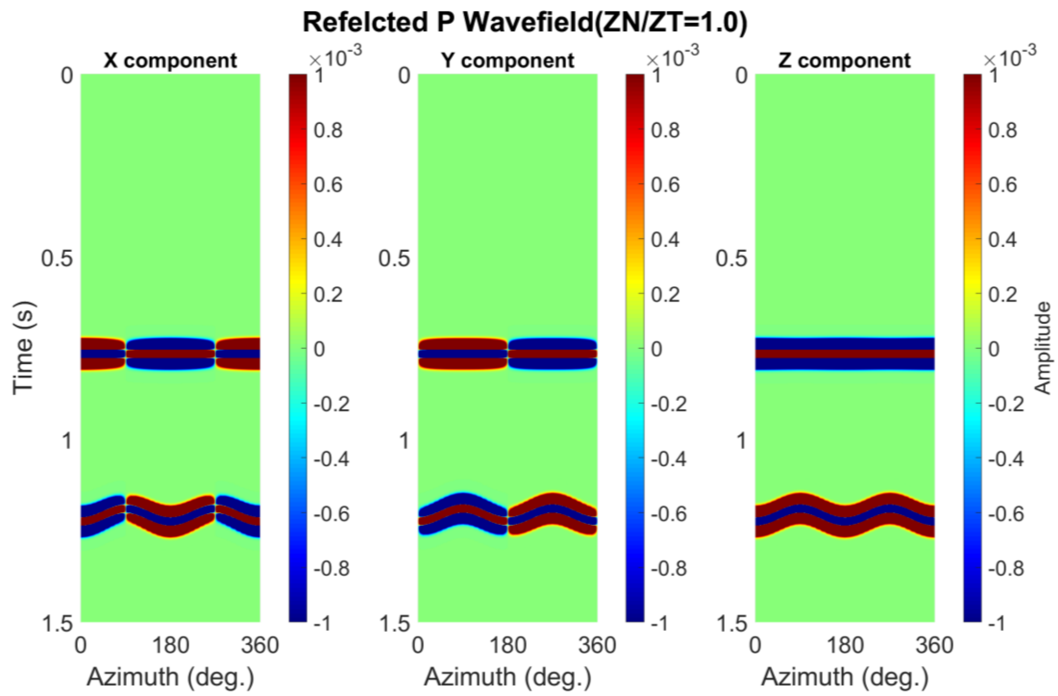

Figure 50 Reflected P wave amplitude variation with azimuths at X, Y and Z components when normal and tangential compliance ratio is 1.0. The source wavelet is a 20 Hz Ricker. The incidence angle is 30 degrees. Z_T is fixed at 1×10^{-10} m/Pa.

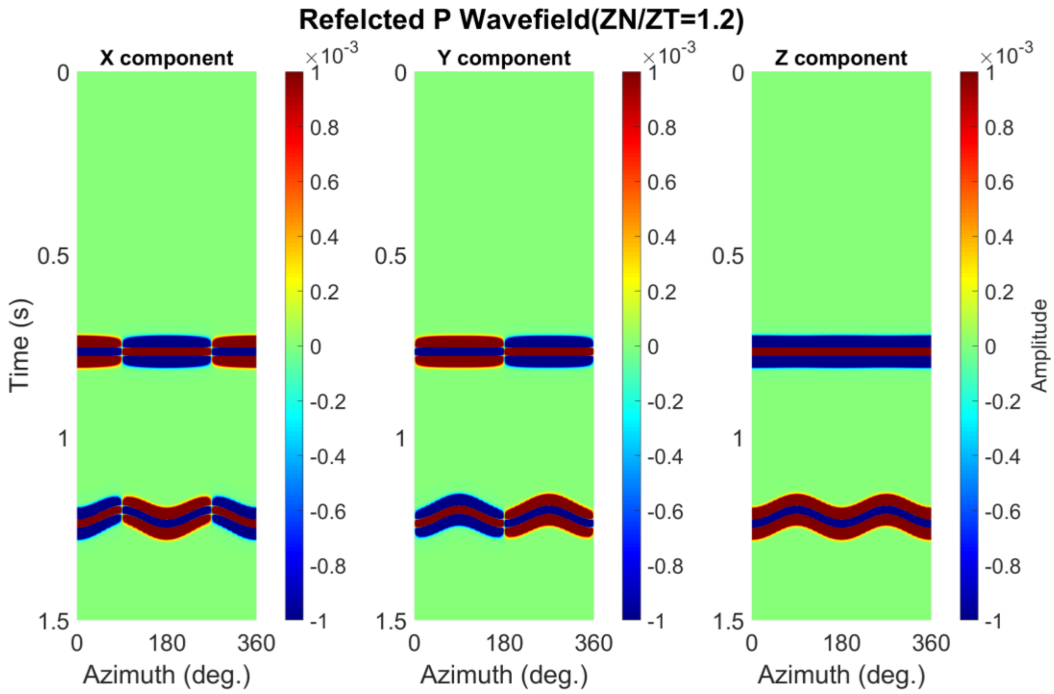

Figure 51 Reflected P wave amplitude variation with azimuths at X, Y and Z components when normal and tangential compliance ratio is 1.2. The source wavelet is a 20 Hz Ricker. The incidence angle is 30 degrees. Z_T is fixed at 1×10^{-10} m/Pa.

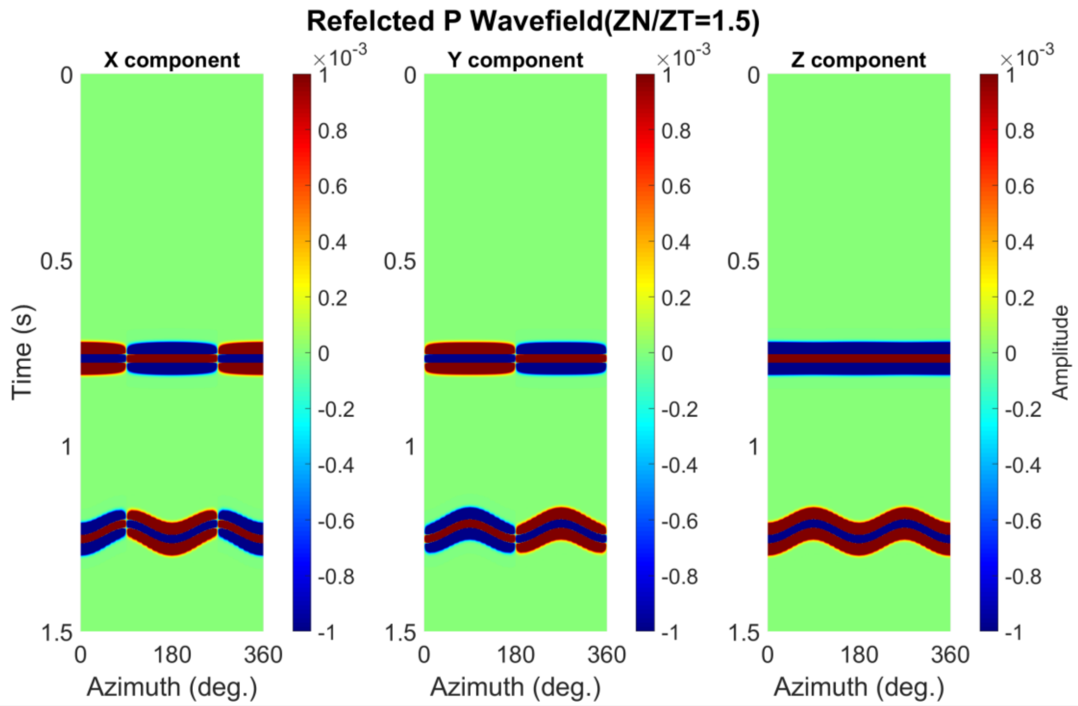

Figure 52 Reflected P wave amplitude variation with azimuths at X, Y and Z component when normal and tangential compliance ratio is 1.5. The source wavelet is a 20 Hz Ricker. The incidence angle is 30 degrees. Z_T is fixed at 1×10^{-10} m/Pa.

The ratio between fracture normal compliance and tangential (vertical) compliance indicates the fracture fluid property. If this value is between 0 and 0.2, fractures are considered to be mainly filled with liquid (Liu *et al.*, 2018). For Z_N/Z_T below 0.1, especially when the ratio is 0.02, the variation of amplitude of reflected P shows discontinuities. When the ratio of Z_N and Z_T is less than 0.02, the amplitude of azimuthal P wave data are not accurate (*Figure 43*) for extracting useful information of fracture parameters.

Since the value of Z_T is fixed in *Figure 43 ~ Figure 52*, the reflections from the bottom of the fractured layer on each azimuth tends to arrive later as the normal fracture compliance increases. As the values of Z_N/Z_T increase from 0.02 to 1.5, the liquid content in the fluid drops, the azimuthal variation of P wave velocity and amplitude tend to be more distinct. As a result, the method of using azimuthal P wave data to predict fracture orientation and density would have better accuracy if the fracture compliance ratio is larger than 0.02.

6.2 Shear wave splitting

The fracture normal compliance and tangential (vertical) compliances are related to the fracture fluid property. If we know the relationship between splitting time and the fracture compliance, we are able to indicate the physical property of fracture such as fluid property. Based on published measurements of Z_N/Z_T from both laboratory and field studies in *Table 2*, I calculated the splitting time *dt1* (time delay between S-P-S_1-

S and S-P-S_2-S), *dt2* (time delay between S-S_1-S_1-S and S-S_1-S_2-S) and *dt3* (S-S_1-S_2-S and S-S_2-S_2-S) caused by different fracture normal and tangential compliance ratio from 0.02 to 1.5 at 30 degree azimuth for both SV incidence (*Figure 55* and *Figure 56*) and SH incidence (*Figure 57* and *Figure 58*).

According to *Figure 42*, the Thomsen's γ is only related to the tangential fracture compliance Z_T. In order to investigate the effect of Z_N/Z_T on S wavefield, the tangential fracture compliance Z_N is set at 1×10^{-10} m/Pa. Then, the change of the value of Z_N/Z_T is all caused by Z_T. The background P wave velocity is 2500 m/s, and the S wave velocity is 1000 m/s. Density is 1000 kg/m³. The thickness of the first layer is 500 m, and the thickness of the fractured layer is 2000 m. The incidence wave is an SV wave with an incidence angle of 10 degrees. The central frequency is 20 Hz. The reflected S wavefield has been calculated at different values of Z_N/Z_T at the 30-degree azimuth in *Figure 53*. We show the ray paths of each seismic event in *Figure 54*.

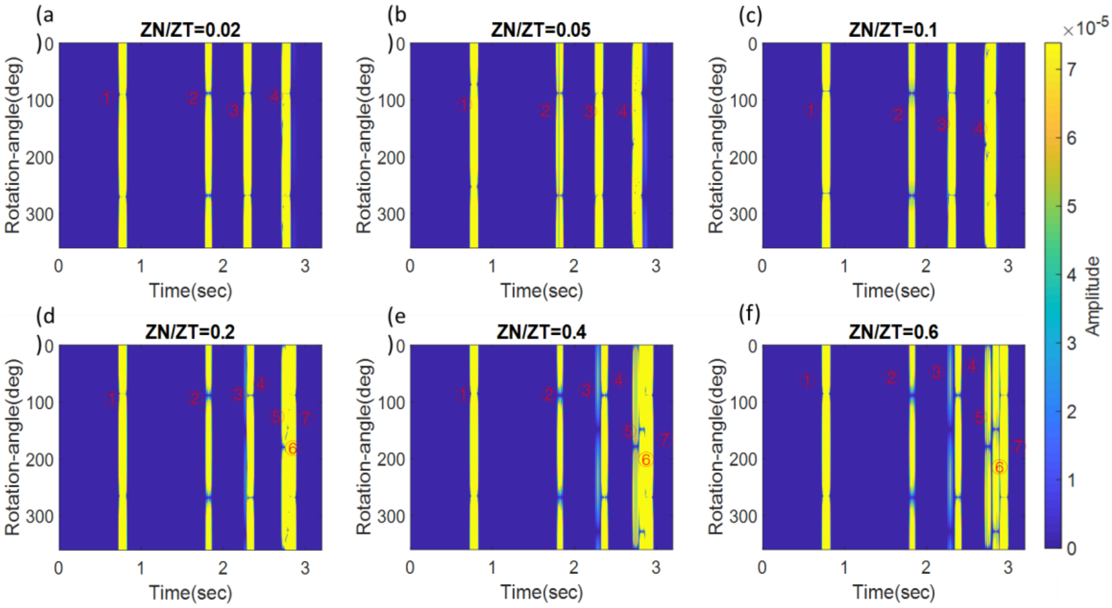

Figure 53 Reflection of *S* wave in layer 1 at the 30-degree azimuth due to different normal and tangential compliance ratio.

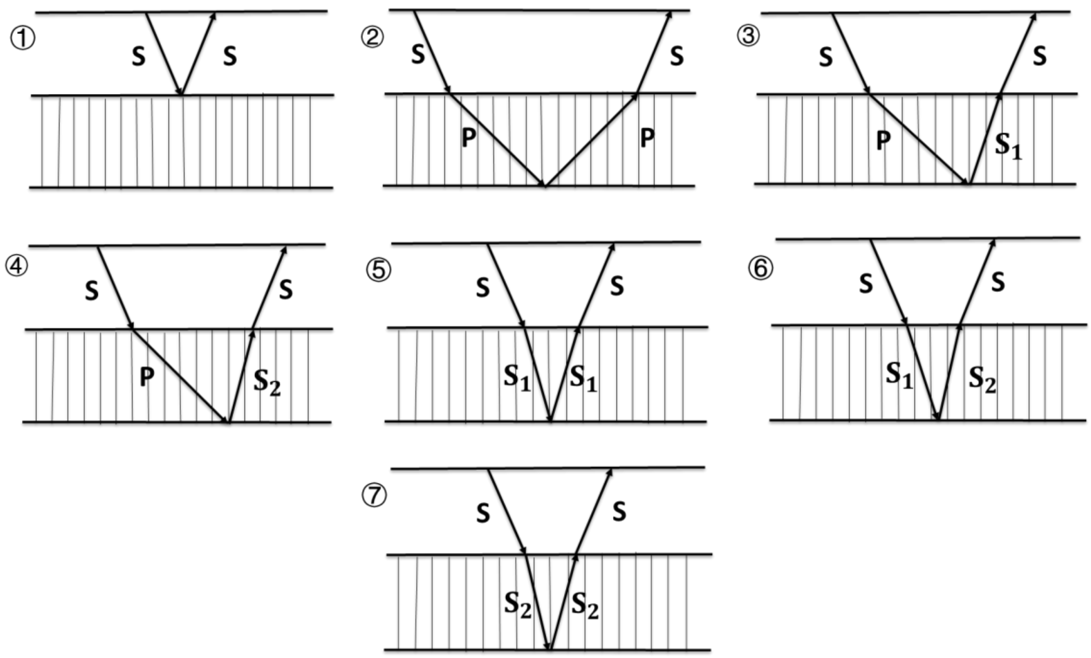

Figure 54 Schematic of ray paths of seismic event 1~7 when the azimuth is 30 degrees.

Seismic event 1 ~ 7 in *Figure 53* (f) are S-S reflection, S-P-P-S reflection, S-P-S_1-S reflection, S-P-S_2-S reflection, S-S_1-S_1-S reflection, S-S_1-S_2-S reflection, S-S_1-S_2-S reflection, and S-S_2-S_2-S reflection, respectively. However, we observe only four seismic events directly from *Figure 53* (a) ~ (c). That's because S-P-S_1-S and S-P-S_2-S reflection (seismic event 3 and 4 in *Figure 53* (f)) completely overlap each other when the value of Z_N/Z_T is less than 0.1, as well as S-S_1-S_1-S, S-S_1-S_2-S, and S-S_2-S_2-S reflection (seismic event 5, 6, and 7 in *Figure 53* (f)). From *Figure 53* (d) ~ (f), event 3 and 4, event 5, 6 and 7 begin to separate as the value of Z_N/Z_T increases. When the value of Z_N/Z_T is 0.4, we could extract splitting time *dt1* (time delay between S-P-S_1-S and S-P-S_2-S reflection), *dt2* (time delay between S-S_1-S_1-S and S-S_1-S_2-S reflection), and *dt3* (S-S_1-S_2-S and S-S_2-S_2-S reflection) directly from *Figure 53* (f). The relationships between splitting time and Z_N/Z_T at a fixed thickness of fractured layer for SV and SH incidence wave at the 30-degree azimuth are displayed through *Figure 55* ~ *Figure 58*.

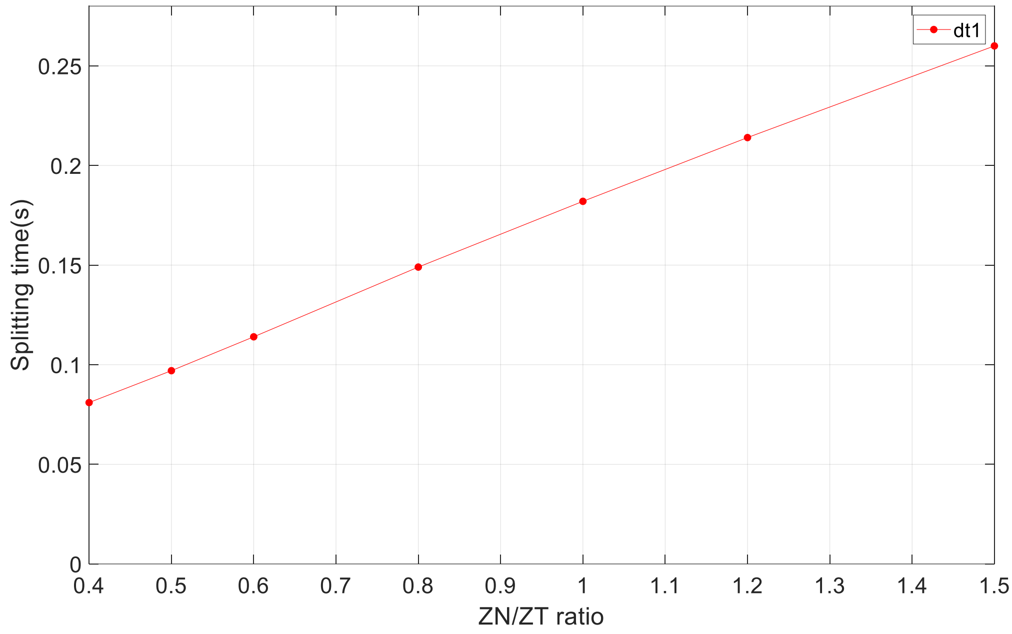

Figure 55 Time difference of S-P-S_1-S and S-P-S_2-S (*dt1*) due to different normal and tangential fracture compliance ratio at the 30-degree azimuth for *SV* incidence. Z_N is fixed at 1×10^{-10} m/Pa.

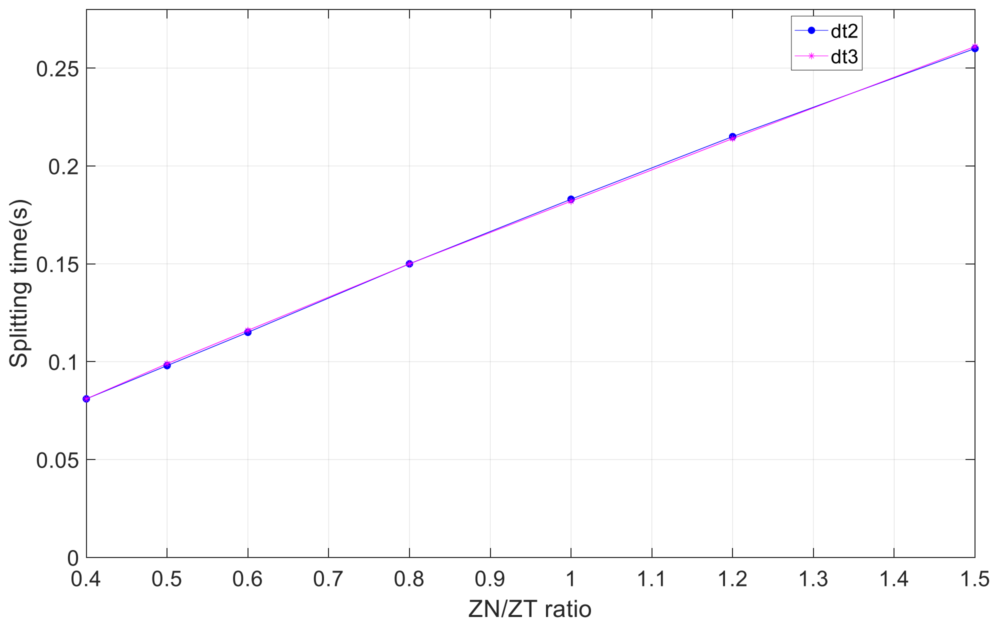

Figure 56 Time difference of S-S_1-S_1-S and S-S_1-S_2-S (*dt2*), S-S_1-S_2-S and S-S_2-S_2-S (*dt3*) due to different normal and tangential fracture compliance ratio at the 30-degree azimuth for *SV* incidence. Z_N is fixed at 1×10^{-10} m/Pa.

In the same way, I plotted the relationship between splitting time (*dt1*, *dt2* and *dt3*) and the Z_N/Z_T ratio (*Figure 57* and *Figure 58*).

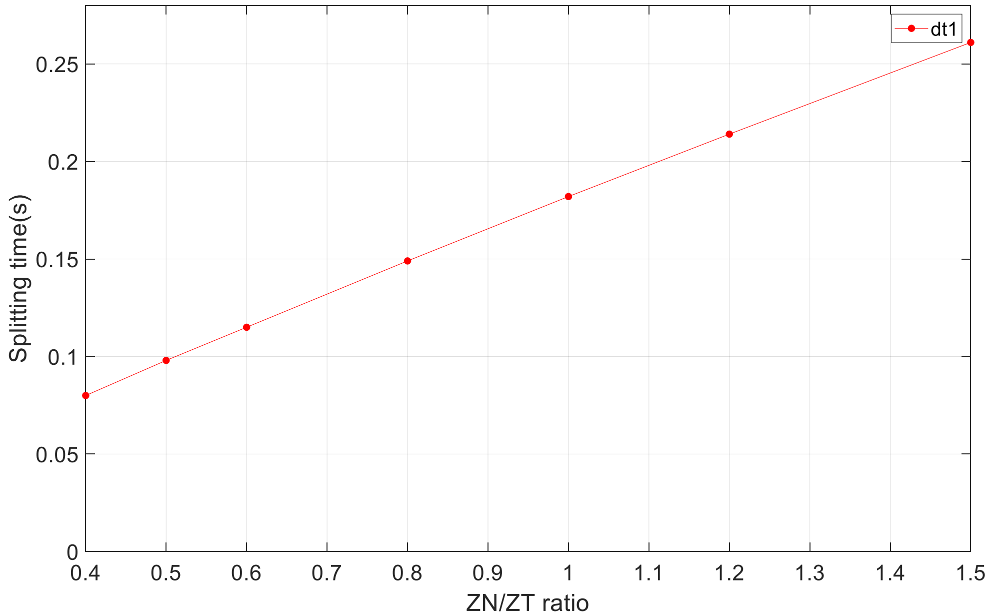

Figure 57 Time difference of S-P-S_1-S and S-P-S_2-S (*dt1*) due to different normal and tangential fracture compliance ratio at the 30-degree azimuth for *SH* incidence. Z_N is fixed at 1×10^{-10} m/Pa.

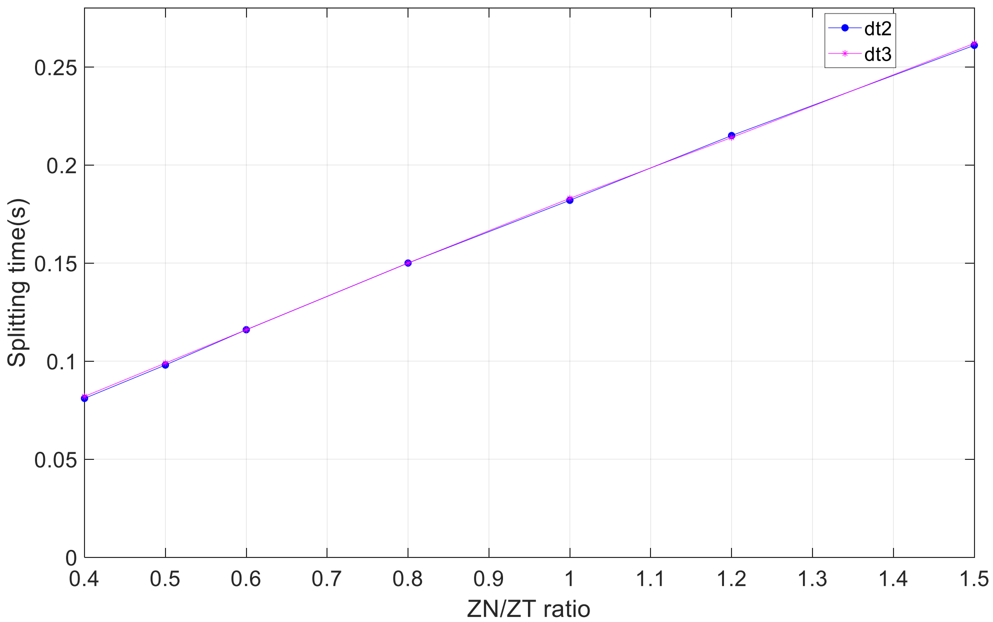

Figure 58 Time difference of S-S_1-S_1-S and S-S_1-S_2-S (*dt2*), S-S_1-S_2-S and S-S_2-S_2-S (*dt3*) due to different normal and tangential fracture compliance ratio at the 30-degree azimuth for SH incidence. Z_N is fixed at 1×10^{-10} m/Pa.

For both SV and SH incidence, the splitting time *dt1*, *dt2* and *dt3* have an overall tendency to increase as the Z_N/Z_T ratio increases from 0.4 to 1.5. However, when the ratio is less than 0.4, it is hard to observe shear wave splitting or extract the splitting time from synthetic seismic data according to my model. As a result, this shear wave splitting analysis method is not efficient for fracture characterization when the fractures have low Z_N/Z_T ratios. If the Z_N/Z_T ratio is between 0 and 0.2, using shear wave splitting analysis to extract the polarization of fast shear waves and the time delay between the two split shear waves for analyzing fracture orientation and fracture density is not feasible.

6.3 Conclusions

In this chapter, I first studied the reflected P wavefield caused by different normal and tangential fracture compliance ratio from 0.02 to 1.5 based on some published measurements of Z_N/Z_T from laboratory and field studies. If the ratio of Z_N and Z_T is less than 0.02, the azimuthal P wave data are not accurate for extracting useful information of fracture parameters (fracture orientation and density).

Second, I found that the Thomsen's γ is only related to tangential compliance Z_T and not the normal compliance, Z_N. Therefore, shear wave splitting is only affected by the tangential compliance Z_T.

Third, if the Z_N/Z_T is low (<0.4) when Z_N is fixed, shear wave splitting would be difficult to observe in the synthetic data even the fracture thickness is thick enough according to my modeling.

Chapter 7

Transmitted Wavefield of an Anisotropic Subducting Slab Model

Seismic waves that propagate through the mantle and recorded at the earth surface provide us a good way to understand the mantle deformation at depth. Elastic anisotropy in the mantle results from deformation, which makes the measurement of seismic anisotropy the best tool available for geophysicists to directly probe patterns of deformation at depth (Long and Silver, 2009). Shear wave splitting has become a popular tool for characterizing anisotropy in the Earth since earlier studies (e.g., Keith and Crampin, 1977; Kosarev *et al.*, 1984; Silver and Chan, 1988). The importance of the dependence of the shear wave fast splitting direction on the seismic wave incidence angle and the slab dip has been emphasized. The polarization of the fast S wave is mainly controlled by the nature of anisotropy embedded in the oceanic asthenosphere and the dipping angle of the subducting slab (Song and Kawakatsu, 2012).

In this chapter, I will focus on transmitted waves propagating through a fractured subducting slab model for both SV incidence and SH incidence waves. Upon propagating through an anisotropic slab, the shear wave will split into two orthogonally polarized components and accumulate a delay time between the fast and slow shear waves. There are two splitting parameters measured from seismic records:

ϕ and dt. They correspond to the polarization of the fast S phase and the time delay between the fast and slow components, respectively.

7.1 HTI model

In my model, the slab strikes along the north and dips southwest with θ_{dip} as the dipping angle (*Figure 59* and *Figure 60*). I consider the fractures in the slab as azimuthal anisotropy with a tilted fast symmetry axis parallel to the slab dip under the global coordinate system. For global coordinate system, the X'- component is along the horizontal line, the Y'- component points into the page and the Z'- component is vertical following the right-hand rule. For local coordinate system, the X- component is along the slab dip and the Z- component is perpendicular to the slab dip. In both local and global coordinate system, the Y- component and the Y'- component stay the same. The local coordinate system could be considered as the result of global coordinate system rotating around the Y coordinate anticlockwise by θ_{dip} (*Figure 59*).

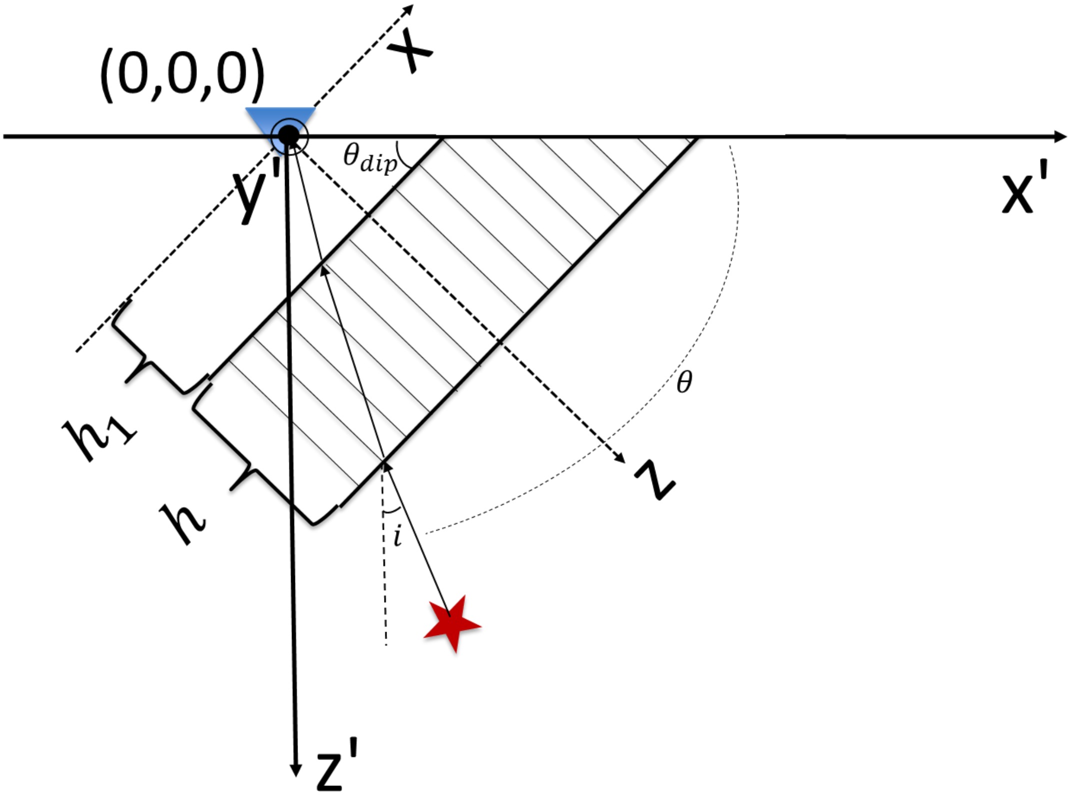

Figure 59 Schematic of a fractured subducting slab model under two sets of coordinate systems. (X, Y, Z) is defined as the local coordinate system. (X', Y', Z') is defined as the global coordinate system. Red star denotes the source. Blue triangle denotes the receiver. i denote the incidence angle. h is the thickness of the fracture layer. The slab is dipping southwest with θ_{dip} as the dipping angle. The slab strike is along the y-axis.

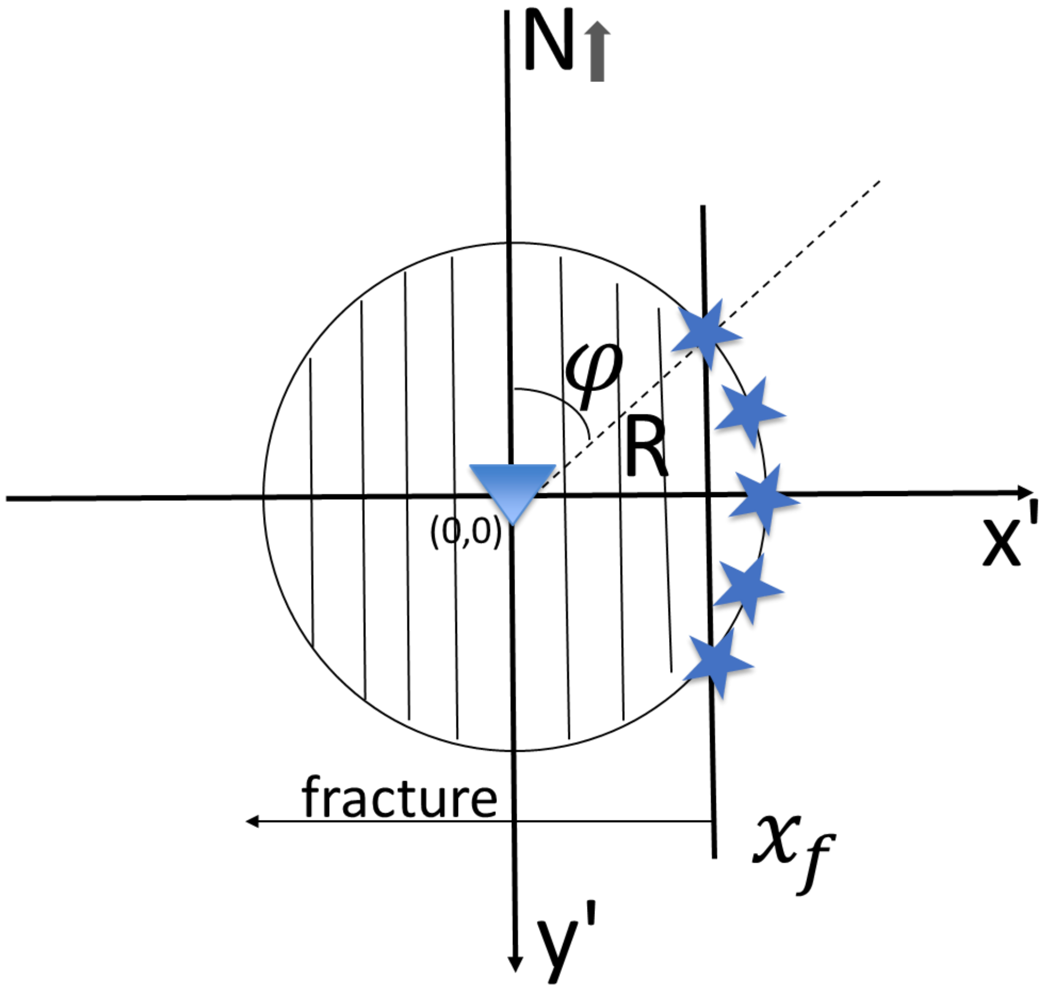

Figure 60 Schematic of geometry of seismic acquisition from top view. Blue stars are the projection on the surface of sources that are deep down the ground in layer 3 of the three-layered model. The blue triangle at zero is the receiver at the surface. The slab is embedded with a set of fractures. x_f is the value of x-coordinate when the source location that is the nearest to the fracture is projected at the surface. φ is the azimuth, defined as the angle between the north and the source to receive line. The slab strike is along the 0-degree azimuth. The slab is dipping southwest (*Figure 59*).

In my model, the transmitted wavefields are recorded at the surface at different azimuths from φ=40 to 140 degrees (*Figure 60*). The source to receiver distance R is 50km. The background P wave velocity is 6000 m/s and the S wave velocity is 4000 m/s. Density is 1000 kg/m³. The slab is 20 km thick. Using the local coordinate system, I consider my model as a three-layer model with the top layer isotropic (layer 1), the second layer fractured (the slab) and the bottom layer isotropic (layer 3). I treat the anisotropy in the slab as an HTI medium. I calculated the transmitted wavefield under the local coordinate system and then transformed to global system using Equation (7.1):

$$\begin{cases} x' = \cos\theta \bullet x - \sin\theta \bullet z \\ y' = y \\ z' = \sin\theta \bullet x + \cos\theta \bullet z \end{cases} . \tag{7.1}$$

The azimuthal anisotropy of 25% is set with a fast symmetry axis along the slab dip for S wave. I will calculate the splitting time and fast polarization as a function of incidence angle at slab dip angle 15, 40, and 60 degrees for both SV incidence and SH incidence.

7.1.1 *SV* incidence

The incoming S wave in isotropic layer 3 is the SV wave. The SV wave means that the shear wave is polarized in the source-receiver acquisition plane. The transmitted wavefields recorded at layer 1 are S-P-S, S-S_1-S and S-S_2-S waves (*Figure 61*). S_1 and S_2 mean fast and slow S wave, respectively in fractured layer 2. The time difference between S-S_1-S and S-S_2-S is *dt* in *Figure 61*. The polarization angle of S_1 is ϕ in *Figure 62*.

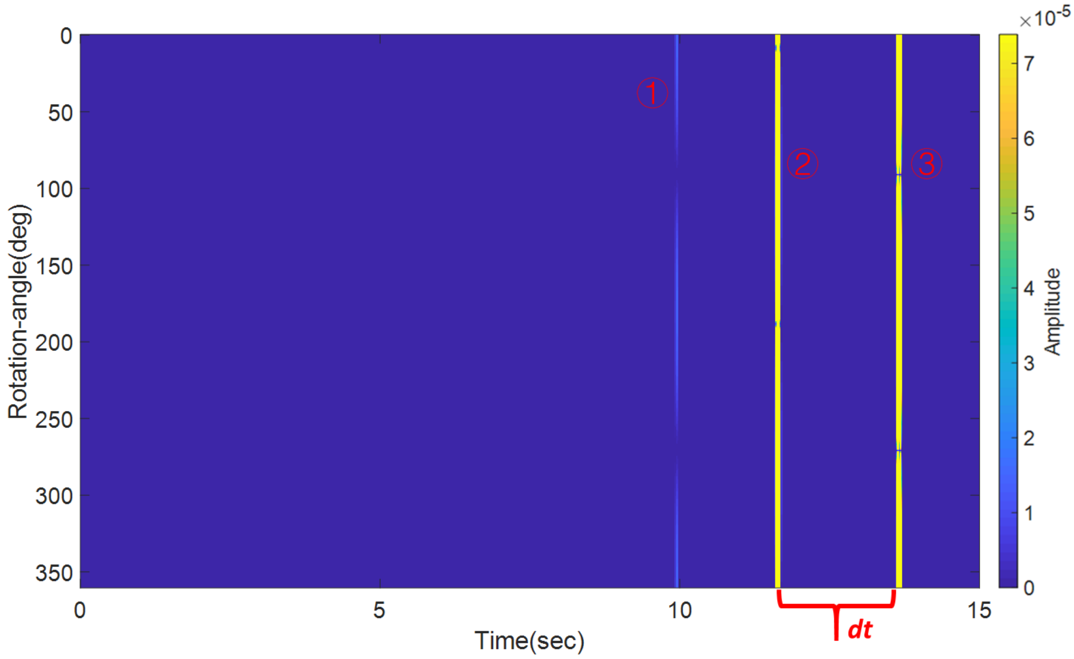

Figure 61 Transmission of S wave in layer 1 at the 60-degree azimuth. The incidence angle i is 10 degrees. The slab dipping angle is 40 degrees. Seismic events 1 ~ 3 are: S-P-S, S-S_1-S, and S-S_2-S waves.

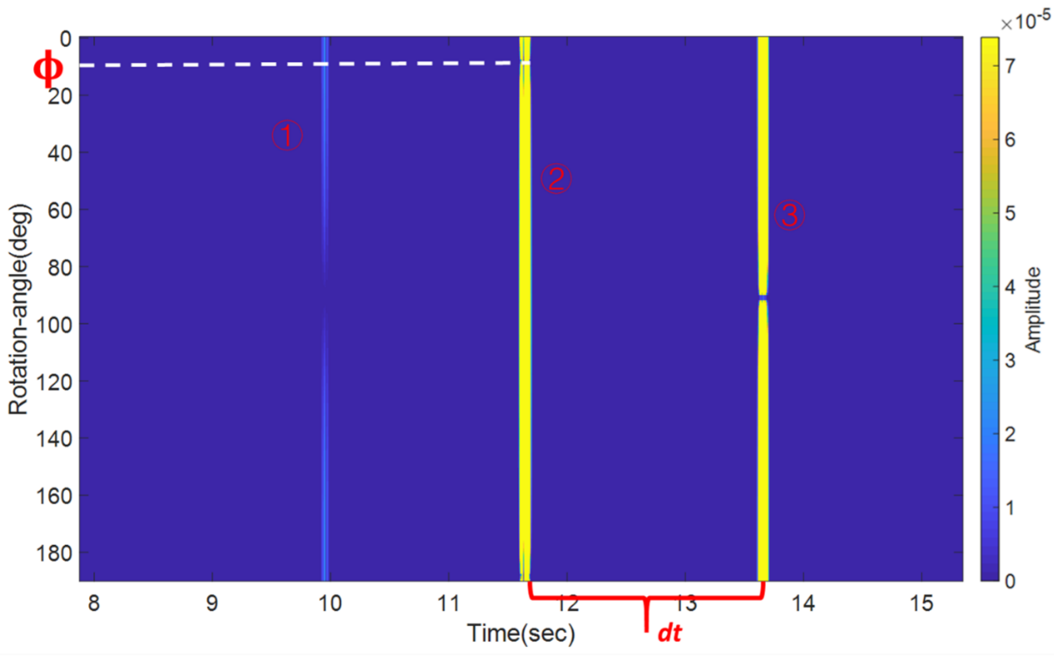

Figure 62 Transmission of S wave in layer 1 at the 60-degree azimuth after zooming in *Figure 61*. The incidence angle i is 10 degrees. The slab dipping angle is 40 degrees. Seismic events 1 ~ 3 are: S-P-S, S-S_1-S, and S-S_2-S waves.

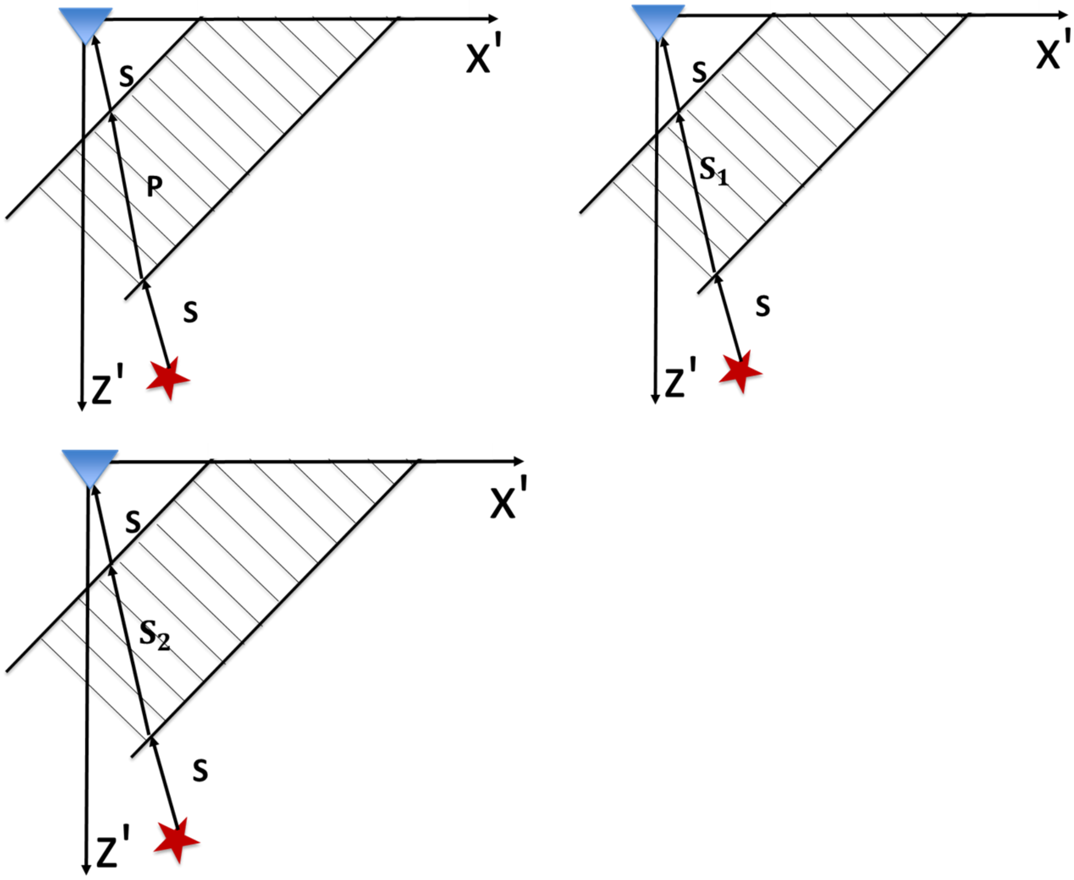

Figure 63 Schematic of ray paths of seismic event 1~3 when the azimuth is 60 degrees (global coordinate system).

The time delay *dt* between S-S_1-S and S-S_2-S will be calculated at azimuth φ = 60 degrees caused by different incidence angles i from 5 to 25 every 5 degree (i is defined in *Figure 59* and φ is defined in *Figure 60*). I will also investigate the time delay caused by different slab dipping angle θ_{dip} = 15, 40, and 60 degrees (*Figure 64*, *Figure 66* and *Figure 68*). The fast polarization angle ϕ is also obtained in the same way at different slab dipping angles and incidence angles (*Figure 65*, *Figure 67* and *Figure 69*).

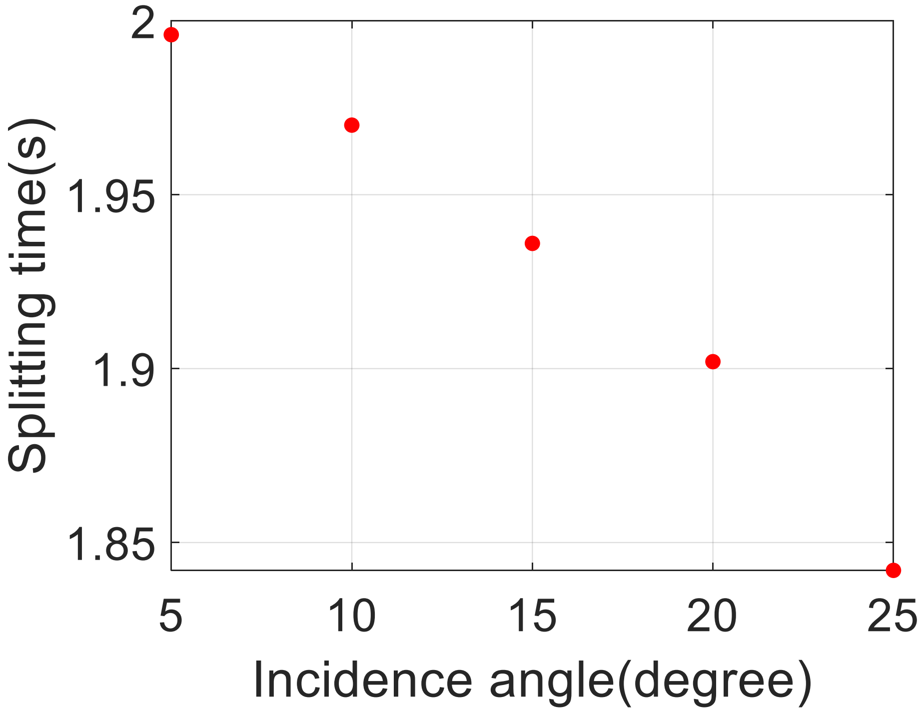

Figure 64 Time delay (splitting time) dt of S-S_1-S and S-S_2-S due to different incidence angle i at the 15-degree slab dip angle.

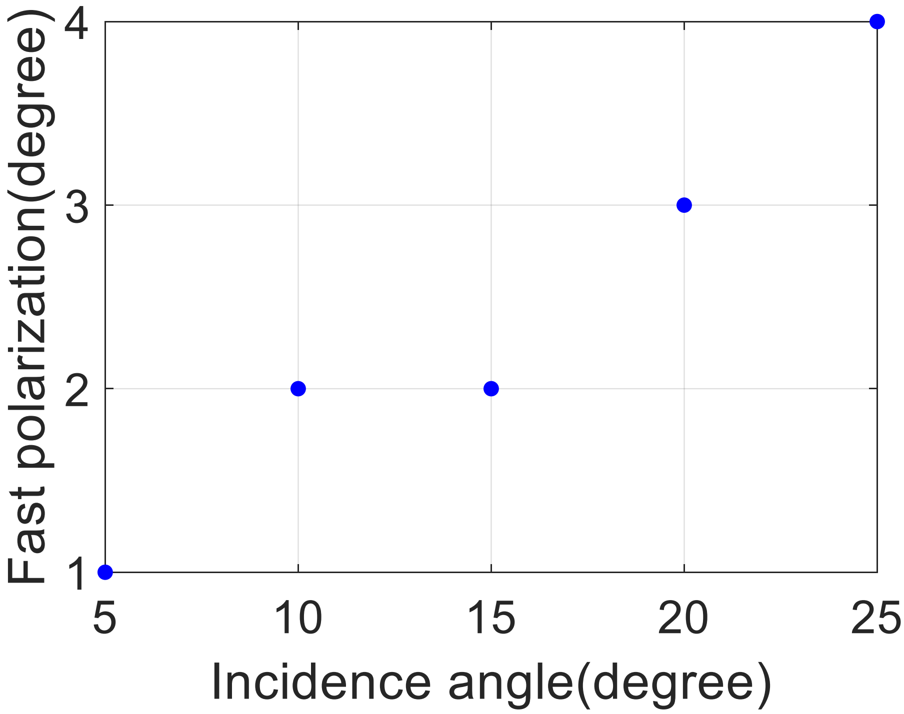

Figure 65 The polarization angle (ϕ) of fast S wave (S-S_1-S) due to different incidence angles i at the 15-degree slab dip angle.

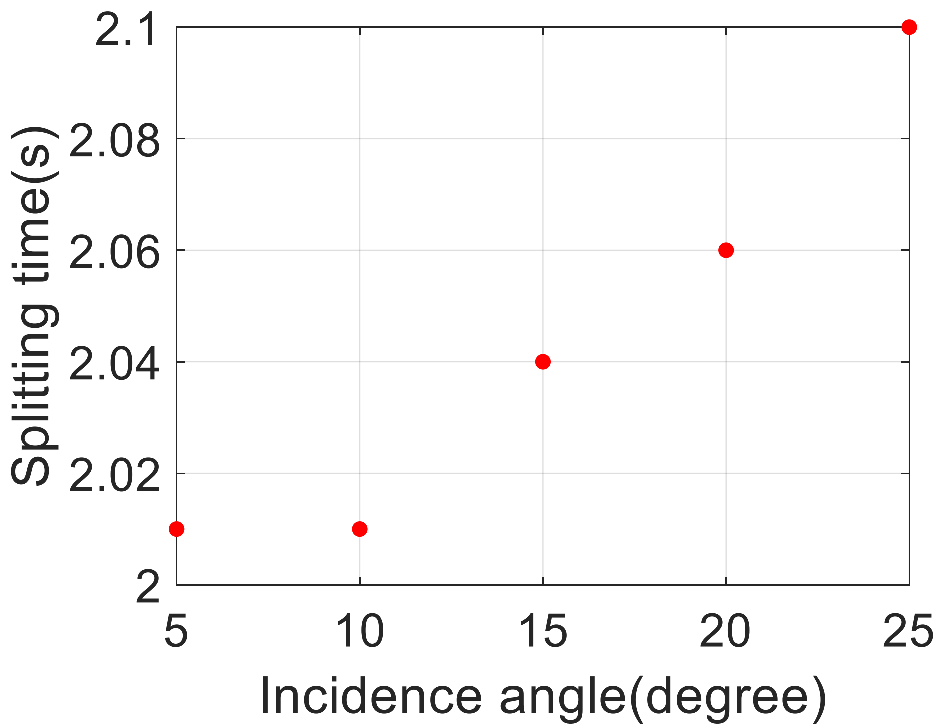

Figure 66 Time delay (splitting time) dt of S-S_1-S and S-S_2-S due to different incidence angles i at the 40-degree slab dip angle.

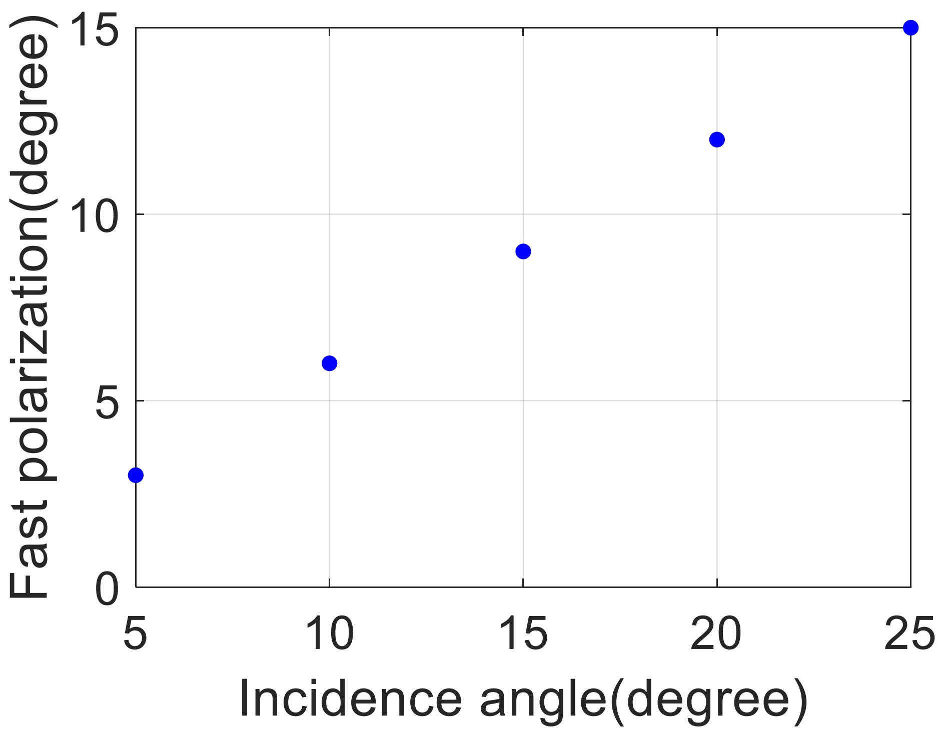

Figure 67 The polarization angle (ϕ) of fast S wave (S-S_1-S) due to different incidence angles i at the 40-degree slab dip angle.

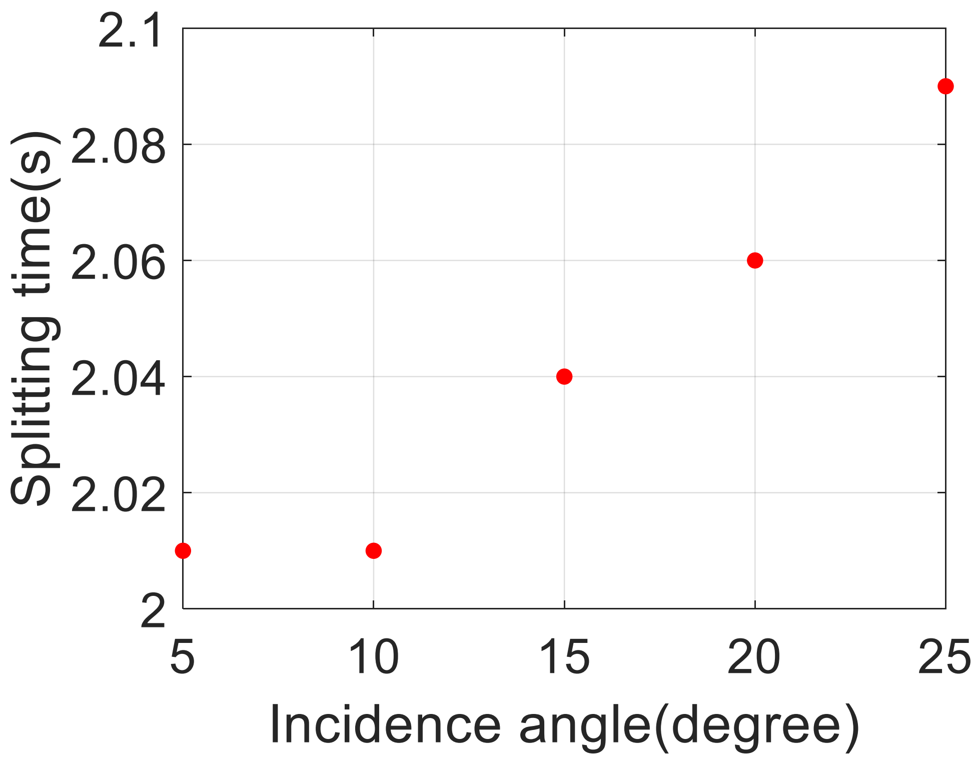

Figure 68 Time delay (splitting time) dt of S-S_1-S and S-S_2-S due to different incidence angles i at the 60-degree slab dip angle.

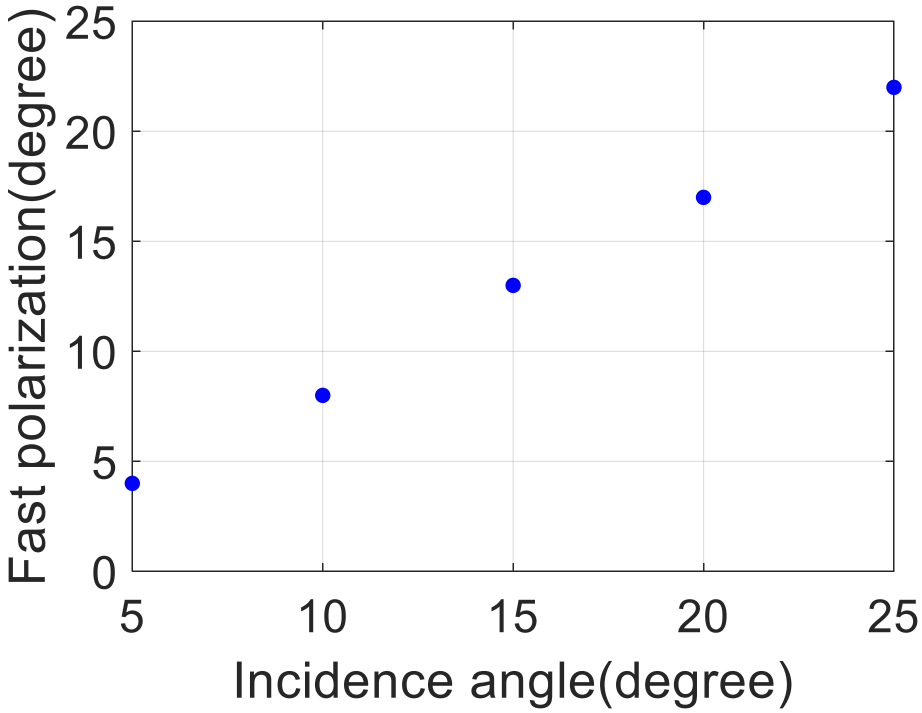

Figure 69 The polarization angle (ϕ) of fast S wave (S-S_1-S) due to different incidence angles i at the 60-degree slab dip angle.

7.1.2 *SH* incidence

The incoming S wave in isotropic layer 3 is SH wave is polarized orthogonal to the acquisition plane. The time delay *dt* between S-S_1-S and S-S_2-S are recorded as a function of different incidence angles from 5 to 25 every 5 degrees (*Figure 70*, *Figure 72* and *Figure 74*) when the slab dipping angle θ_{dip} = 15, 40, and 60 degrees. The fast polarization angle ϕ (the orientation of the fast S phase) is also obtained in the same way.

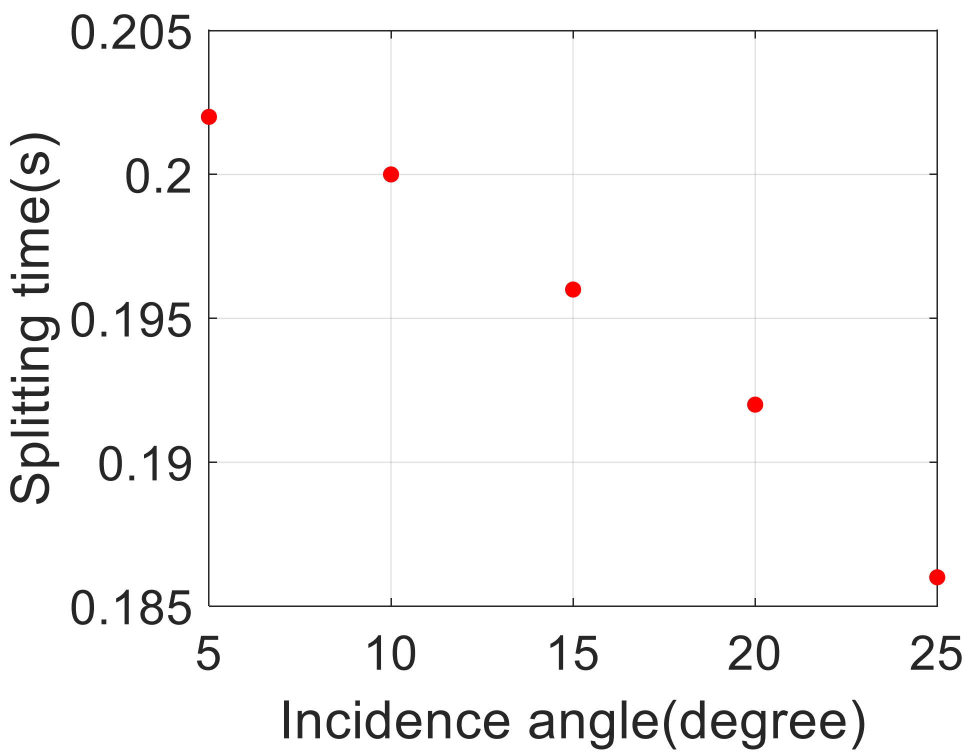

Figure 70 Time delay (splitting time) *dt* of S-S_1-S and S-S_2-S due to different incidence angles i at the 15-degree slab dip angle.

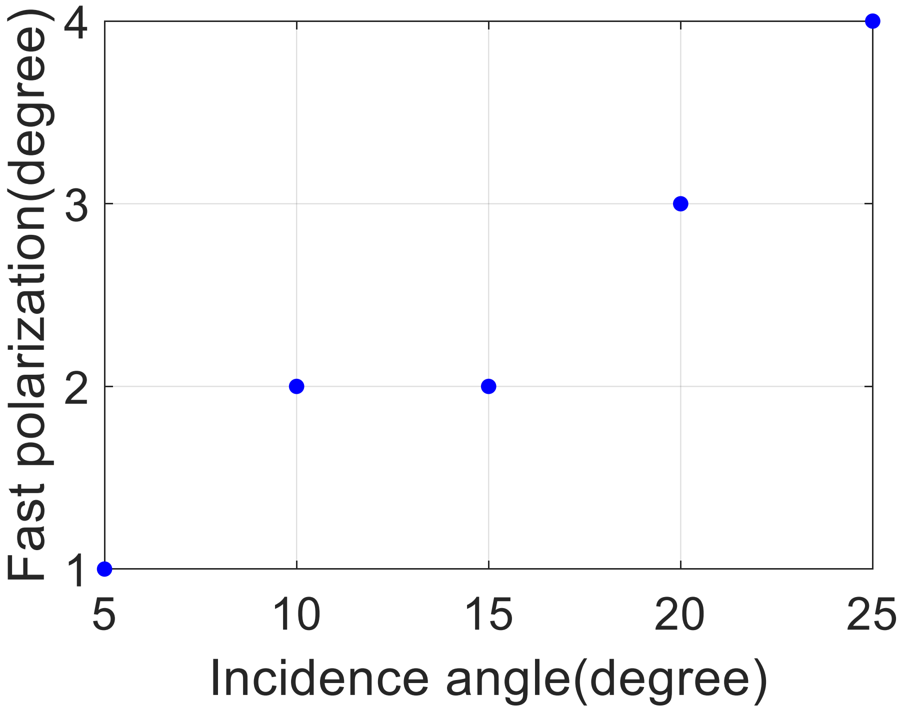

Figure 71 The polarization angle (ϕ) of fast S wave (S-S_1-S) due to different incidence angles i at the 15-degree slab dip angle.

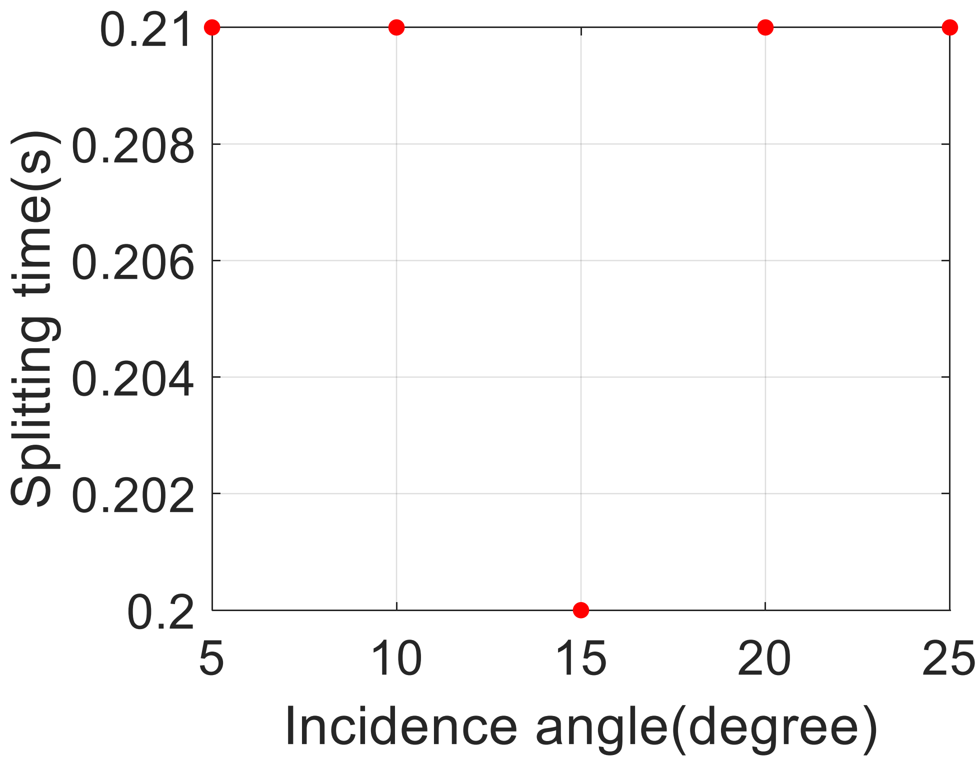

Figure 72 Time delay (splitting time) dt of S-S_1-S and S-S_2-S due to different incidence angles i at the 40-degree slab dip angle.

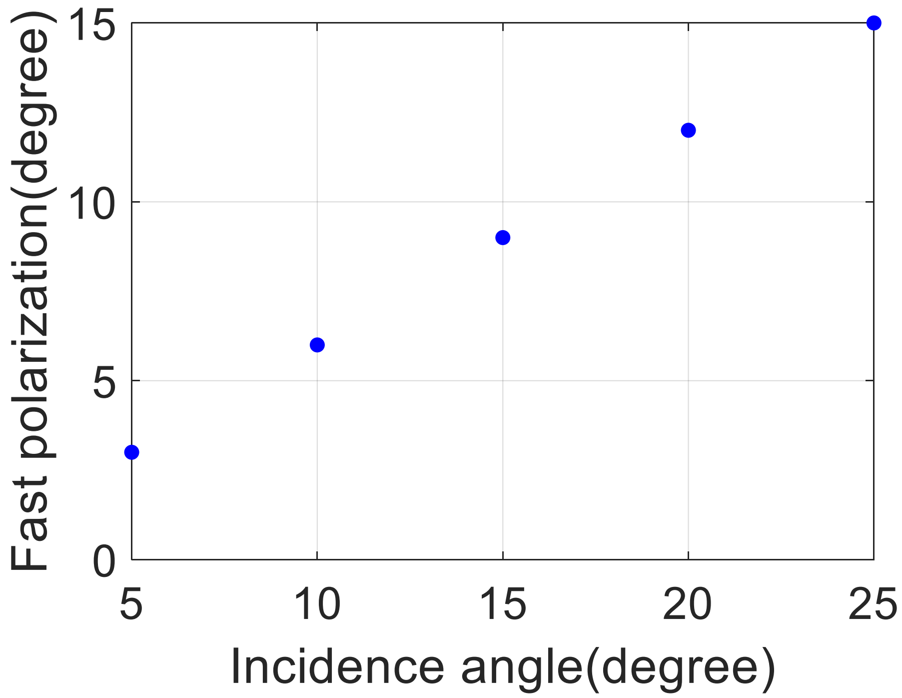

Figure 73 The polarization angle (ϕ) of fast S wave (S-S_1-S) due to different incidence angles i at the 40-degree slab dip angle.

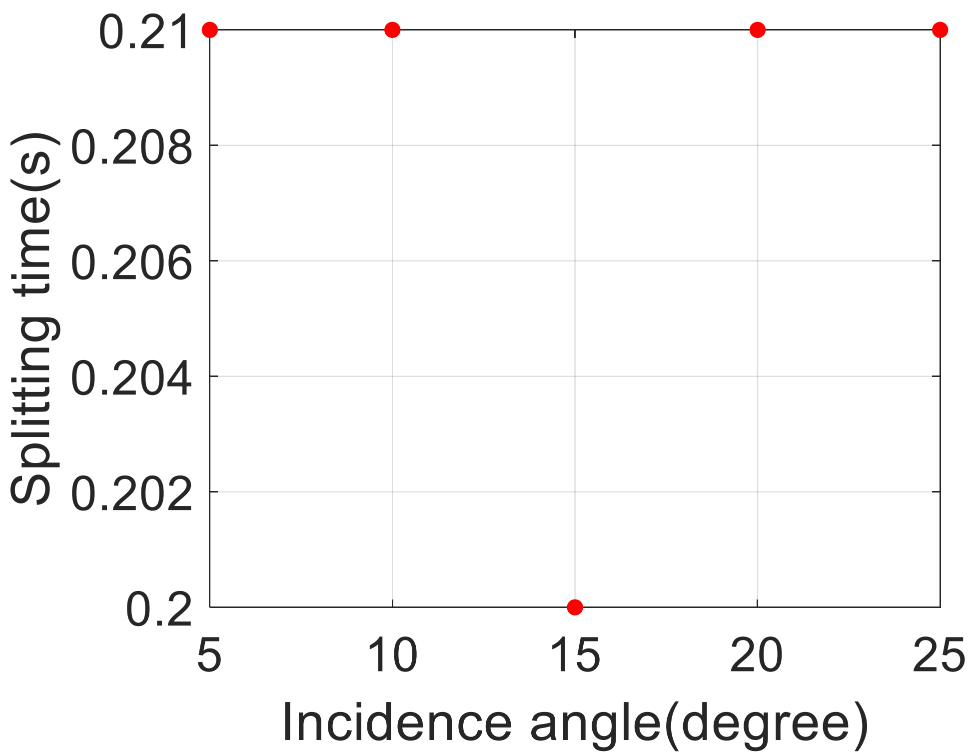

Figure 74 Time delay (splitting time) dt of S-S_1-S and S-S_2-S due to different incidence angles i at the 60-degree slab dip angle.

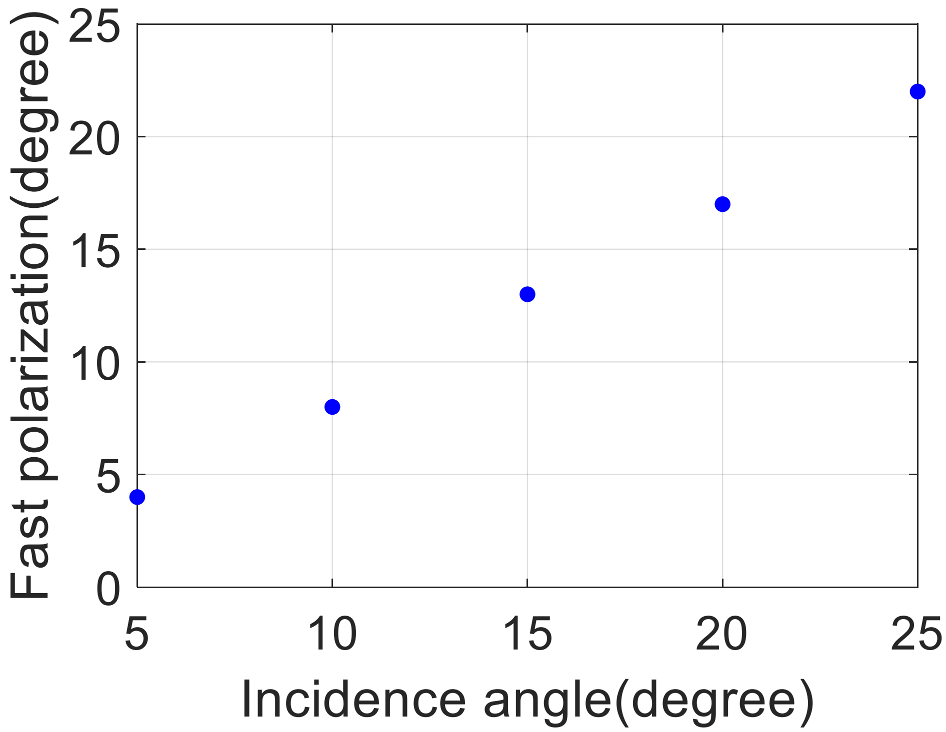

Figure 75 The polarization angle (ϕ) of fast S wave (S-S_1-S) due to different incidence angles i at the 60-degree slab dip angle.

For both SV and SH incidence, the change of splitting time and fast polarization are related to the incidence angle. The fast polarization is parallel or sub-parallel to the subduction direction which is X' in my model (*Figure 59*) at incidence angles from 5 to 10 degrees. The splitting time of S-S_1-S and S-S_2-S is at around 2s for SV incidence and 0.2s for SH incidence when the thickness of the slab is 20 km and the anisotropy of S wave is ~25%. The change of fast polarization angles at slab dip 15, 40, and 60 degrees for SV incidence (*Figure 65*, *Figure 67* and *Figure 69*) and SH incidence (*Figure 71*, *Figure 73*, and *Figure 75*), revealing that the polarization of the fast S wave is controlled by the dipping angle of the slab.

7.2 VTI model

The only difference between this model and my HTI model in **Section 7.1** is the type of anisotropy in the slab. The fracture embedded in the slab is the VTI medium in the local coordinate system. All other parameters are defined the same as in **Section 7.1**.

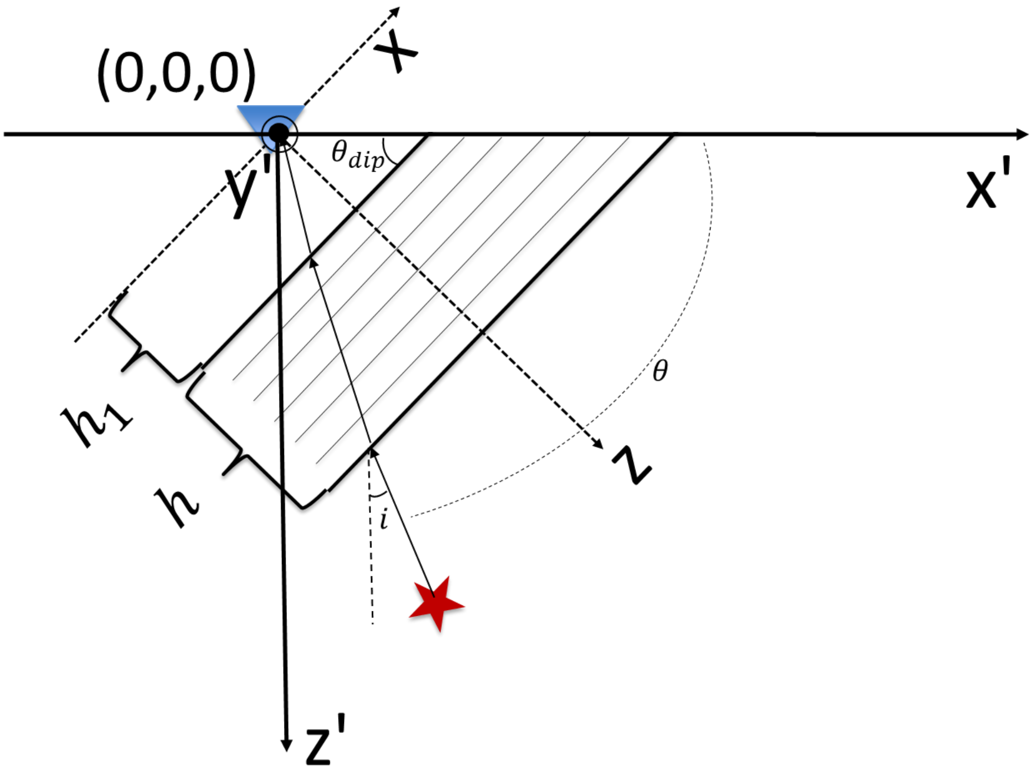

Figure 76 Schematic of a fractured subducting slab model under two sets of coordinate systems. (X, Y, Z) is defined as the local coordinate system. (X', Y', Z') is defined as the global coordinate system. Red star denotes the source. Blue triangle denotes the receiver. i denote the incidence angle. h is the thickness of the fracture layer. The slab is dipping southwest with θ_{dip} as the dipping angle. The slab strike is along the y-axis.

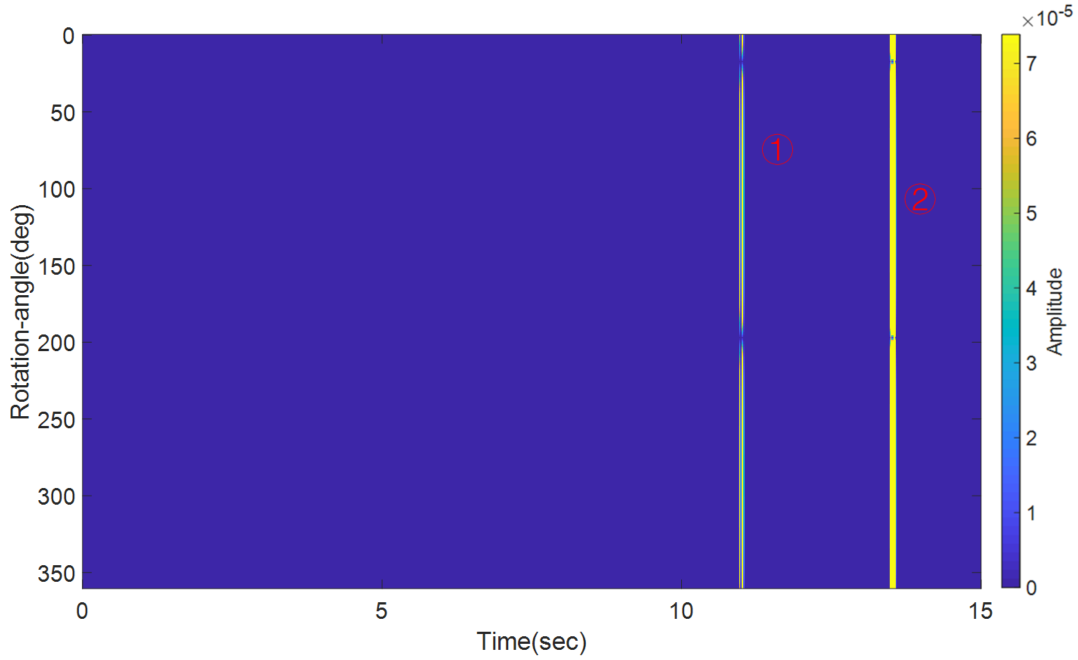

Figure 77 Transmission of S wave in layer 1 at the 60-degree azimuth. The incidence wave is SV wave. The incidence angle i (*Figure 60*) is 10 degrees. The slab dipping angle is 40 degrees.

The acquisition geometry is identical to the geometry shown in *Figure 60*. For SV incidence, I calculated the transmitted wavefield in the local coordinate system first before transforming to global coordinate system. As defined in **Section 7.1.1**, S_2 denotes the slow S wave. Seismic events 1 ~ 2 in Figure *77* are: S-P-S, S-S_2-S waves.When the slab is transversely isotropic with a vertical symmetry axis (VTI) in the local coordinate system, we could only have the slow S wave in seismic records (*Figure 77*). As a result, I could not extract neither the splitting time, nor the polarization of fast S wave in this modeling for SV incidence. This situation has been discussed in detail in **Section 5.2**, the VTI case for the three-layer model. However, if the incidence wave is *SV* coupled with *SH* in local coordinate system, the splitting could be observed (*Figure 78*).

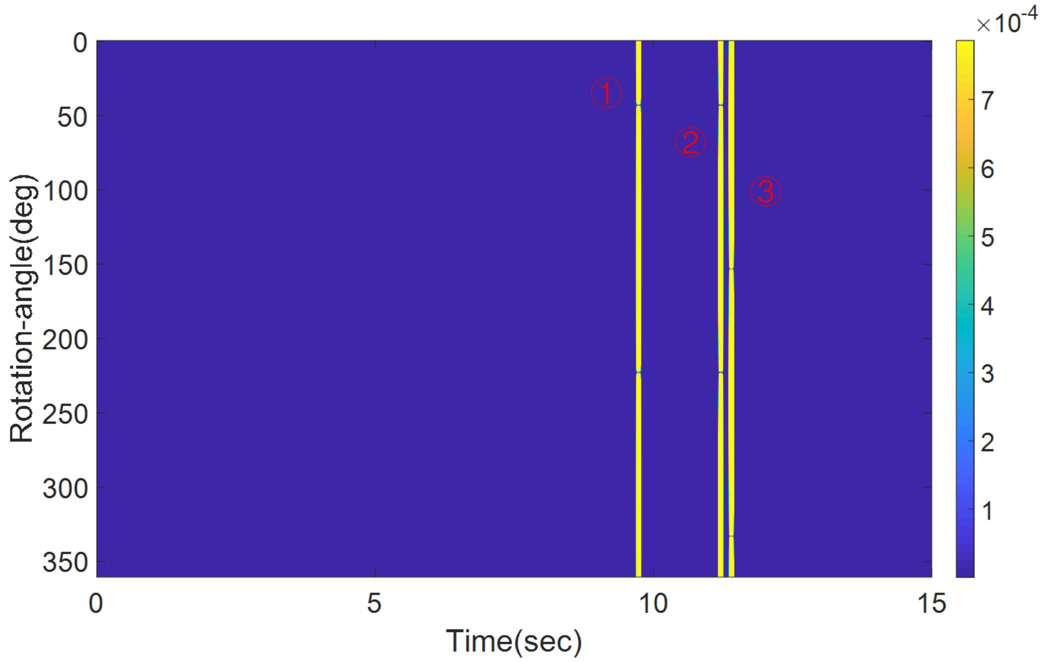

Figure 78 Transmission of S wave in layer 1 at the 60-degree azimuth. The incidence wave is the combination of SV and SH wave. The incidence angle i (*Figure 60*) is 20 degrees. The slab dipping angle is 60 degrees. Seismic events 1 ~ 3 are: S-P-S, S-S_1-S, and S-S_2-S waves.

7.3 TTI model

The slab model and the acquisition geometry are exactly the same as that has been talked about in **Section 7.1 (HTI model)**. The only difference of the TTI model and the HTI model is the type of anisotropy in the slab. In the TTI model, we define the tilt angle β as the angle between the anisotropy fabric and the normal of the slab interface (*Figure 79*). In particular, when β is 90-degree, the fracture model is VTI; when β is 0-degree, the fracture model is HTI.

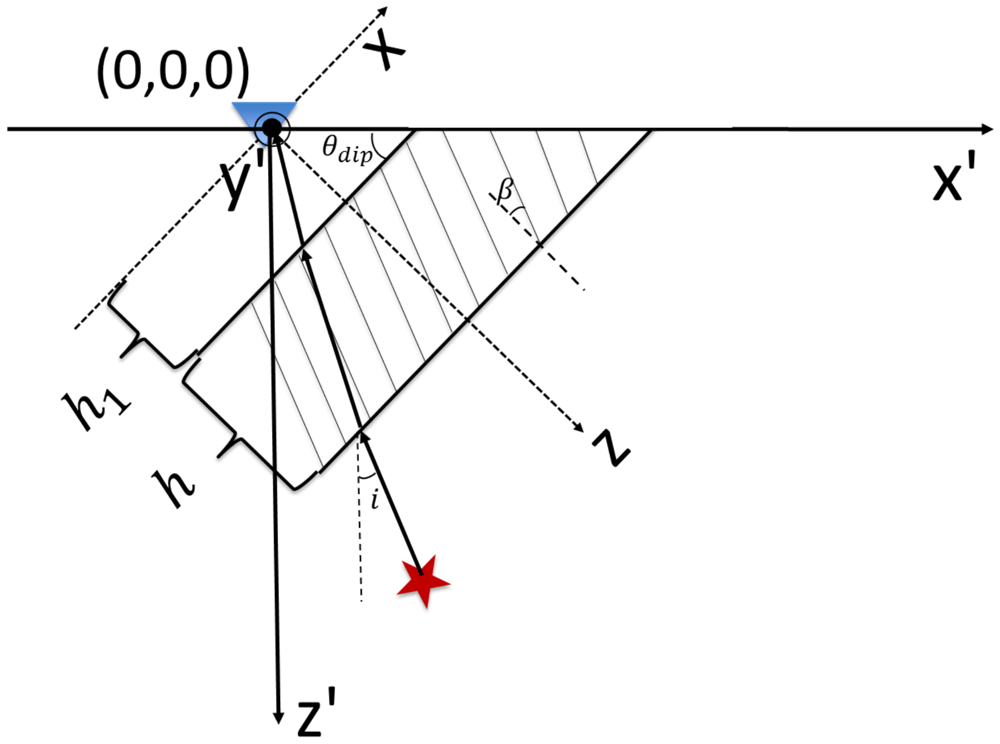

Figure 79 Schematic of a fractured subducting slab model under two sets of coordinate systems. (X, Y, Z) is defined as the local coordinate system. (X', Y', Z') is defined as the global coordinate system. Red star denotes the source. Blue triangle denotes the receiver. i denote the incidence angle. h is the thickness of the fracture layer. The slab is dipping southwest with θ_{dip} as the dipping angle. The slab strike is along the y-axis. The tilt angle β is the angle between the anisotropy fabric and the normal of the slab interface.

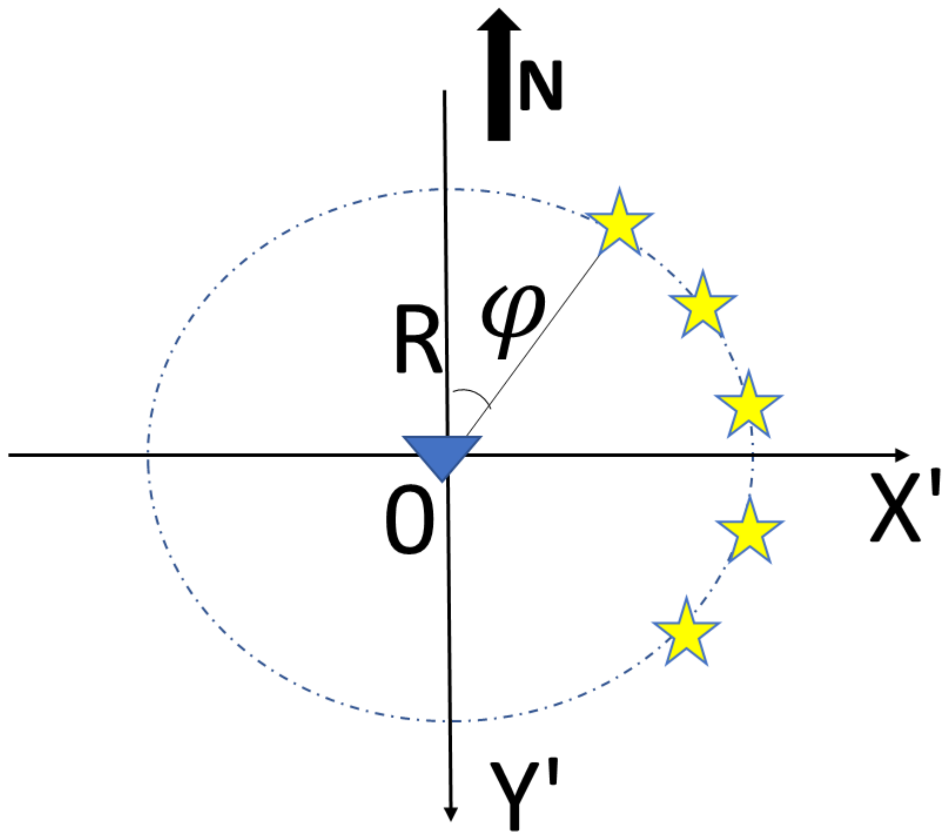

Figure 80 Schematic of geometry of seismic acquisition from top view. Blue stars are the projections on the surface of sources that are deep down the ground in layer 3 of the three-layered model. The blue triangle at zero is the receiver at the surface. The slab is embedded with a set of fractures. φ is the azimuth, defined as the angle between the north and the source to receive line. The slab strike is along the 0-degree azimuth. The slab is dipping southwest.

In my model, the transmitted wavefields are recorded at the surface along different azimuths from φ=40 to 140 degrees every 10 degrees (*Figure 80*). The source to receiver distance R is 50 km. The background *P* wave velocity is 6000 m/s and the *S* wave velocity is 4000 m/s. Density is 2400 kg/m^3. The fracture slab is 20 km thick. I set the azimuthal anisotropy to 25% with a fast symmetry axis along the slab dip for the *S* wave. In this section, I will investigate the following three topics for *SV* incidence: the effect of the tilt angle on the transmitted seismic wavefield of a TTI slab model; and the effect of the azimuth on the transmitted seismic wavefield of a TTI slab model; the effect of the incidence angle on the transmitted seismic wavefield of a TTI slab model.

7.3.1 Effect of the tilt angle on the splitting time and polarization of fast shear wave for SV incidence

The incoming S wave in isotropic layer 3 is the SV wave with a 10-degree incidence angle. The azimuth is set as 60 degrees. The tilt angle varies from 0 to 90 degrees. The transmitted wavefield recorded at layer 1 are S-P-S, S-S_1-S and S-S_2-S waves (*Figure 81*). I calculated the time delay dt of the S-S_1-S and S-S_2-S transmission for different tilt angles (*Figure 83*) and the polarization of the fast shear wave as well.

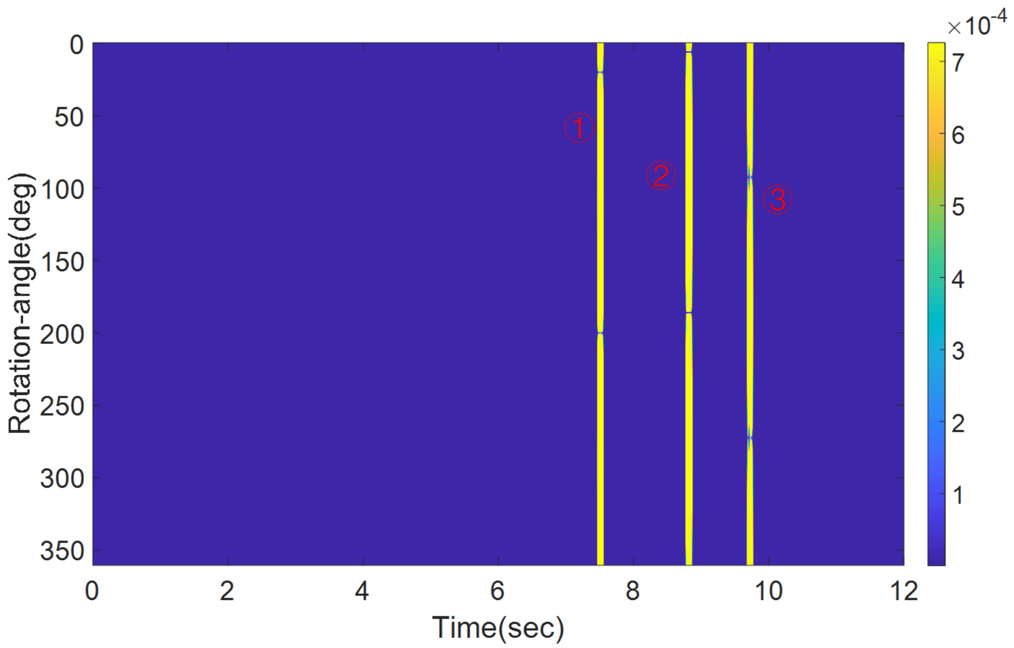

Figure 81 Transmission of S wave in layer 1 at the 60-degree azimuth. The incidence angle i is 10 degrees. The slab dipping angle is 60 degrees. The tilt angle is 45 degrees. Seismic events 1 ~ 3 are: S-P-S, S-S_1-S, and S-S_2-S waves.

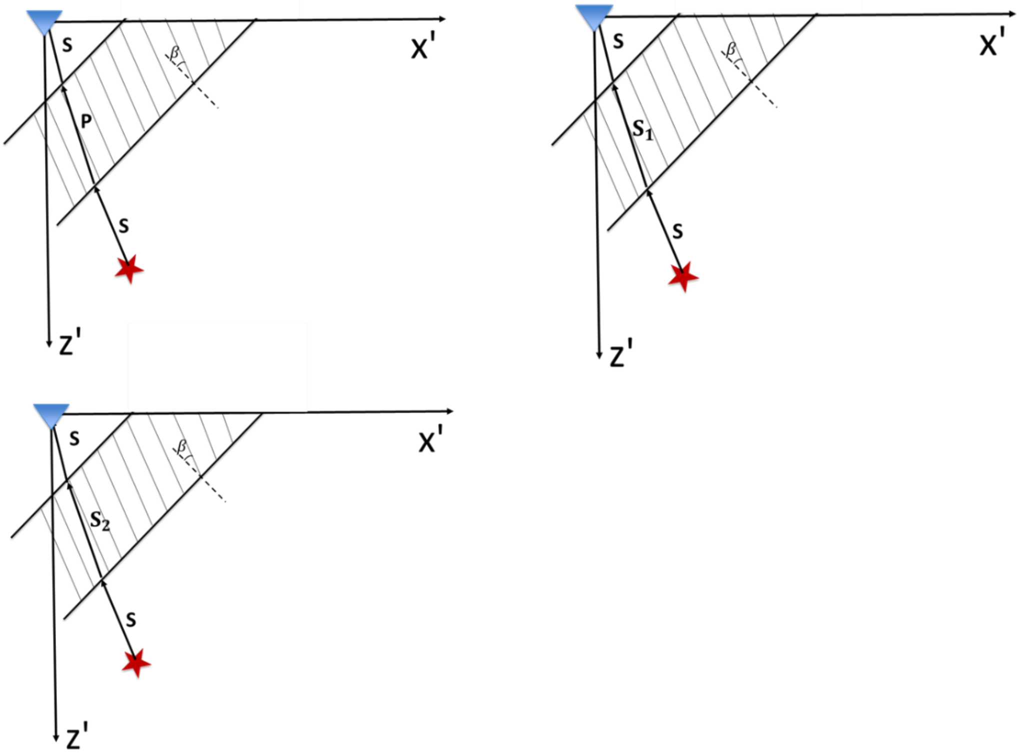

Figure 82 Schematic of ray paths of seismic event 1~3 in *Figure 81* when the azimuth is 60 degrees (global coordinate system).

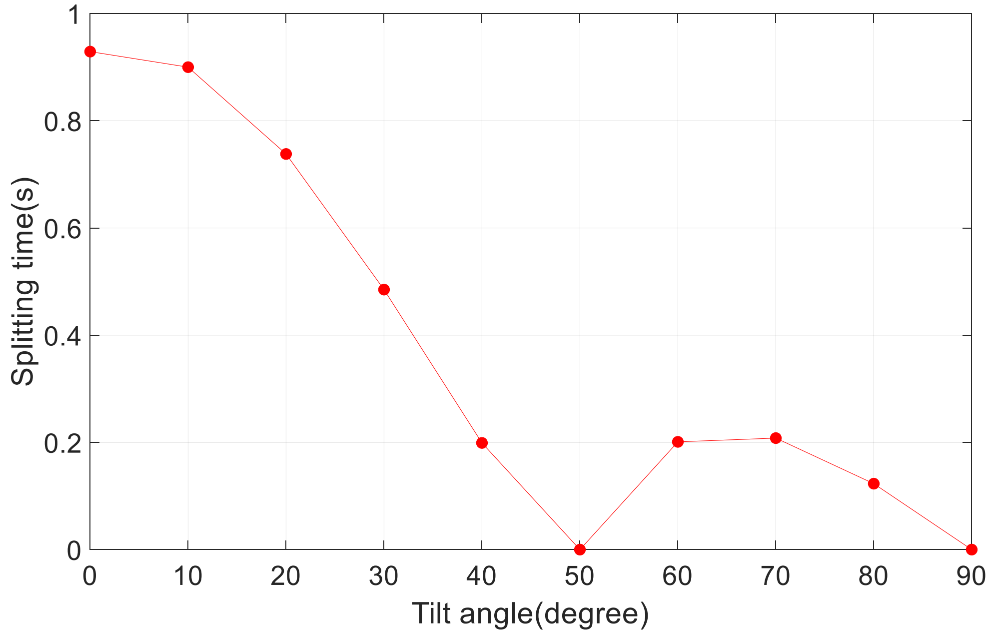

Figure 83 Time delay (splitting time) dt of S-S_1-S and S-S_2-S due to different tilt angles β at the 60-degree azimuth. The incidence wave is SV wave, incidence angle is 10 degrees.

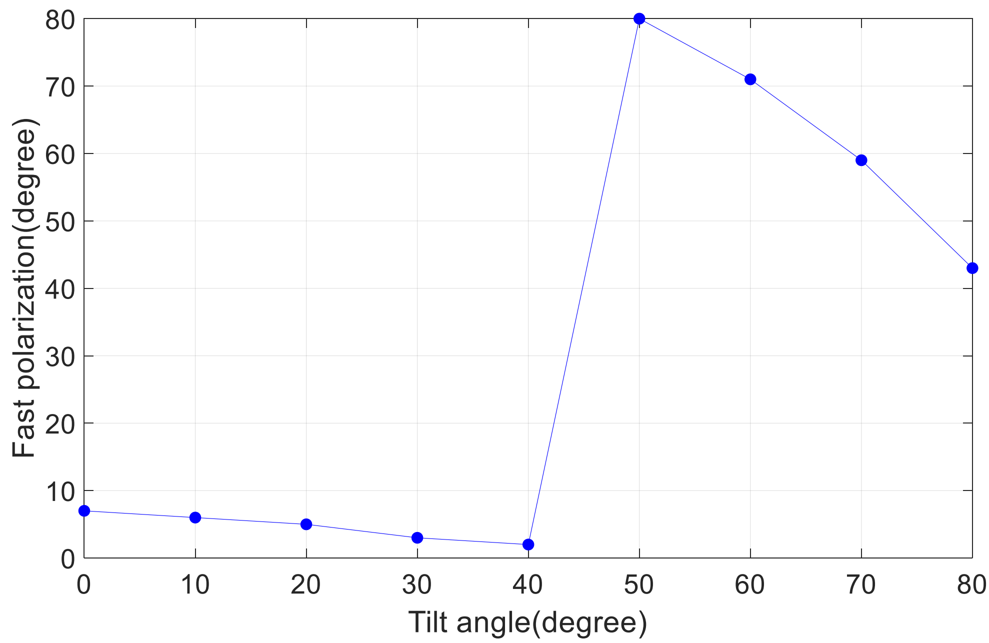

Figure 84 The polarization of the fast S wave angle ϕ (defined in *Figure 62*) due to different tilt angles β at the 60-degree azimuth. The incidence wave is SV wave, incidence angle is 10 degrees.

According to *Figure 83*, the splitting time is the largest when the fracture model has HTI anisotropy (when the tilt angle is 0 degrees). The splitting time is zero at a 50-degree tilt angle and a 90-degree tilt angle (VTI). For the TTI slab model, we could observe the jump of polarization of fast shear wave at 50-degree tilt angle (*Figure 84*).

7.3.2 Effect of the azimuth on the splitting time and polarization of fast shear wave for *SV* incidence

In this section, I calculated the time delay *dt* of the S-S_1-S and S-S_2-S transmission and the polarization of the fast-shear wave for different azimuths. The incoming S wave in isotropic layer 3 is the SV wave with a 10-degree incidence angle. The tilt angle is 45 degrees. The azimuth varies from 40 to 140 degrees every 10 degrees.

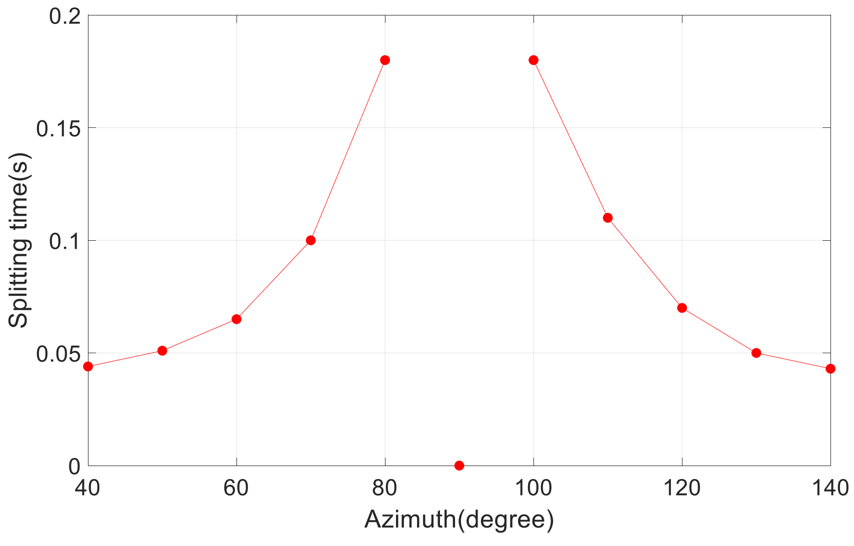

Figure 85 Time delay (splitting time) *dt* of S-S_1-S and S-S_2-S due to different azimuths at the 45-degree tilt angle. The incidence wave is *SV* wave, incidence angle is 10 degrees.

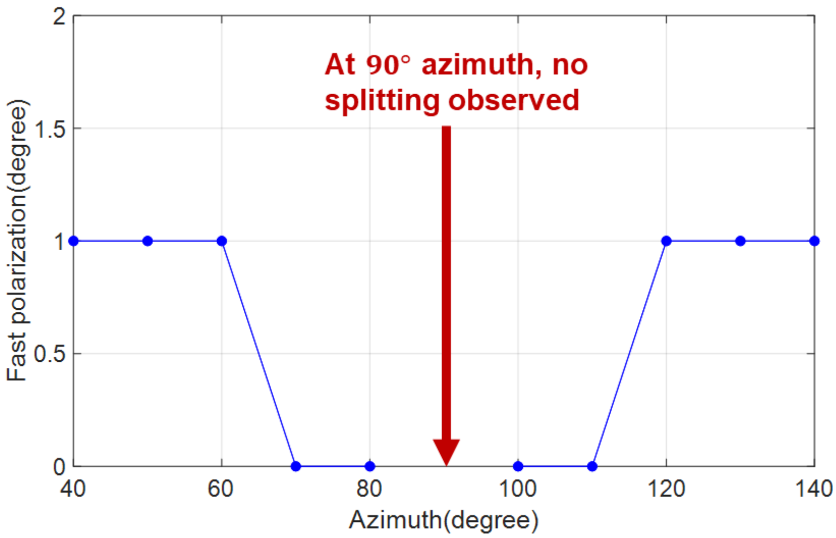

Figure 86 The polarization of the fast *S* wave angle ϕ due to different azimuths at the 45-degree tilt angle. The incidence wave is *SV* wave, incidence angle is 10 degrees.

According to *Figure 85*, the splitting time increase from 40- to 80-degree azimuth and then suddenly jumps to 0 on 90-degree azimuth which is also the symmetry axis plane of the TTI medium. In order to investigate this phenomenon, I calculated the change of velocities in the anisotropic layer 2 (*Figure 87*) and the transmission coefficient of SH wave (*Figure 88*) with different azimuths.

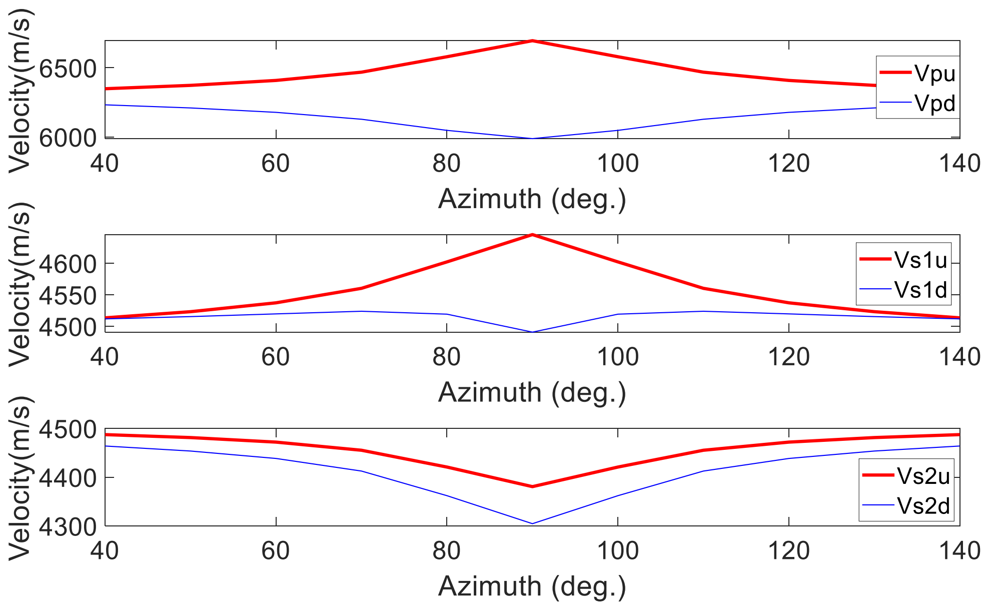

Figure 87 Velocities of downgoing *P*, fast *S* wave S_1 and slow *S* wave S_2 and upgoing *P*, fast *S* wave S_1 and slow *S* wave S_2 in fractured layer 2 due to different azimuths. Fracture strike plane is along 0-degree azimuth, symmetry axis plane is along 90-degree azimuth. Vpu is the upgoing *P* wave and Vpd is the downgoing *P* wave. Vs1u is the upgoing fast *S* wave S_1 and Vs1d is the downgoing fast *S* wave S_1. Vs2u is the upgoing slow *S* wave S_2 and Vs2d is the downgoing slow *S* wave S_2.

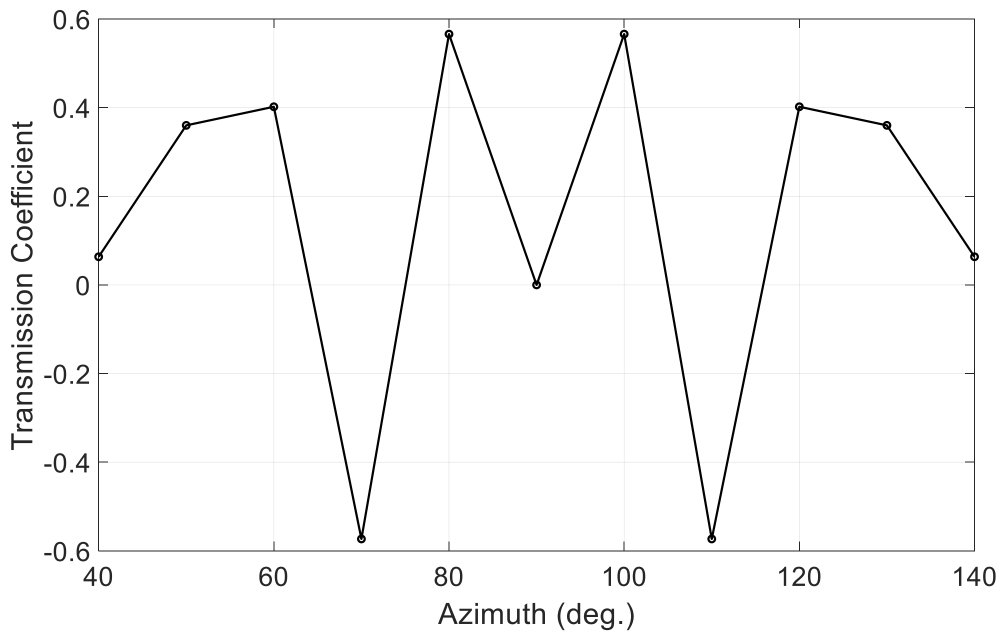

Figure 88 Transmission coefficients for *SH* wave in isotropic layer 1 due to different azimuths when t = 1 s.

What we are concerned about is the velocities of the upgoing fast *S* wave S_1 and upgoing slow S wave S_2 in layer 2, because they will finally propagate into layer 1 and be recorded as the transmitted wavefields at the surface. The velocity difference between these two waves makes the time difference. According to *Figure 87*, the velocity of the upgoing fast-shear wave increases from 40 to 90 degrees azimuth and is largest at the 90-degree azimuth. The velocity of upgoing slow shear wave decreases from 40 to 90 degrees azimuth and is the smallest at the 90-degree azimuth. Thus, the time difference increases from 40 to 80 degrees. However, the coefficient of *SH* wave is 0 at 90 degrees azimuth (*Figure 88*). No fast shear wave could be recorded at that azimuth, which makes no splitting at the symmetry axis plane (90 degrees azimuth).

7.3.3 Effect of the incidence angle on the splitting time and polarization of fast shear wave for *SV* incidence

In this section, I calculated the time delay *dt* of the S-S_1-S and S-S_2-S transmission and the polarization of the fast shear wave for different incidence angles. The incoming S wave in isotropic layer 3 is the SV wave with the incidence angles from 5 degrees to 25 degrees every 5 degrees. The tilt angle is 45 degrees. The azimuth is 60 degrees.

According to *Figure 89* and *Figure 90*, the change of splitting time and fast polarization is related to the incidence angle. The splitting time increases as the incidence angle changes from 5 to 25 degrees.

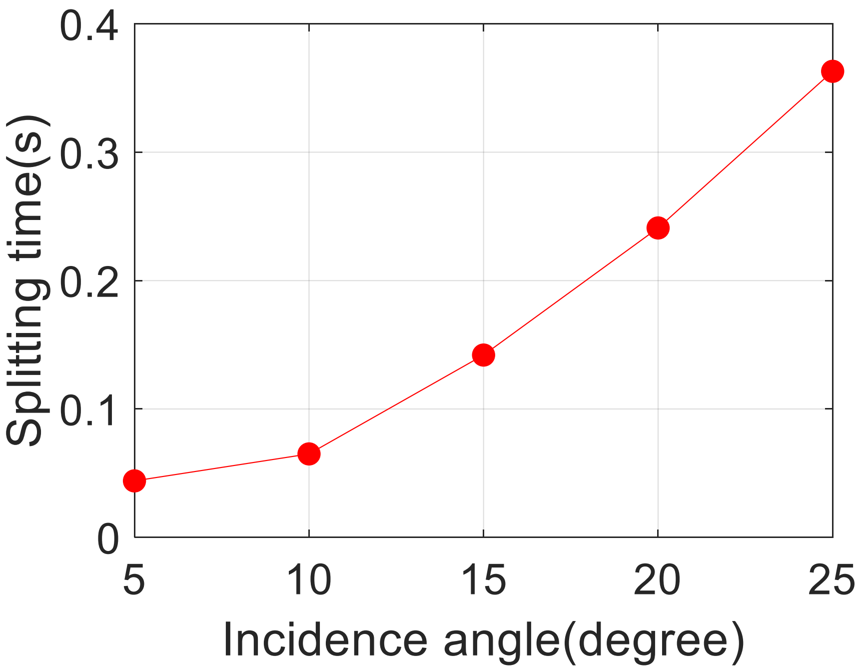

Figure 89 Time delay (splitting time) dt of S-S_1-S and S-S_2-S due to different incidence angles at the 60-degree azimuth. The incidence wave is SV wave. The tilt angle is 45 degrees.

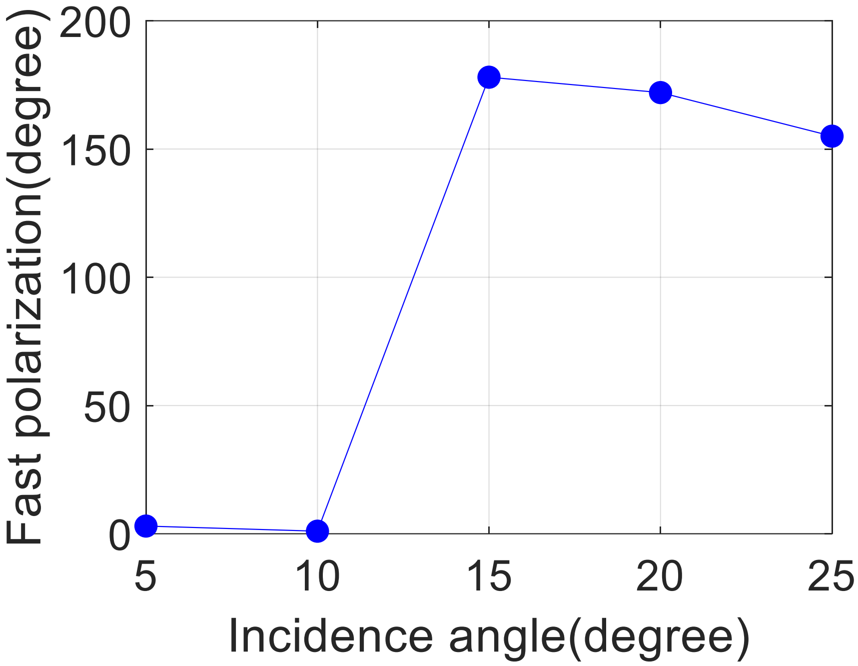

Figure 90 The polarization of the fast *S* wave angle ϕ due to different incidence angles at the 60-degree azimuth. The incidence wave is *SV* wave. The tilt angle is 45 degrees.

7.4 Conclusions

In this chapter, I measured two splitting parameters from seismic records: ϕ and *dt*. Among these two parameters, ϕ corresponds to the orientation of the fast *S* phase and *dt* correspond to the time delay between the fast and slow transmitted shear waves.

For an HTI model, I found that the change of splitting time and fast polarization are all shown as a function of incidence angle. The fast polarization is not only related to the anisotropic property, but is also controlled by the slab dipping angle and incidence angle.

For a VTI model, if the incidence wave is *SV* or *SH* alone, no splitting is observed.

For a TTI model, the coefficient of the fast shear wave is 0 on the symmetry axis plane. No splitting is observed on the symmetry axis plane, although the difference of the velocity values between the fast shear wave and the slow shear wave is the largest.

Chapter 8

Conclusions

For this thesis, I first calculated the reflected and transmitted wavefields caused by an incident plane wave propagating through a fractured layer. Next, I investigated how the thickness of the fractured layer and the normal and tangential fracture compliances influence the reflected wavefield. Finally, I studied the splitting time and fast polarization of transmitted seismic wavefield of a subducting slab model.

I applied numerical seismic modeling in this thesis. Solving the Green-Christoffel equation, I obtained the solutions of polarization vectors of scattered waves. Using boundary condition, I solved the reflection and transmission coefficients for scattered waves in the fracture layer. The reflected wavefield of both P and S wave has also been resolved for their azimuthal dependence behavior.

I created multiple models to illustrate the relationship between fractured layer thickness and reflected wavefield (both P and S reflection). For P reflection, P wave travels faster along the fractures than perpendicular to the fractures through vertically aligned fractures set. As a result, the traveltime and amplitude of reflected P wave vary with azimuth. The thickness of the fractured layer is also related to the reflected P wavefield, because it needs to be thick enough (more than a P wavelength) to accurately extract fracture parameters from the seismic data. For S reflection, shear wave splitting relates to the thickness of the fractured layer. In order to observe splitting, the thickness of fractured layer must not be larger than 5 times of the S wave wavelength.

I also investigated the effect of normal and tangential fracture compliances on reflected P and S waves. For P reflection, I calculated the reflected wavefield caused by different fracture normal and tangential compliance ratios based on several published measurement of Z_N/Z_T from 0.02 to 1.2. The magnitude of azimuthal variation of P wave amplitude and traveltime tends to be more distinct when the Z_N/Z_T becomes larger. For S reflection, I found that Thomsen's γ only relates to the tangential compliance Z_T. Therefore, the tangential fracture compliance Z_T controls the shear wave splitting. The time difference extracted from shear wave splitting analysis would not be reliable at low Z_N/Z_T (less than 0.4).

Finally, I investigated the relation between splitting time of transmitted S wave of a subducting anisotropic slab and slab dip, as well as the relation between fast polarization and slab dip, for different types of anisotropy. I found that the fast polarization is controlled not only by the nature of anisotropy but also the slab dipping angle and the incidence angle.

References

Aguilera, R., and M. S. Aguilera (2001), Well Test Analysis of Multi-Layered Naturally Fractured Reservoirs with Variable Thickness and Variable Fracture Spacing, Journal of Canadian Petroleum Technology, 40(12), 9-12.

Angus, D. A., J. P. Verdon, Q. J. Fisher, and J.-M. Kendall (2009), Exploring trends in microcrack properties of sedimentary rocks: An audit of dry-core velocity-stress measurements, Geophysics, 74(5), 193-203.

Bale, R., B. Gratacos, B. Mattocks, S. Roche, K. Poplavskii, and X. Lil (2009), Shear wave splitting applications for fracture analysis and improved imaging: Some onshore examples, First Break, 27(9):73-83.

Crampin, S., and S. Chastin (2003), A review of shear wave splitting in the crack-critical crust, Geophysical Journal International, 155(1), 221-240.

Crampin, S., and R. McGonigle (1981), The variation of delays in stress-induced anisotropic polarization anomalies, Geophysical Journal of the Royal Astronomical Society, 64(1), 115-131.

Du, Q., Y. Dong, H. Yang, and Y. Wang (2002), Shear Wave Velocity Estimation in HTI Media, Journal of Computational Acoustics, Theoretical and Computational Acoustics 2001. Beijing: World Scientific.

Dyke, C. G., B. Wu, and D. Milton-Tayler (1995), Advances in Characterising Natural Fracture Permeability From Mud Log Data, SPE Formation Evaluation, 10(03), 160-166.

Fang, X. D., Y. C. Zheng, and M. C. Fehler (2017), Fracture clustering effect on amplitude variation with offset and azimuth analyses, Geophysics, 82(1), 13-25.

Gaiser, J., and R. Van Dok(2001), Green River Basin 3-D/3-C Case Study For Fracture Characterization: Analysis of PS-wave Birefringence, 2001 SEG Annual Meeting, San Antonio, Texas, 2001/1/1.

Hall, S., and J. M. Kendall (2003), Fracture characterization at Valhall: Application of P-wave amplitude variation with offset and azimuth (AVOA) analysis to a 3D ocean-bottom data set, Geophysics, 68(4), 1150-1160.

Hobday, C., and M. H. Worthington (2012), Field measurements of normal and shear fracture compliance, Geophysical Prospecting, 60(3), 488-499.

Hsu, C. J., and M. Schoenberg (1993), Elastic waves through a simulated fractured medium, Geophysics, 58(7), 964-977.

Keith, C. M., and S. Crampin (1977), Seismic body waves in anisotropic media: synthetic seismograms, Geophysical Journal of the Royal Astronomical Society, 49(1), 225-243.

Khoshbakht, F., H. Memarian, and M. Mohammadnia (2009), Comparison of Asmari, Pabdeh and Gurpi formation's fractures, derived from image log, Journal of Petroleum Science and Engineering, 67(1), 65-74.

Kosarev, G. L., L. I. Makeyeva, and L. P. Vinnik (1984), Anisotropy of the mantle inferred from observations of P to S converted waves, Geophysical Journal International, 76(1), 209-220.

Liu, E., and A. Martinez (2012), 2 - Fundamentals of seismic anisotropy, in Seismic Fracture Characterization. Oxford: EAGE.

Liu, E., G. Zelewski, C.-P. Lu, J. Reilly, and Z. J. Shevchek(2010), Seismic Fracture Prediction Using Azimuthal AVO Analysis In a Middle East Carbonate Field:workflow And Mitigation of Overburden Effects, 2010 SEG Annual Meeting, Denver, Colorado, 2010/1/1.

Liu, Y. W., X. W. Liu, Y. X. Lu, Y. Q. Chen, and Z. Y. Liu (2018), Fracture prediction approach for oil-bearing reservoirs based on AVAZ attributes in an orthorhombic medium, Petroleum Science, 15(3), 510-520.

Long, M. D., and P. G. Silver (2009), Shear Wave Splitting and Mantle Anisotropy: Measurements, Interpretations, and New Directions, Surveys in Geophysics, 30(4), 407-461.

Lubbe, R., J. Sothcott, M. H. Worthington, and C. McCann (2008), Laboratory estimates of normal and shear fracture compliance, Geophysical Prospecting, 56(2), 239-247.

MacBeth, C., and H. Schuett (2007), The stress dependent elastic properties of thermally induced microfractures in aeolian Rotliegend sandstone, Geophysical Prospecting, 55(3), 323-332.

Nelson, R. A. (2001), Geologic Analysis of Naturally Fractured Reservoirs (2nd Edition), Elsevier.

Pyrak-Nolte, L. J., L. R. Myer, and N. G. W. Cook (1990), Transmission of seismic waves across single natural fractures, Journal of Geophysical Research: Solid Earth, 95(B6), 8617-8638.

Rathore, J. S., E. Fjaer, R. M. Holt, and L. Renlie (1995), P- and S-wave anisotropy of a synthetic sandstone with controlled crack geometryl1, Geophysical Prospecting, 43(6), 711-728.

Rüger, A. (1998), Variation of P-wave reflectivity with offset and azimuth in anisotropic media, Geophysics, 63(3), 935-947.

Rüger, A. (2002), Reflection Coefficients and Azimuthal AVO Analysis in Anisotropic Media. Portland: Society of Exploration Geophysicists.

Sayers, C. M. (1999), Stress-dependent seismic anisotropy of shales, Geophysics, 64(1), 93-98.

Sayers, C. M., and L. D. den Boer (2012), Characterizing production-induced anisotropy of fractured reservoirs having multiple fracture sets, Geophysical Prospecting, 60(5), 919-939.

Sayers, C. M., and D. H. Han (2002), The effect of pore fluid on the stress-dependent elastic wave velocities in sandstones, 2002 SEG Annual Meeting, Salt Lake City, Utah, 2002/10/6.

Schoenberg, M. (1980), Elastic wave behavior across linear slip interfaces, Journal of the Acoustical Society of America, 68(5), 1516-1521.

Schoenberg, M., and C. M. Sayers (1995), Seismic Anisotropy of Fractured Rock, Geophysics, 60(1), 204-211.

Silver, P. G., and W. W. Chan (1988), Implications for continental structure and evolution from seismic anisotropy, Nature, 335, 34.

Silver, P. G., and W. W. Chan (1991), Shear wave splitting and subcontinental mantle deformation, Journal of Geophysical Research: Solid Earth, 96(B10), 16429-16454.

Song, T.-R. A., and H. Kawakatsu (2012), Subduction of oceanic asthenosphere: Evidence from sub-slab seismic anisotropy, Geophysical Research Letters, 39(17).

Thomsen, L. (1986), Weak elastic anisotropy, Geophysics, 51(10), 1954-1966.

Thomsen, L. (2002), Understanding Seismic Anisotropy in Exploration and Exploitation. Tulsa: Society of Exploration Geophysicists.

Tsvankin, I. (2001), Seismic Signatures and Analysis of Reflection Data in Anisotropic Media, Elsevier Science. Oxford: Elsevier Science.

Verdon, J. P., D. A. Angus, J. M. Kendall, and S. A. Hall (2008), The effect of microstructure and nonlinear stress on anisotropic seismic velocities, Geophysics, 73(4), D41-D51.

Verdon, J. P., and A. Wustefeld (2013), Measurement of the normal/tangential fracture compliance ratio (ZN/ZT) during hydraulic fracture stimulation using S-wave splitting data, Geophysical Prospecting, 61, 461-475.

Vetri, L., E. Loinger, J. Gaiser, A. Grandi, and H. Lynn (2003), 3D/4C Emilio: Azimuth processing and anisotropy analysis in a fractured carbonate reservoir, The Leading Edge, 22(7), 675-679.

Yousef, B. M., and D. A. Angus (2016), When do fractured media become seismically anisotropic? Some implications on quantifying fracture properties, Earth and Planetary Science Letters, 444, 150-159.